INDUCTIVELY COUPLED CMOS POWER RECEIVER FOR EMBEDDED MICROSENSORS

A Dissertation
Presented to
The Academic Faculty

by

Nan Xing

In Partial Fulfillment
of the Requirements for the Degree
of Doctor of Philosophy in the
School of Electrical and Computer Engineering

Georgia Institute of Technology
May 2020

COPYRIGHT © 2020 BY NAN XING

INDUCTIVELY COUPLED CMOS POWER RECEIVER FOR EMBEDDED MICROSENSORS

Approved by:

Dr. Gabriel A. Rincón-Mora, Advisor School of Electrical and Computer Engineering *Georgia Institute of Technology*	Dr. Deepakraj M. Divan School of Electrical and Computer Engineering *Georgia Institute of Technology*
Dr. Hua Wang School of Electrical and Computer Engineering *Georgia Institute of Technology*	Dr. James S. Kenney School of Electrical and Computer Engineering *Georgia Institute of Technology*
Dr. Yingjie Liu School of Mathematics *Georgia Institute of Technology*	

Date Approved: April 7, 2020

ACKNOWLEDGEMENTS

I would like to thank my advisor, Dr. Gabriel Alfonso Rincón-Mora for this technical guidance and encouragement throughout the Ph.D. program.

I would also like to thank my dissertation and proposal committee members, Dr. Deepakraj Divan, Dr. Hua Wang, Dr. James Stevenson Kenney, and Dr. Yingjie Liu for their valuable feedback and suggestions.

Furthermore, I would like to thank my colleagues and alumni in Georgia Tech Analog, Power, and Energy lab, Dr. Andres Blanco, Dr. Orlando Lazaro, Dr. Rajiv Prahba, Dr. Carlos Solis, Jushua Cowan, Jun-Yang Lei, Siyu Yang, Tianyu Chang, Devon Janke, Guillaume Guerin for the fruitful discussions and support.

My thanks extend to Mr. Paul Emerson, Dr. Jeff Morroni, and Texas Instruments for supporting this research.

Finally, I would like to thank my family. Their support is endless. Without them, I couldn't have finished the program.

TABLE OF CONTENTS

ACKNOWLEDGEMENTS iii

LIST OF TABLES vii

LIST OF FIGURES viii

SUMMARY xiii

CHAPTER 1. Embedded Microsensors 1
1.1 Applications 1
  1.1.1 Biomedical Implants 1
  1.1.2 Structure/Material Monitoring 3
  1.1.3 Environment Sensing and Other Applications 3
  1.1.4 Summary 4
1.2 Powering Embedded Microsensors 6
  1.2.1 Energy Storage 6
  1.2.2 Harvesting Ambient Energy 9
  1.2.3 Wireless Power Transfer 11
  1.2.4 Summary 14

CHAPTER 2. Inductively Coupled Power Transfer 17
2.1 Inductive Coupling 17
2.2 Circuit Model 21
2.3 Maximum Power Point 26
2.4 MPP Power Receiver 30
  2.4.1 Ideality Index 30
  2.4.2 Boosting Drawn Power 31
  2.4.3 Maximizing Receiver Power 33
2.5 Research Objective 34

CHAPTER 3. The State of The Art In Power Receivers 37
3.1 Resonant Bridge 37
  3.1.1 Resonant Full-bridge 37
  3.1.2 Resonant Half-bridge 42
3.2 Multiplying Charge Pump 44
3.3 Switched Bridge 45
  3.3.1 Non-Investing Switched Bridge 45
  3.3.2 Investing Switched Bridge 48
3.4 Switched Resonant Bridge 51
  3.4.1 Serially Drained Scheme 51
  3.4.2 Directly Drained Scheme 52
3.5 Comparison 53

CHAPTER 4. Compact Switched-Resonant Half-Bridge 58

4.1 Power Stage 58
  4.1.1 Operation 58
  4.1.2 Energy Transfer 59
  4.1.3 Assessment 61
4.2 Design 61
  4.2.1 Parameters 61
  4.2.2 Maximum Output Power 65
  4.2.3 Tuning Accuracy 68
4.3 Measurements 69
  4.3.1 Prototype 69
  4.3.2 Power and Losses 71
  4.3.3 Charging Performance 73
4.4 Relative Performance 74
4.5 Remaining Challenges 77

CHAPTER 5. The Highest Maxing Power Point 79
5.1 Highest Power-Generating Receiver 79
5.2 Maximum Power Point 81
  5.2.1 Optimal Receiver Voltage 81
  5.2.2 Optimal Transfer Frequency 88
  5.2.3 Maximum Output Power 96
5.3 Measurements 98
  5.3.1 Prototype 98
  5.3.2 Optimal Settings 99
  5.3.3 MPP Error 100
5.4 Discussions 102

CHAPTER 6. Synchronizing Controller 104
6.1 Self-Synchronized Switched Resonant Half-Bridge 104
  6.1.1 System Operation 104
  6.1.2 Maximum Power Point 106
6.2 Circuit Implementation 108
  6.2.1 Synchronizing Comparator 108
  6.2.2 Current Reference 110
  6.2.3 MPP Control 111
6.3 Measurements 113
  6.3.1 Prototype 113
  6.3.2 Charge Profile & Ideality Index 116
  6.3.3 Relative Performance 120
6.4 Discussion: Inductively Coupled vs. RF 123
  6.4.1 Inductively Coupled 123
  6.4.2 RF 125
  6.4.3 Comparison: An Example 127

CHAPTER 7. Conclusions 130
7.1 Research Objective 130
7.2 Contributions 131

7.2.1 Evaluation of the SoA Power Receivers 131
7.2.2 MPP Power Stage 133
7.2.3 MPP Theory 135
7.2.4 System Integration 137
7.3 Remaining Challenges & Future Research 139
7.3.1 Zero-Energy Start-up 140
7.3.2 Maximum Power Point Tracking (MPPT) 141
7.4 Summary 144

LIST OF TABLES

Table 1-1. Summary of embedded microsensor applications. 5

Table 1-2. Comparison of energy storage. 8

Table 1-3. Summary and comparison of ambient energy sources 10

Table 1-4. Summary of Energy Sources For Embedded Microsensors 16

Table 3-1. Comparison of SoA power receivers. 57

Table 4-1. Parameter Summary 65

Table 4-2 Relative performance of the proposed power receiver. 76

Table 5-1. MPP Settings Summary 102

Table 6-1. Relative Performance 122

Table 6-2. Parameters for the inductively coupled and RF system. 128

LIST OF FIGURES

Figure 1-1. Implanted blood pressure monitoring MEMS sensor. 1

Figure 1-2. Implanted wireless blood glucose monitoring system. 2

Figure 1-3. Microsystem that senses pressure, temperature, and humidity. 4

Figure 1-4. Multilayer ceramic capacitor... 8

Figure 1-5. Inductively coupled coils for wireless power transfer 12

Figure 1-6. Inductively coupled wireless power transfer for embedded microsystems. .. 13

Figure 1-7. RF wireless power transfer system. 14

Figure 2-1. Inductively coupled receiver coil generates an EMF voltage. 18

Figure 2-2. COMSOL simulated cross-sectional magnetic field near the transmitter coil. 19

Figure 2-3. Calculated and simulated magnetic field along d_X....................................... 19

Figure 2-4. Circuit model of an inductively coupled power transfer system................... 22

Figure 2-5. Equivalent transmitter model. 23

Figure 2-6. Equivalent receiver model... 24

Figure 2-7. Equivalent receiver circuit when closely coupled... 27

Figure 2-8. Equivalent receiver circuit when loosely coupled. 28

Figure 2-9. Maximum receiver power as a function of k_C^2... 30

Figure 2-10. Power model of the inductively coupled power system.............................. 32

Figure 2-11. Simulated waveforms with and without receiver voltage v_R. 33

Figure 2-12. Simulated receiver power as a function of v_R. 34

Figure 3-1. The resonant full-bridge power receiver. 38

Figure 3-2. Waveform of the resonant full-bridge. 38

Figure 3-3. Comparator based PMOS and NMOS switches.. 41

Figure 3-4. Resonant full-bridge with cross-coupled NMOS pair.................................. 41

Figure 3-5. Resonant half-bridge power receiver. 42

Figure 3-6. Waveform of the resonant half-bridge. 43

Figure 3-7. Multiplying charge pump. 45

Figure 3-8. Non-investing switched bridge. 46

Figure 3-9. Waveforms of the non-investing switched bridge. 46

Figure 3-10. The investing switched bridge power receiver.. 48

Figure 3-11. Waveforms of the investing switched bridge. 49

Figure 3-12. Serially drained switched resonant bridge power receiver. 51

Figure 3-13. Waveforms of the switched resonant bridge. 52

Figure 3-14. Skipped operation of the serially drained switched resonant bridge........... 52

Figure 3-15. Directly drained switched resonant bridge power receiver. 53

Figure 3-16. Waveforms of the directly drained switched resonant bridge. 53

Figure 3-17. Simulated v_E's drawn power. 54

Figure 3-18. Simulated receiver power P_L. 55

Figure 4-1. Proposed switched resonant half-bridge power receiver. 59

Figure 4-2. Waveforms of the non-skipping proposed switched resonant half-bridge..... 60

Figure 4-3. Waveforms of the skipping proposed switched resonant half-bridge. 60

Figure 4-4. Measured output-power space when the coils are 16 mm apart. 66

Figure 4-5. Measured output-power space when the coils are 29 mm apart. 67

Figure 4-6. Measured maximum power when adjusting one and two variables. 68

Figure 4-7. Simulated sensitivity of output power to tuning accuracy. 69

Figure 4-8. Photograph of the fabricated power stage IC. 70

Figure 4-9. Photograph of the power transmitter and receiver boards. 70

Figure 4-10. Photograph of the linear adjusting stage. 71

Figure 4-11. Measured losses and resulting maximum power. 72

Figure 4-12. Measured charging profile of the switched resonant half-bridge. 73

Figure 4-13. Available and measured output power and resulting ideality index. 75

Figure 4-14. FPGA synchronizes the transmitter and the receiver. 78

Figure 5-1. Switched resonant half-bridge for highest MPP. 80

Figure 5-2. Energy transfer frequency, duration, and offset of a switched resonant half-bridge power receiver. 80

Figure 5-3. Power model of the switched resonant half-bridge power receiver. 82

Figure 5-4. Ideal receiver voltage v_R to maximize receiver power. 82

Figure 5-5. Receiver voltage v_R of a switched resonant half-bridge. 82

Figure 5-6. Output power across offset time. 86

Figure 5-7. Maximum output power and receiver's peak f_O harmonic voltage. 86

Figure 5-8. Output power across duration. 87

Figure 5-9. Optimal duration. 88

Figure 5-10. $v_{C(PK)}$ deviates from $v_{C(OPT)}$ in the switched resonant half-bridge skipping operation. 89

Figure 5-11. Drawn power and resulting nonlinear loss. 90

Figure 5-12. Simulated capacitor voltage across uncollected cycles. 92

Figure 5-13. Losses and resulting optimal transfer frequency. 96

Figure 5-14. Optimized output power. 97

Figure 5-15. Variable space for output power. 98

Figure 5-16. Measured waveforms at MPP. 99

Figure 5-17. Optimal duration and number of cycles between transfers. 100

Figure 5-18. P_O at the predicted MPP setting and the actual MPP setting. 101

Figure 6-1. Switched resonant half-bridge wireless charger. 105

Figure 6-2. Simulated wireless charger waveforms at 150 mV $v_{E(PK)}$. 106

Figure 6-3. Measured P_O across $v_{E(PK)}$ and f_X. 107

Figure 6-4. High voltage sensing with (a) resistive voltage divider and (b) variable-ratio voltage divider. 108

Figure 6-5. Synchronizer circuit with voltage divider. 109

Figure 6-6. Simulated output curve of the voltage divider. 110

Figure 6-7. PTAT current source. 111

Figure 6-8. 6-bit digital delta sigma skip control. 112

Figure 6-9. Operation of the DSM MPP controller. 112

Figure 6-10. Photos of the wireless charger IC. 113

Figure 6-11. Photos of the wireless charger PCB. 114

Figure 6-12. Linear stage that controls the distance between the transmitter and receiver coils. 114

Figure 6-13. Measurement setup. 115

Figure 6-14. Measured MPP receiver waveforms when k_C = 0.15%. 115

Figure 6-15. Measured MPP receiver waveforms when k_C = 1.1%. 116

Figure 6-16. Measured charging waveforms at 13~28 mm distance. 117

Figure 6-17. Measured ideality factor across power transmission distance d_X. 118

Figure 6-18. Measured $f_{X(MPP)}$ across $v_{E(PK)}$. 119

Figure 6-19. Loss breakdown of the self-synchronized power receiver. 119

Figure 6-20. Measured ideality index. 121

Figure 6-21. Inductively coupled power transfer system. 124

Figure 6-22. Calculated and circuit simulated $P_{O(MAX)}$ at different $v_{E(PK)}$. 125

Figure 6-23. Dipole antenna momentary electric field. 126

Figure 6-24. Dimensions of the L-coupled and RF transmitters and receivers. 128

Figure 6-25. Comparison between inductively coupled RF power density attenuation over distance. 129

Figure 7-1. Applying an alternating high voltage v_R boosts i_L and power from v_E. 131

Figure 7-2. The switched resonant half-bridge that adjusts both energy transfer duration and frequency for MPP. 134

Figure 7-3. Adjusting both t_{ON} and f_X for MPP with 39 mV coupled voltage. 134

Figure 7-4. P_O at the theory's predicted setting and the actual $P_{O(MPP)}$. 137

Figure 7-5. Self-synchronized switched resonant half-bridge power receiver. 138

Figure 7-6. Startup the switched resonant half-bridge with the help of C_{PAR}. 141

Figure 7-7. MPPT by calibrating coupled voltage and using look-up table. 143

SUMMARY

Inductively coupled power transfer can extend the lifetime of embedded microsensors that save costs, energy, and lives. To expand the microsensors' functionality, the transferred power needs to be maximized. Plus, the power receiver needs to handle wide coupling variations in real applications. Therefore, the objective of this research is to design a power receiver that outputs the highest power for the widest coupling range. This research proposes a switched resonant half-bridge power stage that adjusts both energy transfer frequency and duration so the output power is maximally high. A maximum power point (MPP) theory is also developed to predict the optimal settings of the power stage with 98.6% accuracy. Finally, this research addresses the system integration challenges such as synchronization and over-voltage protection. The fabricated self-synchronized prototype outputs up to 89% of the available power across 0.067%~7.9% coupling range. The output power (in percentage of available power) and coupling range are 1.3× and 13× higher than the comparable state of the arts.

CHAPTER 1. EMBEDDED MICROSENSORS

1.1 Applications

With the advancement in micro-electromechanical systems (MEMS) technology, sensors can now be miniaturized onto a millimeter-scale semiconductor chip to collect information from the physical world. An embedded microsensor system often combines the miniaturized sensor with an interface integrated circuit (IC) so the collected information can be processed locally and transmitted to other devices. The embedded microsensors are often small in millimeter-scale, as the MEMS devices and interfaces ICs are often packaged together. MEMS devices can be built on a CMOS IC substrate as well, so the whole embedded microsensor system can be integrated on a single chip to further reduce the size [1-3]. Also, as the MEMS devices and ICs are fabricated with the standard, batch-built process, their cost is low. The small form factor allows the embedded microsensors to collect information in places difficult to reach. And the low cost allows them to be distributed in large quantities or even to form a wireless sensor network [4-6].

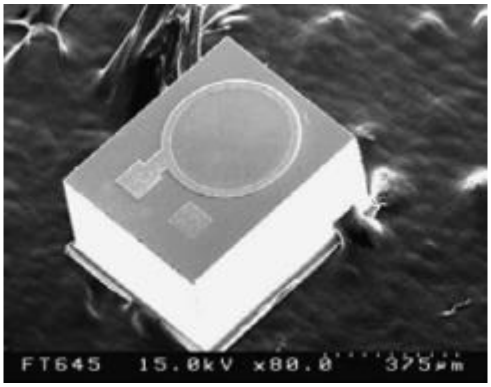

Figure 1-1. Implanted blood pressure monitoring MEMS sensor.

1.1.1 Biomedical Implants

The tiny embedded wireless microsensors can be implanted in human or animal bodies to monitor the body information or assist the body activity [7, 8]. The pressure sensor shown in Figure 1-1 utilizes the silicon diaphragm's capacitive feature to measure the pressure [9]. The sensor is then attached to a cuff that surrounds the lab animal's vessel to provide constant pressure monitoring. The implanted microsensor can monitor blood glucose levels as well. The glucose monitoring system in [10], as shown in Figure 1-2, integrates the glucose sensor, the readout circuit, and the communication module onto a 4 mm × 8 mm printed circuit board (PCB). The readout circuit converts the sensor output to digital numbers, and the readout numbers are sent to the master device via an inductive data link. The embedded microsensors are also found in a wide range of other biomedical implant applications as well, including neuro monitoring/stimulation [11-15], endoscopy [16-18], intraocular pressure sensing [1, 19-21], drug delivery control [22, 23], electrocardiogram [24], and other biomedical readout applications [24-26].

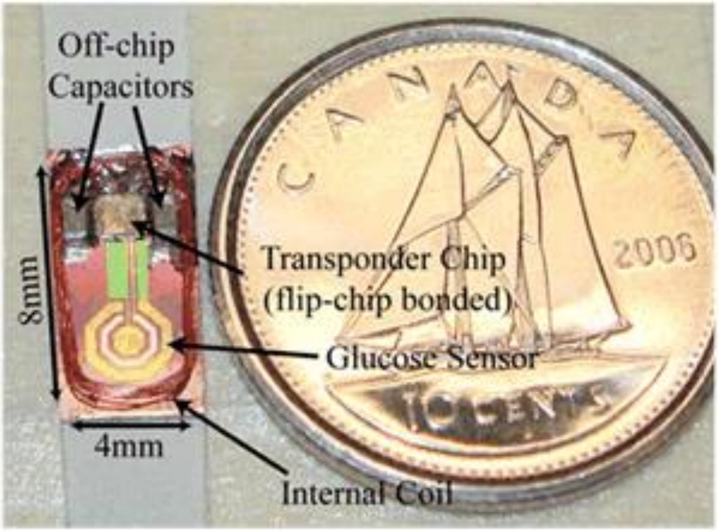

Figure 1-2. Implanted wireless blood glucose monitoring system.

1.1.2 Structure/Material Monitoring

Besides biomedical implant applications, embedded microsensors are also widely used in monitoring structural health in a wireless fashion. In [5] and [27], a bunch of embedded microsensors are distributed at the critical structural points of the architecture. Each microsensor monitors the displacement of one component. A test vehicle or “host” charges each microsensor wirelessly as it passes by and collects information in an as-need fashion. Embedded microsensors are also used in aircraft to monitor any cracks or deformation [28, 29]. Similar microsensors are found embedded in materials and buildings as well [30, 31]. Their tiny form allows them to be embedded in the materials in large quantities. And they are often powered wirelessly to avoid the complex wiring [30, 32, 33].

1.1.3 Environment Sensing and Other Applications

Embedded microsensors are also used for sensing the environment parameters [34-39]. The embedded microsystem in [35], as shown in Figure 1-3 integrates the pressure, temperature, and humidity sensors, as well as the signal processing and transmitting/receiving circuits on a single silicon die. The tiny integrated microsystem can be distributed in the soil and powered wirelessly and instantaneously when an interrogating device is nearby. Microsensors that detect light or chemicals are used for imaging as well [40, 41]. The sensed image data can be processed on-chip with only microwatts of power [41].

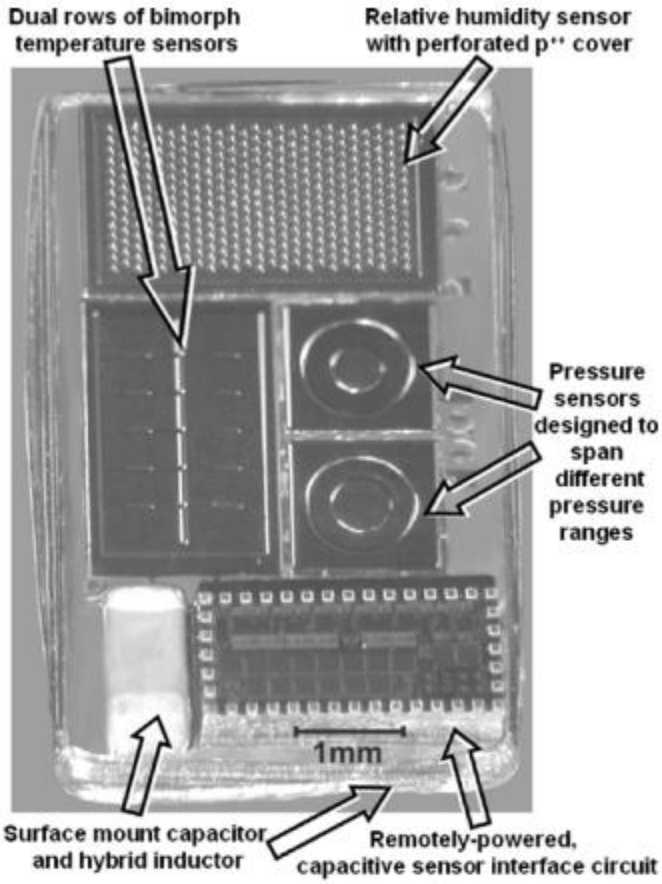
Dual rows of bimorph temperature sensors
Relative humidity sensor with perforated p⁺⁺ cover
Pressure sensors designed to span different pressure ranges
1mm
Surface mount capacitor and hybrid inductor
Remotely-powered, capacitive sensor interface circuit

Figure 1-3. Microsystem that senses pressure, temperature, and humidity.

1.1.4 Summary

Table 1-1 summarizes and compares the power consumption and sizes of different embedded microsensor applications. Most embedded microsensors take up to a few tens of millimeter square, except the aircraft structural health monitor sensor in [29], which takes 63 × 32 mm^2. The power consumption of these embedded microsensors ranges from microwatts to milliwatts, with the highest consuming 78 mW.

Table 1-1. Summary of embedded microsensor applications.

	Application	Power	Size	Reference
Biomedical Implants	Neuro-monitor /Neuro-stimulator	5.8 mW	5.8 mm^2	[11]
		5.9 mW	4.9 × 3.3 mm^2	[12]
		13.5 mW	27.3 mm^2	[15]
	Intraocular aid	–	4 × 1.5 mm^2	[21]
		180 µW	6.76 mm^2	[1]
	Blood flow monitoring	12.6 µW	0.5 × 3.3 mm^2	[42]
	Glucose monitoring	200 µW	4.2 mm^2	[10]
	Blood pressure monitoring	300 µW	2.2 × 2.2 mm^2	[9]
	Drug delivery	7.2 mW	2.48 mm^2	[23]
	Electrocardiogram /Electromyogram /Electroencephalogram	19 µW	2.5 × 3.3 mm^2	[24]
Structural Monitoring	Aircraft structural health monitoring	2.9 mW	–	[28]
		78 mW	63 × 32 mm^2	[29]
Environment Sensing	Pressure, humidity and temperature sensing	341µW	32 mm^3	[35]
	Humidity sensing	1.39 mW	4.8 mm^2	[43]
	Pressure monitoring	33 mW	1 cm^3	[38]
		5 mA	2 × 1.5 mm^2	[39]
Imaging System	Microfluidic chemiluminescence contact imaging	–	2.9 × 2.7 mm^2	[40]
	Vision sensor	33 µW	26 × 26 µm^2	[41]

1.2 Powering Embedded Microsensors

1.2.1 Energy Storage

Lifetime is one of the biggest challenges for embedded microsensors. Battery technology has gone through a long way during the past decades [44]. However, the energy density is still relatively low compared to the fast-growing demand. Among all battery types, the lithium-ion (Li-ion) batteries are the most popular due to their high energy density and mature manufacturing technology [45, 46]. The energy density of Li-ion batteries can be as high as 110-175 Wh/kg [45]. With this density, a 1-gram Li-ion battery can supply a 100 μW microsensor up to 73 days. While a 73-day lifetime is quite enough for consumer electronics, it is insufficient for many embedded microsensor applications. Replacing the battery in biomedical implants require surgery, which is both costly and painful for the patients or the lab animals. Replacing the batteries in structural health monitoring microsensors can be costly too, as they are often deployed in large quantities at places difficult to reach [27, 29, 33, 47, 48].

To extend the lifetime of the embedded microsensor, the onboard battery needs to be replenished. As the batteries on the embedded microsensors are tiny, they deplete easily and requires recharging from time to time. Most Li-ion batteries can fully recharge up to 1000 cycles before the battery capacity severely deteriorates [45, 49, 50]. However, this may still be insufficient. For many biomedical implants, the energy source is not always available, the implants need to take every chance to recharge their battery to ensure robust operation. Frequent recharging severely reduces the battery’s capacity.

The alkaline battery, commonly found in household and commercial applications, provides a cheaper alternative to the Li-ion battery. An alkaline battery uses the chemical reaction between the negative electrode (often zinc) and the alkaline to generate electrical charges. The energy density of an alkaline battery is typically lower than that of Li-ion at 50–120 Wh/kg [51]. Note not all alkaline batteries are designed for rechargeable use. However, some reported state-of-the-art alkaline batteries can recharge up to 6000 cycles [52, 53]. Zinc-carbon battery is another commonly used battery. Compared to the alkaline battery, the zinc-carbon battery's energy density is even lower at 85 Wh/kg [54]. However, the zinc-carbon battery is non-rechargeable, which limits its applications in embedded microsensors.

In terms of recharge cycles, the supercapacitor is much superior. The supercapacitor can recharge 20,000 to 100,000 times without significant capacitance degradation [55, 56], which is up to 100 times better than the Li-on battery. The graphene-based supercapacitor in [56] reports an energy density of 10 Wh/kg, which is an order of magnitude less than the Li-ion battery. The main drawback of the supercapacitor is its leakage. A charged supercapacitor can lose 60% of the voltage in a day [57].

A simple capacitor can be an energy storage as well. Ceramic capacitors often use multilayers to increase the capacitance per package, as shown in Figure 1-4 [58]. A state-of-the-art multilayer ceramic capacitor (Murata GRM31CD80J107ME39_) can pack 100 μF of capacitance into $3.2 \times 1.6 \times 1.6$ mm^3 of space. However, the energy density of the capacitor is very low (2–10 Wh/kg [59]) compared to other forms energy storage. Recharge cycles of capacitor are practically unlimited for embedded microsensor applications.

Capacitors in 60 Hz AC systems charges and discharges millions of times a year, which far exceeds the requirement of embedded microsensor applications.

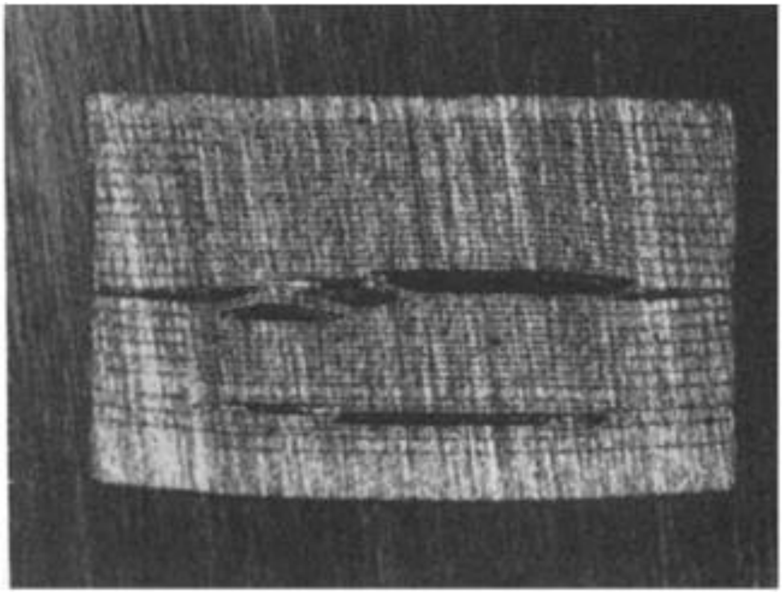

Figure 1-4. Multilayer ceramic capacitor.

Table 1-2. Comparison of energy storage.

Energy Storage	**Energy Density (Wh/kg)**	**Recharge Cycles**	**Remarks**
Li-ion Battery	110-175 [45]	~1000 [45, 49, 50]	–
Alkaline Battery	50–120 [51]	~6000 [52, 53]	–
Zinc-Carbon	85 [54]	Non-rechargeable	Not suitable for microsensor applications
Supercapacitor	10 [56]	20,000–100,000	High leakage
Capacitor	~0.5[59]	Practically unlimited	Low energy density

Table 1-2 summarizes and compares energy density and recharge cycles of different energy storage. Capacitors and supercapacitors have the highest recharge cycles but low energy density. Therefore, they are suitable for applications where energy storage needs to be recharged frequently. Li-ion and rechargeable alkaline batteries, on the other hand, have high energy density but low recharge cycles. They are suitable for applications where a single charge needs to last for hours or days. Non-rechargeable alkaline and zinc-carbon batteries are not suitable for embedded microsensor applications.

1.2.2 Harvesting Ambient Energy

To recharge the microsensor's battery, an energy source is required. The charging needs to be wireless, as charging through a cable defeats the purpose of the embedded operation. One option is to harvest energy from the ambiance, such as light, motion, and temperature difference.

Energy from light can be converted to electrical charges via a photovoltaic cell. Under direct sunlight, the converted power density can be as high as 3 W/cm^2 [60]. Under the indoor condition, the power density number drops to 0.5–1 mW/cm^2 [61]. Although the indoor power density is much lower compared to the outdoor, the power converted is still sufficiently high for microwatt microsensor applications in Table 1-1. Unfortunately, light is rarely available in many embedded microsensor applications. Biomedical implants are normally buried underneath the skin, so they hardly receive any light. Structural and environment monitoring sensors are often embedded in the materials or buried in the earth, so light is unavailable neither.

Motion is another harvestable ambient energy source. Motion energy can be converted to electric charge using a piezoelectric converter [47, 62-64], a magnetic harvester [65-67], or an electrostatic harvester [59, 68, 69]. Out of the three converting methods, the piezoelectric harvester usually outputs the highest power density up to 400 µW [59]. Motion energy is available in some embedded microsensor applications. For example, the blood flow monitoring sensor can utilize the energy carried in the blood pulse. Some structural health monitoring microsensors can utilize the energy in architecture vibration. However, for some other embedded microsensor applications, motion energy is scarce. The environment monitoring microsensors in [35] are buried in soil and can hardly retrieve any motion energy. Also, biomedical implants such as the vision and intraocular sensors [1, 12, 19, 21, 41] are exposed to little motion energy. For embedded microsensor applications where little to no motion energy is available, an alternative energy source is needed.

Table 1-3. Summary and comparison of ambient energy sources

Energy Source	**Conversion Mechanism**	**Power Density (in 1cm^2 or cm^3)**	**Challenges**
Light	Photovoltaic	Outdoor: < 3W [60] Indoor: 0.5–1 mW [61]	Not available for many applications
Motion	Piezoelectric	< 400 µW [59]	Only available for some applications
	Magnetic	1–100 µW [59]	
	Electrostatic	1–100 µW [59]	
RF Radiation	Antenna Rectification	10–100 nW [59]	Low power density
Thermal	Seebeck	1–6 µW [70]	Low power density

Besides light and motion, energy can be harvested from other energy sources as well. Cellular and WiFi radiation carries power that can be harvested. However, the RF signal is normally weak and the harvested power is often low in nanowatt range [59]. The temperature difference can also generate power. Using the Seebeck effect, a thermoelectric generator converts a temperature difference into a voltage source [71]. However, the converted power is low in density. With a 5–10 K temperature difference, the converted power density is only 1–6 μW/cm^2 [70].

Table 1-3 summarizes and compares the possible ambient energy sources for embedded microsensors. The power density from RF generators and thermoelectric generators are too low for most embedded microsensor applications. The outdoor light provides the highest power density up to a few watts. However, light is rarely available in an embedded environment. The motion energy generates moderate power density (< 400 μW), which is enough for some applications. However, motion energy is not always available. To expand the application space of embedded microsensors, an alternative energy source is necessary.

1.2.3 Wireless Power Transfer

When the ambient energy is not available, the only option left is to recharge the battery wirelessly using a dedicated source. Transmitting power wirelessly over a long distance often involves using either a pair of inductively-coupled coils [72-75] or RF antennas [76, 77]. Although power can also be transferred via capacitive coupling, the power transmission distance is often as short as a few millimeters [78, 79], which is impractical for most embedded microsensor applications.

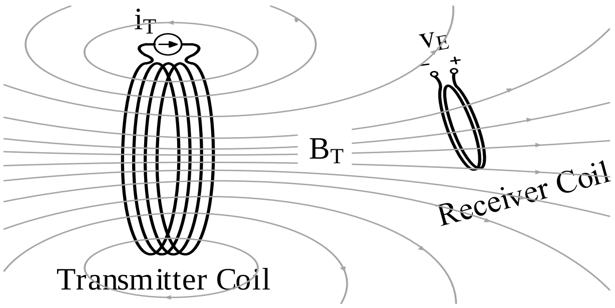

Figure 1-5. Inductively coupled coils for wireless power transfer

Inductively coupled power transfer utilizes a pair of coils to transfer power [80]. The transmitting coil L_T in Figure 1-5 runs an AC current i_T and generates a changing magnetic field B_T in the nearby space. The receiving coil L_R captures the magnetic flux that L_T emits and induces an electromotive force (EMF) voltage v_E. A power receiver extracts power from v_E to charge the energy storage.

Figure 1-6 shows a typical inductively powered embedded microsensor system. The transmitting coil L_T inductively couples an EMF voltage $v_{E(R)}$ on the receiving coil L_R. The power receiver conditions and rectifies the inductor current i_L to charge up the energy storage v_B. which supplies the microsystem's components, such as sensors, amplifiers, DSPs, wireless communication, etc. Out of all system components, the wireless communication block often consumes the highest power [24]. Combining the receiver and supply stages into one stage is possible and can improve efficiency when the load is active [81-84]. However, most embedded microsensors are heavily duty-cycled to conserve energy [24]. Eliminating the intermediate energy storage v_B means the power received when the load idles is wasted, so the averaged efficiency is low.

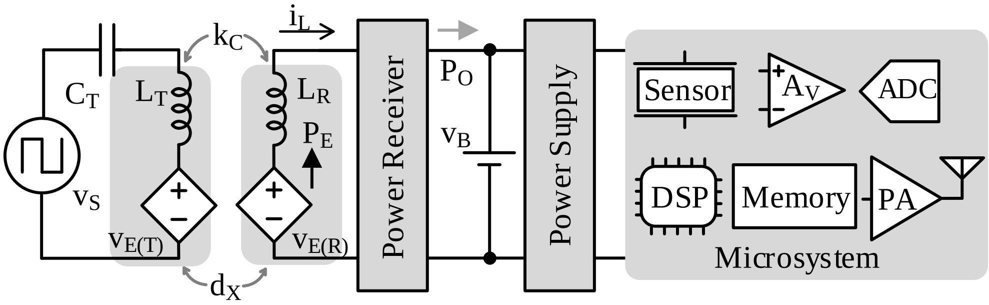

Figure 1-6. Inductively coupled wireless power transfer for embedded microsystems.

Powering embedded microsensors using a pair of inductively coupled coils is challenging for several reasons. First, the stringent size constraint in many embedded microsensor applications requires the receiver coil to be tiny. These tiny coils, often in millimeter-scale, measure only a fraction of the power transmission distance. So the power transmission radial distance is large. As a result, the tiny coils often couple only millivolts, from which drawing sufficient power is difficult. Also, because of their tiny size, the receiver coils are resistive, so the ohmic loss on the coil is high, limiting the maximum power the receiver can draw. Finally, although increasing the transmitting power avails more power to the receiver. The maximum transmitting power is limited by the safety standard. IEEE Standard for Safety Levels with Respect to Human Exposure to Electric, Magnetic, and Electromagnetic Field, 0 Hz to 300 GHz [85] specifies the safe magnetic field levels for the human brain, limbs, and whole body.

The RF wireless transfer [86-94], on the other hand, uses a pair of antennae to transfer power. In an RF system, a power amplifier drives the transmitting antenna that radiates P_T, as Figure 1-7 shows. The receiver captures a fraction of P_T. A matching network minimizes the reflection power on the receiving antenna, so P_O is maximum. The current from the receiving antenna is rectified to charge v_B. A dedicated RF power transfer system does not require data communication blocks such as the modulator, demodulator, or mixers.

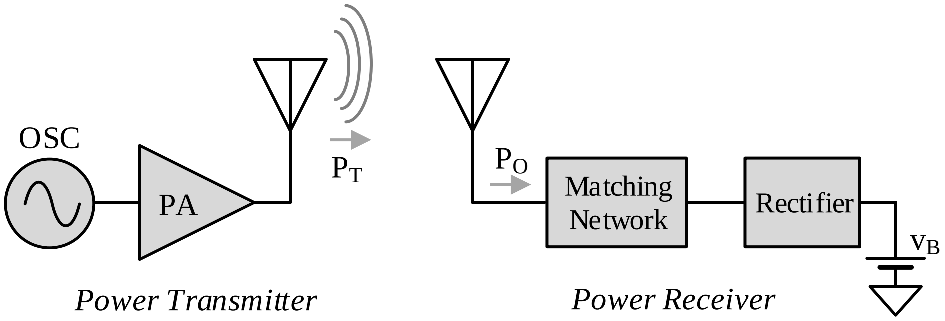

Figure 1-7. RF wireless power transfer system.

Both inductively coupled and RF can transfer power wirelessly. When the power transmission distance is long, the inductively coupled power decays with distance to the power of 6, while RF power decays quadratically with distance. So, RF power is higher. When the power transmission distance is short, the inductively coupled power receiver theoretically can receive all the power the transmitter avails. On the other hand, RF power always radiates into space. So, at a shorter distance, inductively coupled power is higher. A more detailed quantitative comparison between the two wireless technologies will be discussed in Chapter 6.

1.2.4 Summary

Table 1-4 compares different energy source options for embedded microsensor applications. The first option is to use energy storage, such as a battery or a supercapacitor to supply the microsensor system. The power density of these energy storage is practically unlimited for the targeted applications, as most embedded microsensors require only microwatts to milliwatts of power, according to the summary in Table 1-1. However, the energy density of these energy storage is limited. The Li-ion battery has the highest energy density of 110-175 Wh/kg. But still, a 1-gram Li-thion battery can supply a 100 µW microsensor up to 73 days. Replacing the battery can be costly or even impractical in some cases. Therefore, the second option is to harvest ambient energy, such as light or motion, to recharge the energy storage. Although some energy harvesting methods generate moderate to high power, the harvestable energy source is not always available is an embedded environment. So with the absence of ambient energy source, the only option left is to transfer power wirelessly via a pair of inductively coupled coils or RF antennae. In the near field (up to a few radial distances), the inductively coupled power is higher as it does not emit power into space. However, in the far-field, the inductively coupled power decays 3 times faster than the RF. So RF is more suitable for far-field applications [95].

Table 1-4. Summary of Energy Sources For Embedded Microsensors

Energy Source		Energy Density (Wh/kg)	Power Density (cm^{-2} or cm^{-3})	Remarks
Energy Storage	Li-ion Battery	110-175 [45]	Practically Unlimited	~1000 cycles [45, 49, 50]
	Alkaline Battery	50–120 [51]		~6000 cycles [52, 53]
	Zinc-Carbon Battery	85 [54]		Non-rechargeable
	Super-capacitor	10 [56]		20,000–100,000 cycles; High leakage.
	Capacitor	~0.5 [59]		Practically unlimited cycles
Energy Harvester	Photovoltaic (Outdoor)	Practically Unlimited	< 3W [60]	Source rarely available
	Photovoltaic (Indoor)		0.5–1 mW [62]	
	Piezoelectric		< 400 µW [59]	Source not always available
	Magnetic		1–100 µW [59]	
	Electrostatic		1–100 µW [59]	
	WiFi or Cellular		10–100 nW [59]	Low power density
	Thermal		1–6 µW [69]	Low power density
Wireless Power Transfer	Inductively coupled	Practically Unlimited	Scales w/ distance and source	Requires nearby source. Power decays 3 times faster than RF in the far field.
	RF Radiation			Requires nearby source. Loses power into space in the near field.

CHAPTER 2. INDUCTIVELY COUPLED POWER TRANSFER

2.1 Inductive Coupling

When the transmitter coil in Figure 2-1 flows a current i_T, it generates a magnetic field in the nearby space, according to Ampère's Law. To generated magnetic field can be quantitatively determined by integrating each infinitesimal length of coil's magnetic effect using the Bio-Savart's Law:

$$\overrightarrow{B_T} = \frac{\mu_C}{4\pi}\int_C \frac{I_T d\vec{l} \times \vec{r}}{|r|^3}. \tag{2.1}$$

Here $\vec{r}$ in Eq. (2.1) is the vector from the infinitesimal length of the coil $d\vec{l}$ to the point to be measured, and $|r|$ is the length of $\vec{r}$. μ_C is the permeability of the medium. For most embedded microsensor applications, to maximize the coupling, the coils are often aligned in the center like in Figure 2-1 and the transmitting coil's radius r_T is often much larger than r_R of the receiving coil. With these assumptions, the magnetic field passes the receiver coil along the center axle d_X can be calculated as [96]:

$$B_T = \frac{0.5\mu_C N_T i_T r_T{}^2}{\left(r_T{}^2 + d_X{}^2\right)^{1.5}}, \tag{2.2}$$

where N_T is the number of turns in the transmitter coil. When the distance d_X is much higher than the transmitter coil's radius d_T, the generated magnetic field BT drops cubically with d_X:

$$B_T\Big|_{d_X >> R_T} \approx \frac{0.5\mu_C N_T i_T r_T{}^2}{d_T{}^3} \propto \frac{1}{d_T{}^3}\,. \qquad (2.3)$$

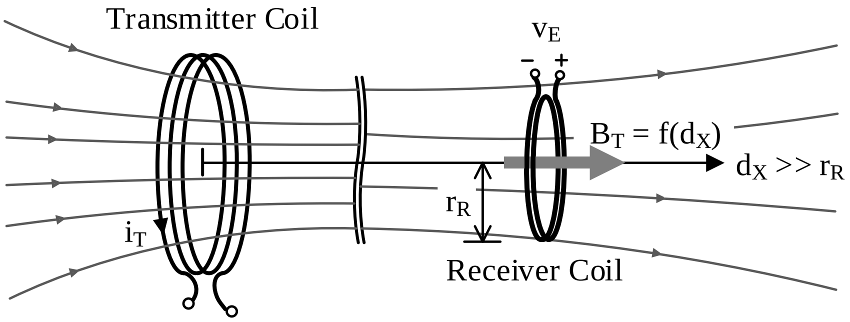

Figure 2-1. Inductively coupled receiver coil generates an EMF voltage.

To validate the B_T calculation in Eq. (2.2), the magnetic field generated by a 250-turn, 4.3 cm diameter coil is simulated using COMSOL Multiphysics FEM tool. Figure 2-2 shows the simulated B_T of a half cross-sectional plane that is perpendicular to the coil. The color in Figure 2-2 represents B_T's magnitude while the lines show B_T's direction. The simulated B_T strength along the d_X axle is compared with the calculation in Figure 2-3. Below 5.6 d_T of distance, the calculation from Eq. (2.2) matches the simulated results within ±3% error. Beyond that, due to the dynamic range limit of the simulation, the error increases to ±10%.

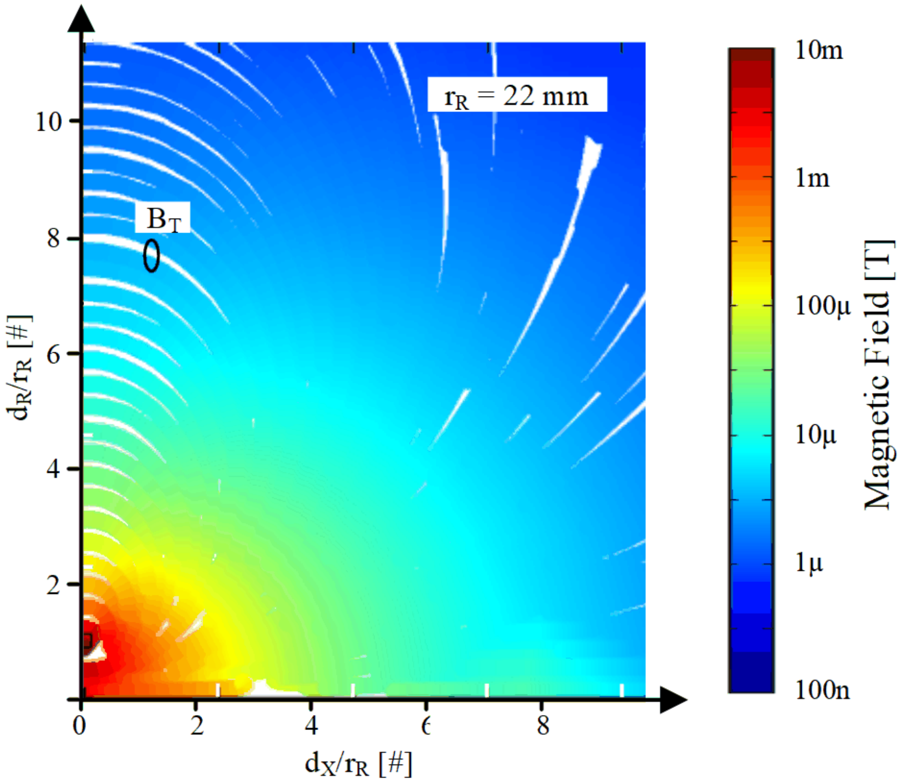

Figure 2-2. COMSOL simulated cross-sectional magnetic field near the transmitter coil.

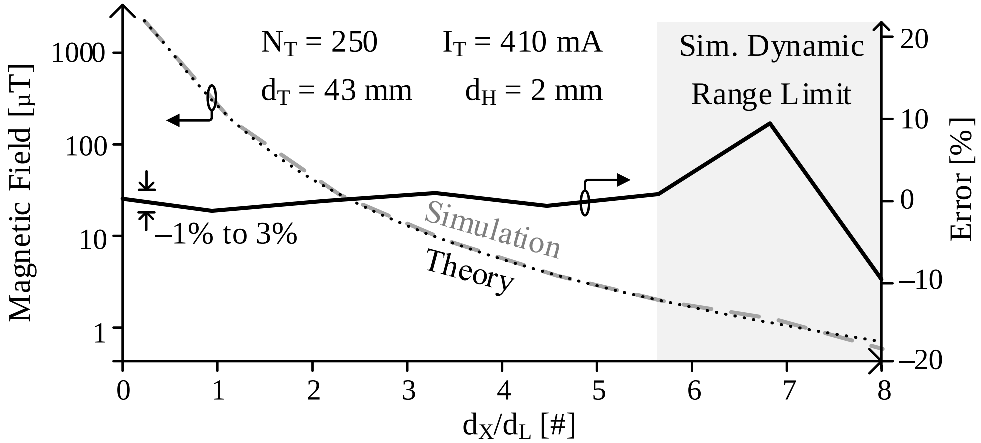

Figure 2-3. Calculated and simulated magnetic field along d_X.

The receiver coil in Figure 2-1 captures the magnetic flux that the transmitter coil emits. According to the Faraday's Law, the changing magnetic flux that goes through the receiver coil couples an open-circuit electromotive force (EMF) voltage v_E on the receiver coil:

$$v_E = \frac{\partial \Phi_{RT}}{\partial t} = \frac{\partial \left(B_T A_R N_R \right)}{\partial t} \propto \frac{di_T}{dt} . \tag{2.4}$$

From Eq. (2.3) and Eq. (2.4), the captured magnetic flux Φ_R is proportional to i_T:

$$v_E \propto \frac{\frac{di_T}{dt}}{\left(r_T{}^2 + d_X{}^2 \right)^{3/2}} \propto i_T . \tag{2.5}$$

When the power transmission distance d_X is much larger than the transmitter radius r_T, induced v_E drops quickly with distance:

$$v_E \propto \frac{1}{d_X{}^3} . \tag{2.6}$$

The self-inductance of an inductor is defined by the magnetic flux a unit current can generate from its inductor, so for the transmitter and receiver coil:

$$\Phi_T = L_T i_T , \tag{2.7}$$

$$\Phi_R = L_R i_T . \tag{2.8}$$

The mutual inductance M_C, on the other hand, is the magnetic flux that a unit current can generate from another inductor:

$$\Phi_{TR} = M_C i_R , \tag{2.9}$$

$$\Phi_{RT} = M_C i_T , \tag{2.10}$$

Note the mutual inductance M_C in Eq. (2.9) and Eq. (2.10) are the same [97]. This means with the same current i_R and i_T, the transmitter generates as much magnetic flux on the receiver as the receiver generates on the transmitter. The coupling factor k_C indicates, on geometric average, how much generated magnetic reaches the other coil, both from the transmitter to the receiver, and from the receiver to the transmitter:

$$k_C = \sqrt{\left(\frac{\Phi_{RT}}{\Phi_T}\right)\left(\frac{\Phi_{TR}}{\Phi_R}\right)} = \frac{M_C}{\sqrt{L_T L_R}}\ , \tag{2.11}$$

Since the captured magnetic flux is always a fraction of the emitted magnetic flux, $k_C < 1$.

2.2 *Circuit Model*

Figure 2-4 shows the circuit model of an inductively coupled power system. An AC source v_S with source resistance R_S drives current to the transmitting coil L_T. According to the maximum power transfer theorem [98], to deliver the maximum power to L_T, the reactive components of the source and load must be equal in magnitude but opposite in sign. For this, a resonant capacitor C_T is added so its impedance $\left(\frac{1}{jC_T\omega_O}\right)$ cancels that of L_T $\left(jL_T\omega_O\right)$. Or more intuitively, as C_T and L_T resonate at v_S' frequency f_O, the resonation amplifies the L_T's current i_T to its maximum. So the power to L_T is also maximum. The effective series resistance of L_T is R_T at f_O. The resonating current i_T couples a closed-loop EMF voltage $v_{E(R)}$ on the receiver coil L_R. From (2.4) and (2.10), the coupled $v_{E(R)}$ can be calculated as:

$$v_{E(R)} = \frac{\partial \Phi_{RT}}{\partial t} = M_C \frac{di_T}{dt}\ . \tag{2.12}$$

The induced EMF voltage is reciprocal: when the receiver is closed-circuited, the receiver current i_R also induces an EMF voltage $v_{E(T)}$ on the transmitter side. Similarly, the EMF voltage the receiver induces back on the transmitter can be obtained as:

$$v_{E(T)} = \frac{\partial \Phi_{TR}}{\partial t} = M_C \frac{di_R}{dt}. \tag{2.13}$$

Similar to the transmitter, the receiver also uses a resonate capacitor C_R to maximizes the power to the load Z_L.

The circuit model in Figure 2-4 is a complete and symmetrical model in a closed-form. However, the transmitter's IV and the receiver's IV are interrelated by (2.12) and (2.13), which makes the analysis complicated and unintuitive. An alternative approach is to decouple the transmitter and receiver by replacing the coupling with their equivalent load, respectively.

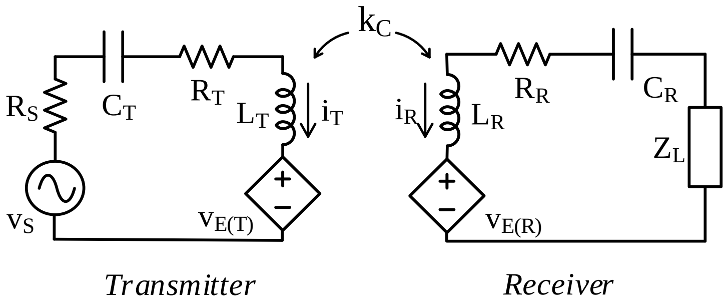

Figure 2-4. Circuit model of an inductively coupled power transfer system.

First, let's look at the transmitter. As the receiver draws power from the transmitting source, it "loads" the transmitter as an effective impedance $Z_{EQE(R)}$, as Figure 2-5 shows. The model in Figure 2-5 omits the resonant capacitor C_T and inductor L_R as they cancel out at f_O. Apply the Kirchhoff's voltage law (KVL) to the transmitter in Figure 2-4 gives:

$$v_S = i_T\left(R_S + R_T\right) + v_{E(T)}\,. \tag{2.14}$$

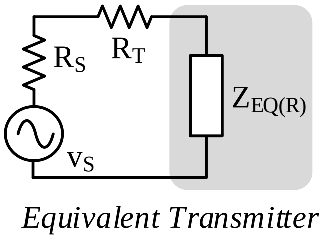

Figure 2-5. Equivalent transmitter model.

Replacing the $v_{E(T)}$ with Eq. (2.13) gives:

$$v_S = i_T\left(R_S + R_T\right) + M_C\frac{di_R}{dt}\,. \tag{2.15}$$

Since the system works on a single frequency f_O, converting the equation into phasor form simplifies the analysis:

$$V_S = I_T\left(R_S + R_T\right) + j\omega_O M_C I_R\,. \tag{2.16}$$

Again, from the receiver circuit in Figure 2-4, i_R can be expressed as:

$$I_R = \frac{v_{E(R)}}{R_R + Z_L} = \frac{j\omega_O M_C I_T}{R_R + Z_L}\,. \tag{2.17}$$

Replacing the I_R in Eq. (2.16) with Eq. (2.17) gives:

$$V_S = \left(R_S + R_T\right)I_T + \frac{\left(j\omega_O M_C\right)^2}{R_R + Z_L}I_T\,. \tag{2.18}$$

Therefore, the equivalent load from the receiver can be expressed as:

$$Z_{EQ(R)} = \frac{\left(j\omega_O M_C\right)^2}{R_R + Z_L}\,. \tag{2.19}$$

The transmitter's effect on the receiver is different. As the receiver draws power from the transmitter, it "loads" the transmitter and lowers i_T. As a result, the EMF voltage $v_{E(R)}$, coupled back on the receiver is lower. Therefore, the transmitter's impact on the receiver is like a source resistance to the coupled voltage source: higher i_R causes higher voltage drop from the induced open-circuit voltage v_E, so the closed-circuit $v_{E(R)}$ is lower. Figure 2-5 shows the equivalent decoupled model of the receiver circuit. The coupled resistance R_E models the transmitter's effect on the receiver.

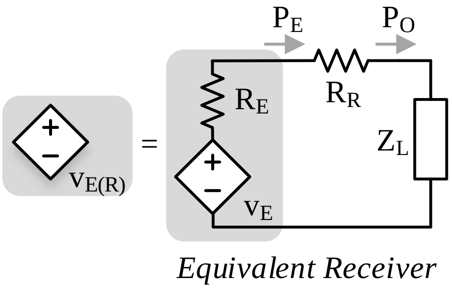

Figure 2-6. Equivalent receiver model.

One way to derive the open-circuit voltage v_E and equivalent R_E is to apply the KVL and KCL to the circuit in Figure 2-4. The coupled $v_{E(R)}$ can be expressed in phasor form as:

$$V_{E(R)} = j\omega_O M_C I_T . \tag{2.20}$$

The transmitting current i_T can be expressed as:

$$I_T = \frac{V_S - V_{E(T)}}{R_S + R_T} = \frac{V_S - j\omega_O M_C I_R}{R_S + R_T} . \tag{2.21}$$

Replacing the I_T in Eq. (2.20) with Eq. (2.21) yields:

$$V_{E(R)} = j\omega_O M_C \left(\frac{V_S - j\omega_O M_C I_R}{R_S + R_T} \right) = j\omega_O M_C \left(\frac{V_S}{R_S + R_T} \right) + \left(\frac{\omega_O{}^2 M_C{}^2}{R_S + R_T} \right) I_R . \tag{2.22}$$

Comparing Eq. (2.22) with

$$V_{E(R)} = V_E + R_E I_R \,. \tag{2.23}$$

gives the expressions for v_E and R_E:

$$V_E = j\omega_O M_C \left(\frac{V_S}{R_S + R_T} \right). \tag{2.24}$$

$$R_E = \frac{{\omega_O}^2 {M_C}^2}{R_S + R_T} \,. \tag{2.25}$$

The second way of derivation is more intuitive. When the receiver circuit is open-circuited, $v_{E(T)}$ is zero, so

$$V_E = j\omega_O M_C I_T \big|_{V_{E(T)}=0} = j\omega_O M_C \left(\frac{V_S}{R_S + R_T} \right). \tag{2.26}$$

The coupled voltage v_E and resistance R_E represent the power limit from the transmitter. So v_E and R_E should avail as much power as v_S and $R_S + R_T$:

$$\frac{\left(\frac{0.5V_S}{\sqrt{2}} \right)^2}{R_S + R_T} = \frac{\left(\frac{0.5V_E}{\sqrt{2}} \right)^2}{R_E} \,. \tag{2.27}$$

Therefore, combined with Eq. (2.26),

$$R_E = \frac{{V_E}^2}{{V_S}^2} \left(R_T + R_S \right) = \frac{{\omega_O}^2 {M_C}^2}{R_S + R_T} \,, \tag{2.28}$$

which yields the same result as Eq. (2.28).

The circuit models in Figure 2-5 and Figure 2-6 greatly simplify the analysis as they decouple the transmitter and the receiver. The next section of this chapter will show how the decoupled models can help predict the maximum power point (MPP) of the circuit.

2.3 Maximum Power Point

Power systems are often optimized for two goals, maximum efficiency point (MPE) and MPP. MPE is often designed to conserve energy and reduce heat dissipation. Since most embedded microsensors, as summarized in Table 1-1, consume only microwatts to milliwatts, energy conservation or heat dissipation is not among the top priorities. Rather, most embedded microsensors need maximum power to expand the functionality as well as improve power robustness. Therefore, most inductively coupled power transfer for embedded microsensors are designed for MPP instead of MPE.

In an inductively coupled power transfer system, Z_L in Figure 2-6 represents the power receiver. The key to drawing max power from L_R is that the receiver "load match" the source impedance [99]. The maximum power the receiver can draw is, therefore:

$$P_{O(MAX)} = \frac{\left(0.5v_{E(RMS)}\right)^2}{R_E + R_R} = \frac{\left(\frac{0.5v_{E(PK)}}{\sqrt{2}}\right)^2}{R_E + R_R} . \tag{2.29}$$

Radial distance d_R normalizes the power transmission distance with the transmitter and receiver's coil radius r_R and r_T:

$$d_R = \frac{d_X}{\sqrt{r_R r_T}} . \tag{2.30}$$

At $d_R << 1$, the coils are closely coupled. The receiver heavily loads the transmitter, so $R_E >> R_R$. The receiver circuit model reduces to that in Figure 2-7. In this case, the maximum receiver power can be expressed as:

$$P_{O(MAX)}\Big|_{R_E >> R_R} \approx \frac{\left(\frac{0.5v_{E(PK)}}{\sqrt{2}}\right)^2}{R_E}. \tag{2.31}$$

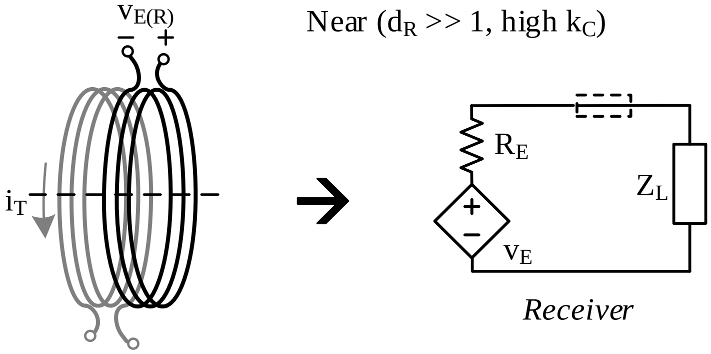

Figure 2-7. Equivalent receiver circuit when closely coupled.

Combined with Eq. (2.27), the maximum receiver power can be rewritten as:

$$P_{O(MAX)}\Big|_{R_E >> R_R} \approx \frac{\left(\frac{0.5v_{S(PK)}}{\sqrt{2}}\right)^2}{R_S + R_T} \neq f(d_X), \tag{2.32}$$

which does not scale with distance d_X. Another explanation for (2.32) is that, when the coils are closely coupled, maximum receiver power is limited by the maximum transmitter power, which yields the same result:

$$P_{O(MAX)}\Big|_{R_E >> R_R} \approx P_{E(MAX)} = \frac{\left(\frac{0.5v_{S(PK)}}{\sqrt{2}}\right)^2}{R_S + R_T}. \tag{2.33}$$

However, when the radial distance $d_R >> 1$, the coils are loosely coupled. The receiver barely loads the transmitter, so $R_E << R_R$. The equivalent receiver circuit reduces to the circuit in Figure 2-8. In this case, the maximum power the receiver can draw is limited by the coupled voltage v_E. As v_E drops cubically with d_X, $P_{O(MAX)}$ drops even faster with $d_X{}^6$:

$$P_{O(MAX)}\Big|_{R_E >> R_R} \approx \frac{\left(\frac{0.5v_{E(PK)}}{\sqrt{2}}\right)^2}{R_R} \propto \frac{1}{d_X{}^6}. \tag{2.34}$$

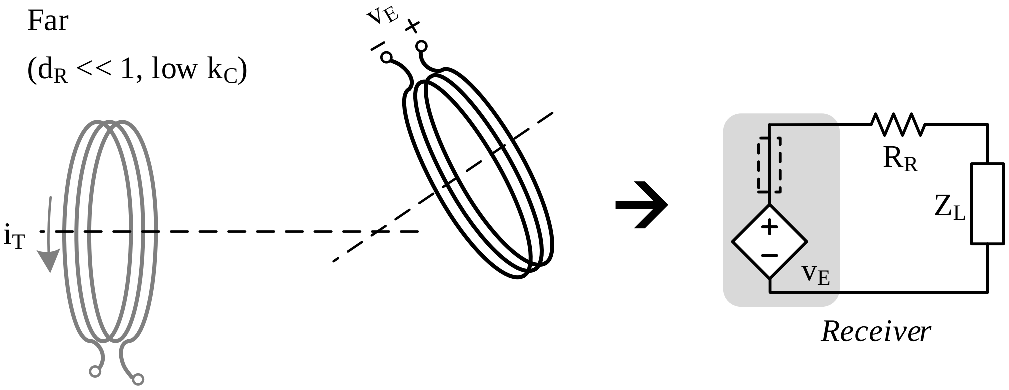

Figure 2-8. Equivalent receiver circuit when loosely coupled.

The $P_{O(MAX)}$ expression in Eq. (2.29) is intuitive. However, the $P_{O(MAX)}$'s variable dependence is not clear in this equation, as v_E, R_E, and R_R depend on many variables such as k_C, L_T, L_R, f_O, R_T, etc. The quality factor Q represents one or a group of components' reactive/resistive impedance ratio. For the transmitting and receiving loop:

$$Q_T = \frac{\omega_O L_T}{R_T + R_S}, \tag{2.35}$$

$$Q_R = \frac{\omega_O L_R}{R_R}, \tag{2.36}$$

Combining Eq. (2.26), Eq. (2.28), Eq. (2.35), and Eq. (2.36), $P_{O(MAX)}$ can be rewritten as:

$$P_{O(MAX)} = \frac{\left(\frac{0.5v_{E(PK)}}{\sqrt{2}}\right)^2}{R_E + R_R} = \frac{\left(j\omega_O M_C\right)^2 \left(\frac{v_{S(PK)}}{\frac{\omega_O L_T}{Q_T}}\right)^2}{8\left[\left(\frac{\omega_O{}^2 M_C{}^2}{\frac{\omega_O L_T}{Q_T}}\right) + \left(\frac{\omega_O L_R}{Q_R}\right)\right]}. \tag{2.37}$$

Replacing the M_C in Eq. (2.37) with Eq. (2.11), $P_{O(MAX)}$'s expression can be simplified as:

$$P_{O(MAX)} = \left(\frac{k_C{}^2 Q_T Q_R}{1 + k_C{}^2 Q_T Q_R}\right)\left[\frac{v_{S(PK)}}{2\sqrt{2}\left(R_S + R_T\right)}\right]^2 = \left(\frac{k_C{}^2 Q_T Q_R}{1 + k_C{}^2 Q_T Q_R}\right) P_{E(MAX)}. \tag{2.38}$$

From Eq. (2.38), it is clear that $P_{O(MAX)}$ depends on the available power of the transmitter, k_C, Q_T and Q_R. When $k_C >> \frac{1}{Q_T Q_R}$, $P_{O(MAX)}$ does not scale with k_C:

$$P_{O(MAX)} \approx P_{E(MAX)}. \tag{2.39}$$

When $k_C << \frac{1}{Q_T Q_R}$, $P_{O(MAX)}$ drops quadratically with k_C:

$$P_{O(MAX)} \approx k_C{}^2 Q_T Q_R P_{E(MAX)}. \tag{2.40}$$

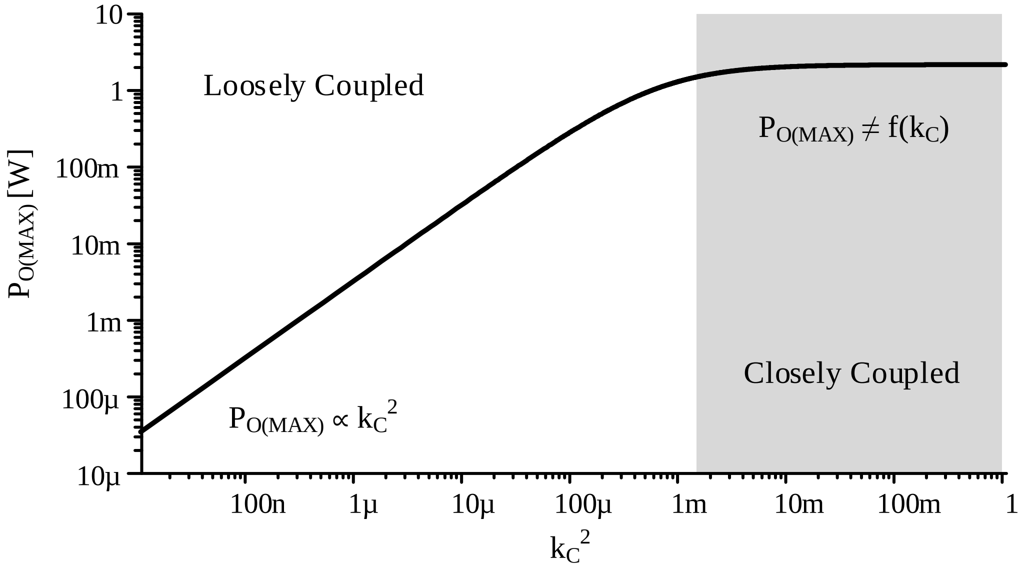

Figure 2-9. Maximum receiver power as a function of k_C^2.

The alternative expression of $P_{O(MAX)}$ in Eq. (2.38) also provides a more quantitative definition for closely/loosely coupled: the coils are loosely coupled when $k_C >> \frac{1}{Q_T Q_R}$, and loosely coupled when $k_C << \frac{1}{Q_T Q_R}$. Figure 2-9 plots the maximum receiver power as a function of k_C^2. In the closely coupled the region, $P_{O(MAX)}$ curve stays flat, as it is capped by the transmitting source. In the loosely coupled region, $P_{O(MAX)}$ drops 10 dB/dec, as it drops quadratically with k_C.

2.4 MPP Power Receiver

2.4.1 Ideality Index

The previous section of the chapter derives the maximum receiver power $P_{O(MAX)}$. However, the derived $P_{O(MAX)}$ is only a theoretical maximum. The maximum power any real receiver can output at MPP ($P_{O(MPP)}$) is always lower than $P_{O(MAX)}$ for several reasons. First, drawing the highest $P_{O(MPP)}$ requires the receiver to "load match" the v_E's source resistance $R_E + R_R$. However, the receiver is not a resistor. The receiver needs to rectify the inductor current to charge up the energy storage. So the receiver is not a linear component. Second, the analysis in the previous section considers only conduction losses, whereas real receivers suffer from charge loss, quiescent loss and other losses as well. Finally, the receiver also has conduction loss, so the output power to the battery is always lower than $P_{O(MAX)}$.

However, the theoretical maximum receiver power $P_{O(MAX)}$ provides a good reference point for receiver design. The maximum output power $P_{O(MPP)}$ is the key performance of the wireless power receiver. However, different wireless receivers' $P_{O(MPP)}$ is not comparable, as $P_{O(MPP)}$ scales with the transmitter's power and coupling. To assess the relative performance of the wireless charger, $P_{O(MPP)}$ needs to be normalized. The ideality factor η_I references $P_{O(MPP)}$ to $P_{O(MAX)}$ and normalizes $P_{O(MPP)}$ with non-receiver variables:

$$\eta_I = \frac{P_{O(MPP)}}{P_{O(MAX)}}. \tag{2.41}$$

2.4.2 Boosting Drawn Power

The maximum power point theory in the previous section concludes that to deliver the highest power, the receiver must "load match" v_E's source impedance. That means the receiver's resistive impedance needs to match $R_E + R_R$, and its reactive impedance needs to cancel $\left(jL_T\omega_O\right)$. However, this guideline is impractical for receiver design, as the power receiver is not a passive element, but an active, nonlinear, switched circuit that rectifies the inductor current to charge up the energy storage. The rest of this section discusses how to operate the receiver so it mimics the effect of a matched passive load.

Figure 2-10 shows the power model of an inductively coupled power system. The voltage of across the power receiver is v_R. To understand how v_E in Figure 2-10 generates power, first consider shorting the power receiver so $v_R = 0$. This way, v_E's sinusoid across L_R produces a current $i_{L(0)}$ in that is 90° out of phase. This is because v_E's positive half-cycles raise i_L and v_E's negative half-cycles reduce i_L about a 0-mA median. v_E and $i_{L(0)}$ are therefore both positive and both negative half the time and opposite polarities the other half. This means, v_E outputs as much power as it consumes, so output power is nil.

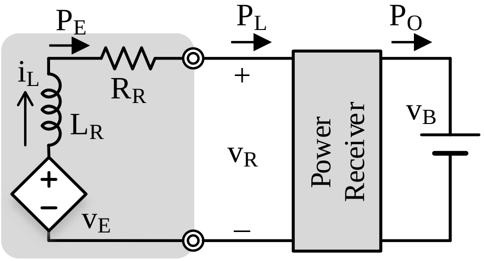

Figure 2-10. Power model of the inductively coupled power system.

The only way to net output power is to reduce the phase difference between v_E and i_L . Luckily, applying a receiver voltage v_R at the beginning of v_E's positive half-cycle like Figure 2-11 shows at 0 µs energizes L_R quicker to a higher peak i_L so that applying a negative voltage after that can help reduce i_L to zero at the end of the half-cycle. Similarly, applying a negative v_R when the negative half-cycle begins at 0.5 µs energizes L_R to a lower peak i_L so that impressing a positive voltage after that can help raise i_L to zero at the end of the half-cycle. When balanced this way, v_E and i_L are in phase (with the same polarity), so v_E only *sources* power.

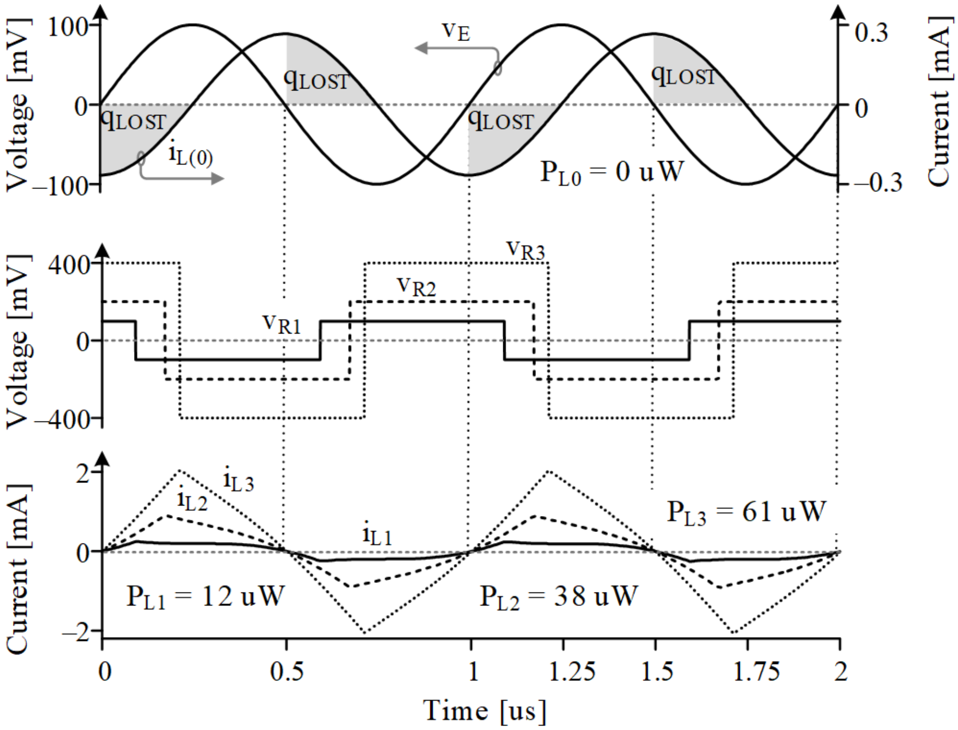

Figure 2-11. Simulated waveforms with and without receiver voltage v_R.

If the system is lossless, v_R recovers the power that v_E delivers with i_L. In other words, v_{ER} ultimately receives what v_E produces. And since a higher v_R raises i_L to an even higher peak, higher v_R's can draw more power from v_E. This is why v_{R1}'s 100 mV, v_{R2}'s 200 mV, and v_{R3}'s 400 mW in Figure 2-11 draw 12, 38, and 61 µW, respectively. Applying high alternating high voltage v_R across L_R boosts P_E.

2.4.3 Maximizing Receiver Power

Although P_E in Figure 2-10 grows indefinitely with higher v_R, in reality, L_R's ESR R_R limits how much power the L_R can output (P_L). This is because, as i_L continues to rise, the quadratically growing conduction loss on R_R (P_R) eventually outgrows the power drawn from v_E. As shows, before v_R reaches v_{MPP0}, P_O grows with v_R as higher voltage boosts damping force. Past v_{MPP0}, P_O drops as the conduction loss negates the drawn power gain, as Figure 2-12 shows. L_R's output power maximizes at v_{MPP0} when the receiver's damping force balances the drawn power gain and the conduction loss. The receiver's breakdown voltage also limits how much v_R can be applied and, thus, L_R's output power. So, the coil's output power is both loss- and breakdown-limited.

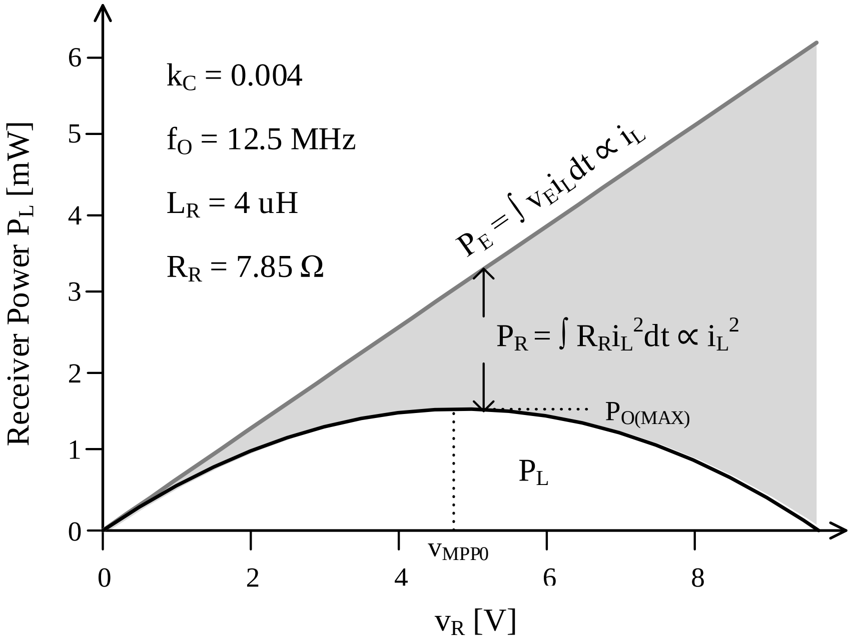

Figure 2-12. Simulated receiver power as a function of v_R.

To sum up, to maximize the receiver power P_L, the receiver must impress an alternating voltage v_R across the receiver coil L_R. Besides, the impressed voltage v_R's magnitude must be right at its optimal value. This way, the receiver mimics the effect of a matched passive load and the receiver power P_L is close to $P_{O(MAX)}$.

2.5 Research Objective

Therefore, the objective of this research is to evaluate, design, build, test, and assess an inductively coupled CMOS power receiver for embedded microsensors with the highest ideality index η_I possible. Or in other words, the receiver's output power at MPP ($P_{O(MPP)}$)

should be as close to its theoretical maximum $P_{O(MAX)}$ as possible. Achieving high η_I is challenging. First, coupling in these applications is very weak because the separation between the transmitter and receiver coils far exceeds the radius of the coils. Such a tiny, weakly coupled, and often misaligned receiver coil only couples millivolts, so drawing power is difficult. Applying a high voltage boosts coil current and, in consequence, outputs more power, but only to the extent that the circuit's breakdown voltage allows. Plus, tiny coils are so resistive that ohmic losses also constrain output power. This research, therefore, proposes to study how breakdown voltage and losses limit output power, and under those conditions, how a receiver can output the highest power possible. With this understanding, the research will then explore and develop a low-loss CMOS power receiver with a microwatt controller that can operate the system so output power is maximally high. The ultimate goal is to build a power-receiver system that can draw and output more power than the state of the art, and that way, expand the functionality, life, and application space of emerging biomedical implants and structurally embedded microsensors.

To achieve this objective, the first step is to assess and identify the best receiver power stage that outputs the highest power with the least breakdown limit and fewest components. For this, Chapter 3 reviews and assesses the state-of-the-art power receivers in terms of their power, breakdown limitation, and compactness. Chapter 4 proposes a switched resonant half-bridge power receiver that outputs up to 85% of $P_{O(MAX)}$ without breakdown constraint. After identifying the best power stage, the second step is to develop a theory that predicts the best settings at which the receiver can output the highest $P_{O(MPP)}$. For this, Chapter 5 proposed an MPP theory that is 98.75% accurate in predicting the MPP settings. The final step is to address the practical challenges in the controller design. For this, Chapter 6 presents a microwatt controller that synchronizes the operation of the proposed switched resonant half-bridge.

CHAPTER 3. THE STATE OF THE ART IN POWER RECEIVERS

The state-of-the-art inductively coupled power receivers can be categorized into four types: resonant power receiver, multiplying charge pump, switched bridge, and switched resonant bridge. This chapter discusses and compares the four types of power receivers in terms of their operations, compactness, loss-limited maximum output power, breakdown limitations, and other limitations.

3.1 Resonant Bridge

3.1.1 Resonant Full-bridge

A. Operation

The basic concept of a resonant power receiver is to use the LC oscillation voltage as the alternating high voltage v_R across the receiver coil to maximizes the receiver power $P_{L(MAX)}$. The resonant full-bridge [10, 12, 34, 82, 83, 100-104] in Figure 3-1 is composed of an LC resonant tank (L_R, C_R) and a full-bridge circuit. L_R and C_R are tuned to resonate at the transmitter frequency f_O. This way, the inductor current i_L is always in-phase with the coupled voltage v_E. As a result, during the startup, v_E constantly sources power into L_R–C_R, and the oscillation voltage v_C grows from cycle to cycle.

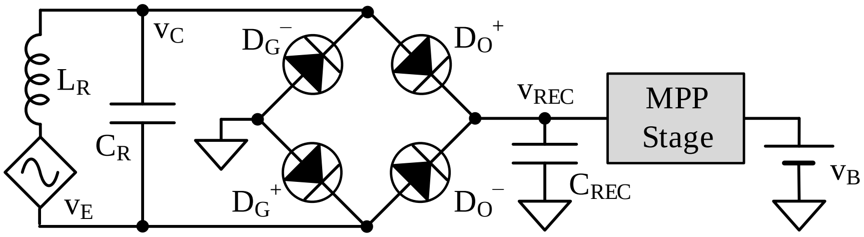

Figure 3-1. The resonant full-bridge power receiver.

Once v_C grows beyond the rectified voltage v_{REC}, diodes D_O^+ and D_G^+ conduct and clamp v_C to v_{REC} for t_{REC}^+, as the waveform in Figure 3-2 shows. During the clamped time, the inductor current i_L is redirected by D_O^+ and D_G^+ to charge the rectified capacitor C_{REC}. So the energy in the LC tank is transferred to C_{REC}. Similarly, as v_C drops below $-v_{REC}$, diodes D_O^- and D_G^- conduct to clamp v_C at $-v_{REC}$ and charge C_{REC} in the opposite direction. As discussed in the previous chapter, to maximize $P_{O(MAX)}$, the voltage across L_R (v_C in the resonant full-bridge) needs to be regulated at its optimal level. For this purpose, an MPP stage adjusts the v_{REC} so v_C is clamped at the optimal level.

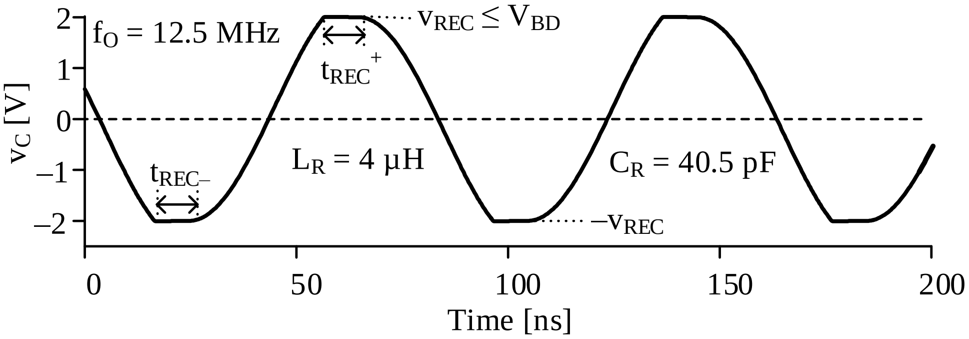

Figure 3-2. Waveform of the resonant full-bridge.

B. Power

Since v_E in far applications is often dwarfed v_C, the energy that LC tank takes (from v_E) and gives (to C_{REC}) every cycle is a negligible part of the energy being exchanged between L_R and C_R. So, L_R's peak energy $E_{L(PK)}$ approximately matches C_R's peak energy $E_{C(PK)}$:

$$E_{L(PK)} = 0.5 i_{L(PK)}{}^2 L_R \approx E_{C(PK)} = 0.5 v_{C(PK)}{}^2 = 0.5 v_{REC}{}^2 C_R\,. \tag{3.1}$$

Equation (3.1) relates $i_{L(PK)}$ and v_{REC} as:

$$i_{L(PK)} \approx v_{REC}\sqrt{\frac{C_R}{L_R}}\,. \tag{3.2}$$

When the coupled voltage v_E is low, the clamped time $t_{REC}{}^+$ and $t_{REC}{}^-$. As a result, the v_C and i_L waveforms can be approximated as sinusoidal waveforms. With the in-phase i_L and $v_{E(R)}$, The power v_E sources can be calculated by integrating the voltage and current over a cycle T_O:

$$\begin{aligned} P_E &= \int_0^{T_O} v_E i_L dt \\ &= \int_0^{T_O} v_{E(PK)} \sin(2\pi f_O t)\, i_{L(PK)} \sin(2\pi f_O t)\, dt\,. \\ &= 0.5 v_{E(PK)} i_{L(PK)} \end{aligned} \tag{3.3}$$

Replacing the $i_{L(PK)}$ in Eq. (3.3) with Eq. (3.2), P_E can be rewritten as:

$$P_E = 0.5 v_{E(PK)} v_{REC}\sqrt{\frac{C_R}{L_R}}\,. \tag{3.4}$$

The sourced power P_E loses to the conduction loss of L_R's ESR:

$$\begin{aligned} P_R &= \int_0^{T_O} i_L{}^2 R_R dt \\ &= \int_0^{T_O} i_{L(PK)}{}^2 \sin^2(2\pi f_O t) R_R dt\,. \\ &= 0.5 R_R i_{L(PK)}{}^2 \end{aligned} \tag{3.5}$$

Replacing the $i_{L(PK)}$ in Eq. (3.5) with Eq. (3.2), P_R can be rewritten as:

$$P_R = 0.5 R_R v_{REC}^{\,2}\left(\frac{C_R}{L_R}\right). \tag{3.6}$$

The receiver power P_L is the difference between P_E and P_R:

$$\begin{aligned} P_L &= P_E - P_R \\ &= 0.5 v_{E(PK)} v_{REC}\sqrt{\frac{C_R}{L_R}} - 0.5\left(R_R + R_E\right) v_{REC}^{\,2}\left(\frac{C_R}{L_R}\right) \\ &= -0.5 R_R\left(\frac{C_R}{L_R}\right)\left[v_{REC} - \left(\frac{0.5 v_{E(PK)}}{R_R + R_E}\right)\sqrt{\frac{L_R}{C_R}}\right]^2 + \frac{v_{E(PK)}^{\,2}}{8\left(R_R + R_E\right)} \end{aligned}. \tag{3.7}$$

P_L is a parabolic function of v_{REC}, so:

$$P_{L(MAX)} = \frac{v_{E(PK)}^{\,2}}{8\left(R_R + R_E\right)}, \tag{3.8}$$

when

$$v_{REC(OPT)} = \left(\frac{0.5 v_{E(PK)}}{R_R + R_E}\right)\sqrt{\frac{L_R}{C_R}}. \tag{3.9}$$

Since L_R and C_R resonate at f_O:

$$f_O = \frac{1}{2\pi\sqrt{L_R C_R}}. \tag{3.10}$$

Replacing the C_R in (3.9) with (3.10), $v_{REC(OPT)}$ can be rewritten as:

$$v_{REC(OPT)} = \left(\frac{v_{E(PK)}}{2}\right)\left(\frac{2\pi f_O L_R}{R_R}\right) = 0.5 Q_R v_{E(PK)}. \tag{3.11}$$

The resonant full-bridge's maximum receiver power $P_{L(MAX)}$ is the same as the theoretical maximum receiver power derived in Eq. (2.37). This is based on the approximation that i_L and v_C's waveforms are sinusoidal. When the coupling is higher, the clamped time t_{REC}^+ and t_{REC}^- become a significant portion of the period T_O, so $P_{O(MAX)}$ is slightly less than the theory's prediction.

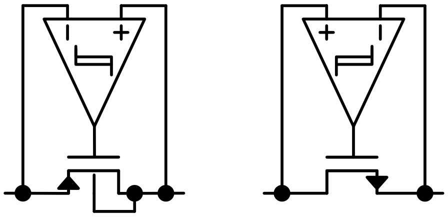

Figure 3-3. Comparator based PMOS and NMOS switches.

For low-voltage and low-power power receivers, the voltage drop on the diodes in the resonant full-bridge causes significant conduction loss. The diodes are often implemented as a comparator based MOSFET switch, as shown in Figure 3-3 to reduce the voltage drop to millivolts [82-84, 105-108]. The ground diodes or the output diodes can be replaced with a pair of gate cross-coupled transistors to save area and power [84, 105, 106, 109], like Figure 3-4 shows. As v_C swings above v_{REC}, the gate voltage of M_G^+ is high, so M_G^+ turns on. Similarly, as v_C swings below $-v_{REC}$, the gate voltage of M_G^- is high, so M_G^- turns on. So M_G^+ and M_G^- turn on and off the same way as D_G^+ and D_G^- in Figure 3-1.

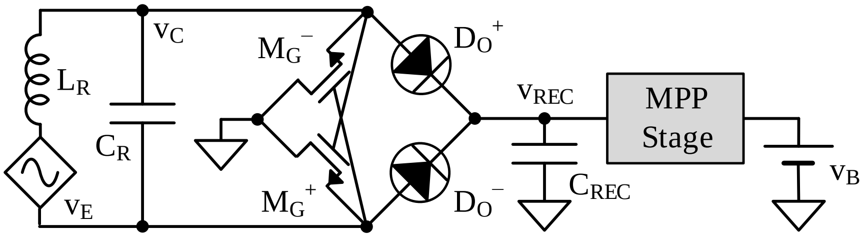

Figure 3-4. Resonant full-bridge with cross-coupled NMOS pair.

C. Limits

For max power, the MPP buffer in Figure 3-1 needs to regulate v_{REC} at $0.5Q_Rv_{E(PK)}$. However, as $v_{E(PK)}$ gets higher, $0.5Q_Rv_{E(PK)}$ may exceed the CMOS circuit's breakdown V_{BD}. Since all D_O^+ and D_O^- both see v_{REC}, the MPP buffer can no longer regulate v_{REC} to its optimal value but to V_{BD}. In other words, the maximum voltage across the L_R (v_C in this case) is limited to V_{BD}.

3.1.2 Resonant Half-bridge

A. Operation

C_R in the resonant half-bridge of Figure 3-5 similarly produces a voltage v_C that keeps i_L and v_E in-phase. The induced v_E, as a result, constantly sources power to the LC tank and boosts the oscillation. As v_C oscillates beyond v_{REC}, millivolts diode D_{REC} conducts to steer i_L to charge up C_{REC}.

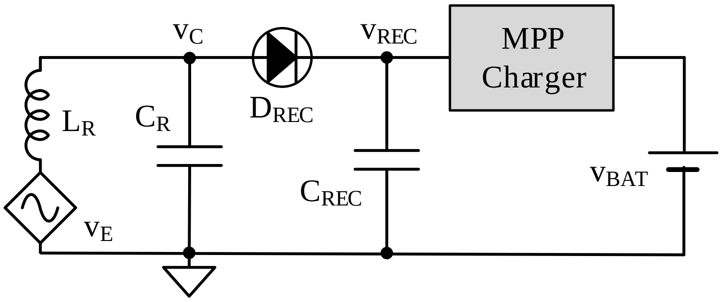

Figure 3-5. Resonant half-bridge power receiver.

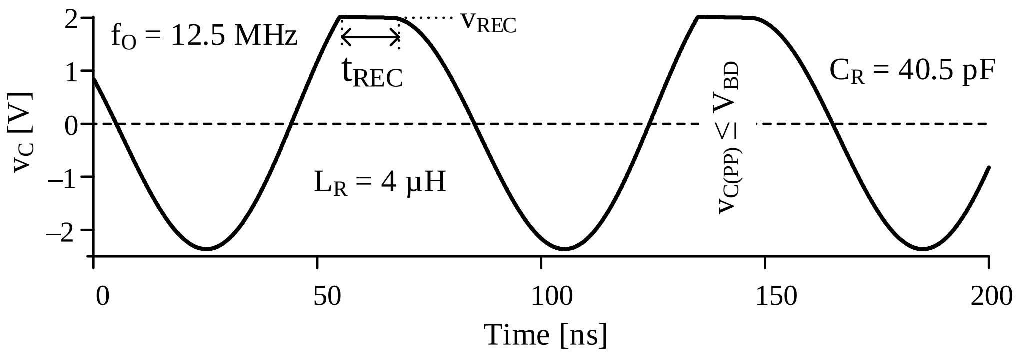

Figure 3-6. Waveform of the resonant half-bridge.

B. Power

Compared to the resonant full-bridge, the resonant half-bridge's v_C is not clamped above zero, as Figure 3-6 shows. However, for most embedded microsensor applications, the coupled voltage v_E is low in millivolts. As a result, the energy v_E sourced to LC tank each cycle is much smaller than the energy being exchanged between L_R and C_R. So the negative $v_{C(PK)}$ is close to $-v_{REC}$. Similarly, the v_C and i_L waveforms can be approximated as sinusoidal waveforms. The P_E calculation for the resonant full-bridge in (3.3) and (3.4) is still valid for the resonant half-bridge. For the same reason, the conduction loss P_R calculation is the same as the resonant full-bridge as well. As both resonant full-bridge and resonant half draw the same P_E from v_E, and lose the same P_R on R_R and R_E, their maximum receiver power $P_{O(MAX)}$ is about the same. This may sound counter-intuitive at first glance, as the resonant full-bridge draws power twice in a cycle, which is twice as frequent as the resonant half-bridge. However, each time the half-bridge transfers energy accumulated in a full cycle, while the full-bridge only transfers energy accumulated in a half-cycle. As a result, their $P_{O(MAX)}$ is about the same.

C. Limits

Compared to the resonant full-bridge, the resonant half-bridge uses only one switche D_{REC} and is thus more compact. However, this simplification also brings two disadvantages. First, as the waveform in Figure 3-6 shows, as there is no ground diode that clamps v_C at the ground, v_C can swing below zero. As D_{REC} sees the negative swing of v_C, the circuit requires a negative supply to bias the body of the FETs to prevent the body diode from turning on. This adds area and complexity to the circuitry. Second, since D_{REC} sees v_C's full swing, the maximum voltage across L_R is limited to half of the V_{BD}. This means the breakdown limit is only half as high as the resonant full-bridge. Similar to the resonant full-bridge, the damping voltage across L_R is v_C. For MPP, an extra MPP buffer stage is required to regulate v_{REC} at its optimal value.

3.2 Multiplying Charge Pump

The multiplying charge pump [7, 17, 88, 94, 105, 110-114] in Figure 3-7 uses capacitors to transfer energy. A multiplying charge pump consists of one or more stages. Similar to the resonant bridge and the resonant half-bridge, the multiplying charge pump uses a resonant capacitor C_R to generate oscillation. During the negative half-cycle of the oscillation voltage v_C, D_{G1}^- of Figure 3-7 turns on to charge C_{C1}^+ to $v_{C(PK)}$. For the next half-cycle, the positive v_C stacks on top of C_{C1}^+. tIdeally, each stage raises the output voltage by $2v_{C(PK)}$. In reality, the parasitic capacitance and output loads the circuit and brings v_{ON} down:

$$v_{ON} = 2N\left(\frac{C_O}{C_O + C_{PAR}} v_{C(PK)} - \frac{I_O}{f_O\left(C_O + C_P\right)}\right). \tag{3.12}$$

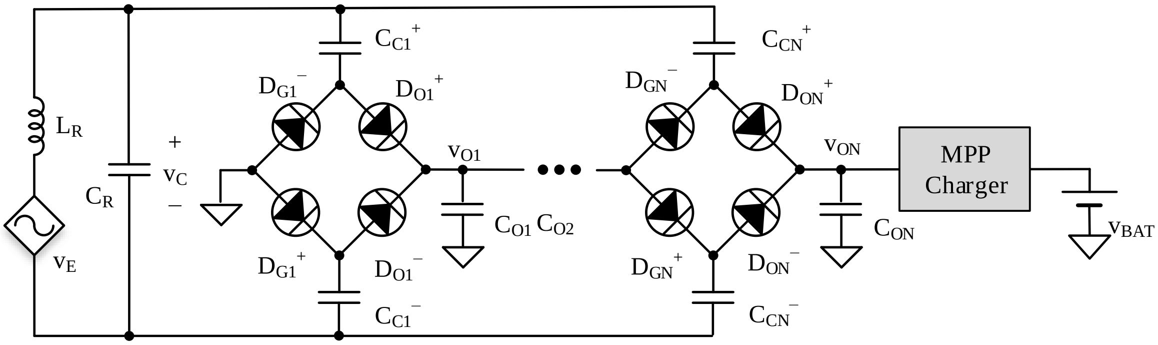

Figure 3-7. Multiplying charge pump.

L_R's conduction loss limits the multiplying charge pump as much as it limits the resonant bridge or the resonant half-bridge. So L_R can output as much as power as the resonant power receivers when loss-limited. However, the power L_R outputs dissipates as heat as current flows through the diodes, so the power that reaches v_{ON} is lower. Although replacing the bridge circuit with a fully cross-coupled bridge reduces the diode loss, it increases the loss due to reverse current [91]. Moreover, the multiplying charge pump is also more breakdown-limited than the resonant power receivers. As v_{ON} amplifies $v_{C(PK)}$, the damping voltage v_C is limited to a fraction of v_{BD}. Finally, an N-stage charge pump requires 3N+1 capacitors and 4N switches, costing more silicon real estate.

3.3 Switched Bridge

3.3.1 Non-Investing Switched Bridge

A. Operation

The switched bridge does not use resonance to provide the damping voltage. Instead, the bridge circuit in Figure 3-8 connects L_R to the battery periodically to provide the damping voltage v_R. Figure 3-9 shows the waveforms of the non-investing switched bridge. Starting at zero i_L (at ~20 ns), since both switches S_G^+ and S_G^- close, the voltage across L_R is v_E. So the positive v_E energizes i_L in the positive direction till v_E's polarity flips. Then the ground switch S_G^- opens, the energy built up in L_R is transferred to the battery v_B through D_O^+. For the next half-cycle, the negative v_E, energizes i_L in the opposite direction till v_E's polarity flips again. Then the ground switch S_G^+ opens, the energy built up in L_R is transferred to the battery v_B through D_O^-.

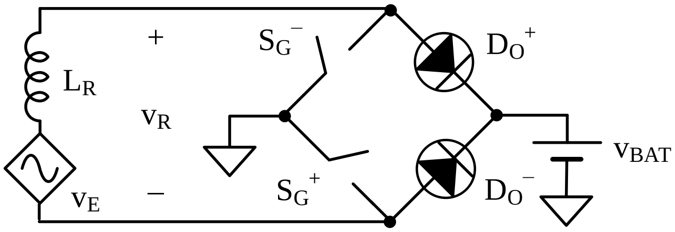

Figure 3-8. Non-investing switched bridge.

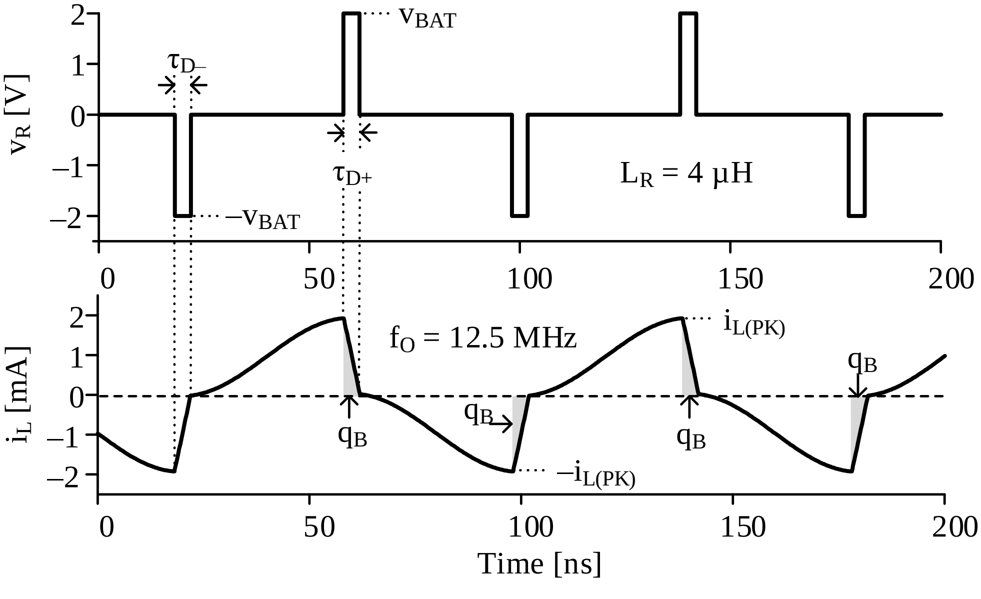

Figure 3-9. Waveforms of the non-investing switched bridge.

B. Power & Limits

As v_B is often much higher than the induced voltage v_E, the energy transfer time $\tau_D^+(\tau_D^-)$ is a negligible portion of the cycle. So the peak inductor current $i_{L(PK)}$ can be derived from the voltage across L_R over half-cycle:

$$i_{L(PK)} = \int_0^{0.5T_O} \frac{v_E}{L_R} dt = \int_0^{0.5T_O} \frac{v_{E(PK)} \sin\left(2\pi f_O t\right)}{L_R} dt = \frac{v_{E(PK)}}{\pi f_O L_R} = \frac{v_{E(PK)}}{0.5Q_R R_R}. \qquad (3.13)$$

During one half-cycle, L_R transfers all its energy to the battery:

$$E_{L(PK)} = 0.5L_R i_{L(PK)}{}^2 = \frac{v_{E(PK)}{}^2}{2\pi^2 f_O{}^2 L_R}. \qquad (3.14)$$

So the receiver power P_L is $E_{L(PK)}$ averaged over half-cycle:

$$P_L = \frac{E_{L(PK)}}{0.5T_O} = \frac{v_{E(PK)}{}^2}{\pi^2 f_O L_R} = \frac{2v_{E(PK)}{}^2}{\pi Q_R R_R}. \qquad (3.15)$$

The receiver power P_L of the non-investing switched bridge is not a function of battery voltage. The non-investing switched bridge's P_L is only a $16/\pi Q_R(<<1)$ fraction of that of a resonant half/full-bridge. This is because, although the voltage across L_R v_R can be as high as v_B, its duration is short. As a result, the averaged v_R magnitude is low. With v_B, the time $\tau_D{}^{+/-}$ to full drain L_R's energy is:

$$\tau_D \approx \frac{i_{L(PK)}}{\left(\frac{v_B}{L_R}\right)} = \frac{v_{E(PK)}}{\pi f_O v_B}. \qquad (3.16)$$

The averaged v_R magnitude is:

$$\left|v_R\right|_{(AVG)} = v_B\left(\frac{\tau_D}{0.5T_O}\right) = \frac{2v_{E(PK)}}{\pi}. \qquad (3.17)$$

The average v_R magnitude in the non-investing switched bridge is much lower than the optimal v_R for MPP ($0.5Q_R v_{E(PK)}$). As a result, the receiver power P_L is very low.

Although the non-investing switched bridge does not require an MPP buffer stage, it requires a synchronizer circuit to turn off S_G^- and S_G^+ when i_L peaks.

3.3.2 *Investing Switched Bridge*

A. Operation

The non-investing switched bridge in Figure 3-10 outputs little power as the duty cycle of the battery connection is very small. The investing switched bridge [115, 116] replaces the output diodes with switches S_O^+ and S_O^-, as shown in Figure 3-10, so L_R can connect to C_{REC} when i_L flows in both directions.

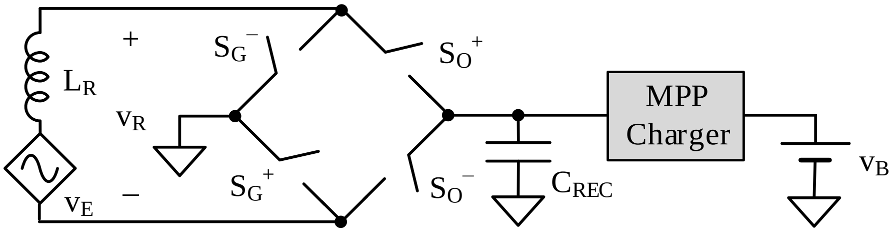

Figure 3-10. The investing switched bridge power receiver.

Figure 3-11 shows the waveforms of the investing switched bridge. During v_E's rising half-cycle, S_G^- and S_O^- close so v_{REC} ramps up i_L linearly to its peak $i_{L(PK)}$. During v_E's falling half-cycle, S_G^+ and S_O^+ close, so i_L ramps down linearly with v_E. Since v_E is small compared to v_{REC}, i_L's waveform is almost triangular.

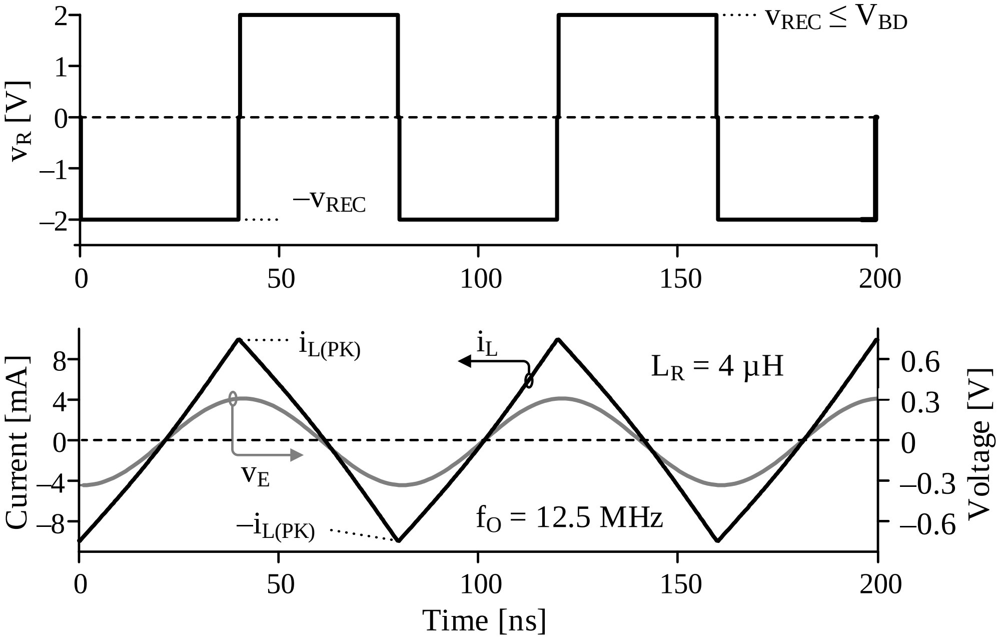

Figure 3-11. Waveforms of the investing switched bridge.

B. Power

The power sourced from P_E can be calculated by integrated v_E and i_L over the positive v_E half-cycle, as the negative half-cycle's power is the same:

$$\begin{aligned} P_E &= \int_0^{0.5T_O} v_E i_L dt \\ &= \int_0^{0.5T_O} v_{E(PK)} \sin\left(2\pi f_O t\right)\left(\frac{v_{REC}}{L_R}\right) t dt \cdot \\ &= \frac{v_{E(PK)} v_{REC}}{\pi^2 f_O L_R} \end{aligned} \qquad (3.18)$$

Compared to the resonant power receivers, the investing switched bridge's v_E sources 27% more power. This is because, while the resonant bridge's damping voltage is sinusoidal with peak limited to v_{REC}, the investing switched bridge connects L_R to v_{REC} or $-v_{REC}$ all the time. So the averaged damping voltage and $i_{L(PK)}$ are higher. Higher $i_{L(PK)}$, however, also increases L_R's conduction loss:

$$
\begin{aligned}
P_R &= \int_0^{0.5T_O} \left(R_R + R_E\right) i_L{}^2 dt \\
&= \int_0^{0.5T_O} \left(R_R + R_E\right) \left(\frac{v_{REC}}{L_R}\right)^2 t^2 dt \cdot \\
&= R_R \left[\left(\frac{v_{REC}}{L_R}\right)\left(\frac{0.25T_O}{\sqrt{3}}\right)\right]^2
\end{aligned}
\tag{3.19}
$$

The receiver power P_L is the difference between P_E and P_R:

$$
P_L = P_E - P_R = \frac{v_{E(PK)} v_{REC}}{\pi^2 f_O L_R} - R_R \left[\left(\frac{v_{REC}}{L_R}\right)\left(\frac{0.25T_O}{\sqrt{3}}\right)\right]^2, \tag{3.20}
$$

which, similar to the resonant half/full-bridge, is a parabolic curve of v_{REC}. So

$$
P_{L(MAX)}\Big|_{v_{REC}=0.387Q_R v_{E(PK)}} = \frac{12 v_{E(PK)}{}^2}{\pi^4 R_R}. \tag{3.21}
$$

Combining the higher P_E and higher P_R, the maximum receiver power from L_R is only 1.5% lower than the theoretical maximum $P_{O(MAX)}$ obtained in (2.29). The investing switched bridge also reaches MPP at a lower v_{REC} of $0.387Q_R v_{E(PK)}$. However, since all 4 switches, $S_G{}^+$, $S_G{}^-$, $S_O{}^+$, and $S_O{}^-$ see v_{REC}, the maximum v_{REC} that can be applied across L_R is limited to V_{BD}.

C. Limits

For MPP, the investing switched bridge also requires an MPP buffer stage to regulate the rectified voltage v_{REC} so it is at is optimal level. However, the MPP buffer is necessary only when the battery voltage v_B is lower than the optimal v_{REC}. When v_B is higher than $0.387Q_R v_{E(PK)}$, the investing switched bridge can adjust L_R's battery connection duty cycle to reduce the average voltage across L_R. The investing switched bridge also requires a synchronizer to turn on and turn off the switches when v_E peaks and valleys.

3.4 Switched Resonant Bridge

3.4.1 Serially Drained Scheme

A. Operation

The switched resonant bridge in Figure 3-12 [117-122], like the resonant bridge, uses C_R to keep v_E and i_L in-phase. However, unlike the resonant bridge, the circuit drains LC tank's energy to v_B in series. C_R and L_R, when tuned to resonate at f_O, exchange and receive power from v_E. As a result, $v_{C(PK)}$ grows from cycle to cycle until it reaches MPP. S_R then opens for t_{ON}, like Figure 3-13 shows. The bridge connects the LC in series with v_B and drains a portion of LC tank's energy to charge up v_B. By controlling t_B, the bridge circuit drains just enough energy so that $v_{C(PK)}$ remains at it maximum power point next cycle.

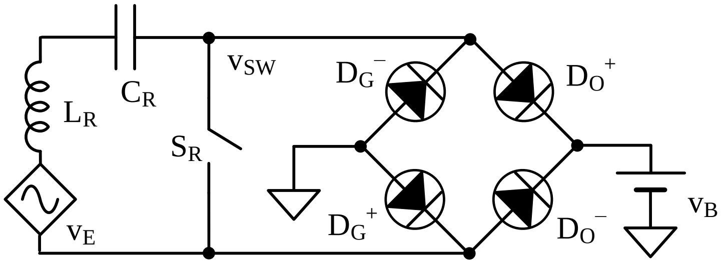

Figure 3-12. Serially drained switched resonant bridge power receiver.

Although the switched resonant bridge can transfer to v_B every cycle, it does not have to. Transferring energy less frequently [122-124] can reduce the switching and gate drive loss. Figure 3-14 shows a switched resonant bridge that transfers energy every 5 cycles. As switched resonant bridge skips energy transfer in the first 4 cycles, energy builts in the LC tank. On the 5th cycle, the bridge transfers the accumulated energy to v_B.

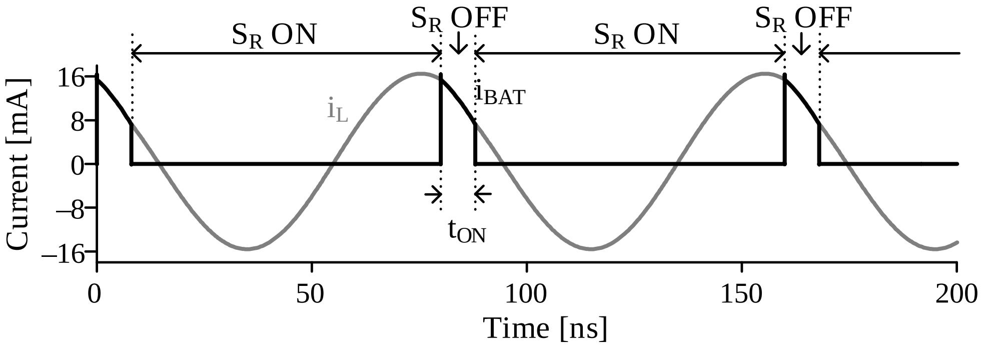

Figure 3-13. Waveforms of the switched resonant bridge.

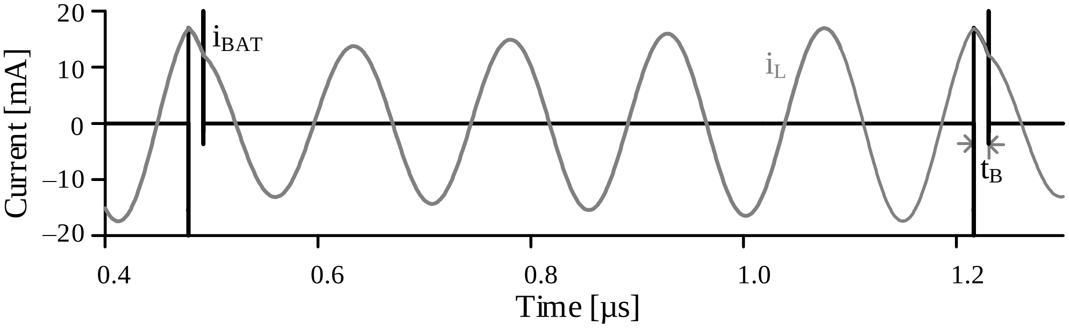

Figure 3-14. Skipped operation of the serially drained switched resonant bridge.

B. Power & Limits

Since the voltage impressed on L_R is sinusoidal, the switched resonant bridge's L_R can output as much power as a resonant bridge. A synchronizer senses i_L peak and configures the switches synchronously. As the serially drained switched resonant bridge can control its damping voltage v_C by adjusting t_{ON}, it does not require an additional MPP stage. So the system can be more compact and efficient. Moreover, as all the switches, S_R, D_G^+, D_G^-, D_O^+, and D_G^- are connected to either ground or v_B, the maximum damping voltage $v_{C(PK)}$ is not limited to V_{BD}. This means the circuit can reach MPP for a wider range of v_E.

3.4.2 Directly Drained Scheme

A variation of the serially drained switched resonant bridge is the directly drained scheme [125], as shown in Figure 3-15. The circuit operates in two modes: When S_C in Figure 3-15 connects, energy accumulates and exchanges between L_R and C_R. As a result, oscillation grows from cycle to cycle, as Figure 3-16 shows. When S_C disconnects, S_O connects and L_R drains its energy entirely and directly to v_B.

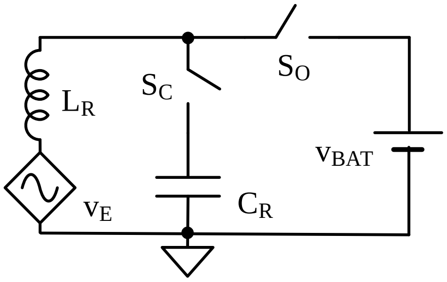

Figure 3-15. Directly drained switched resonant bridge power receiver.

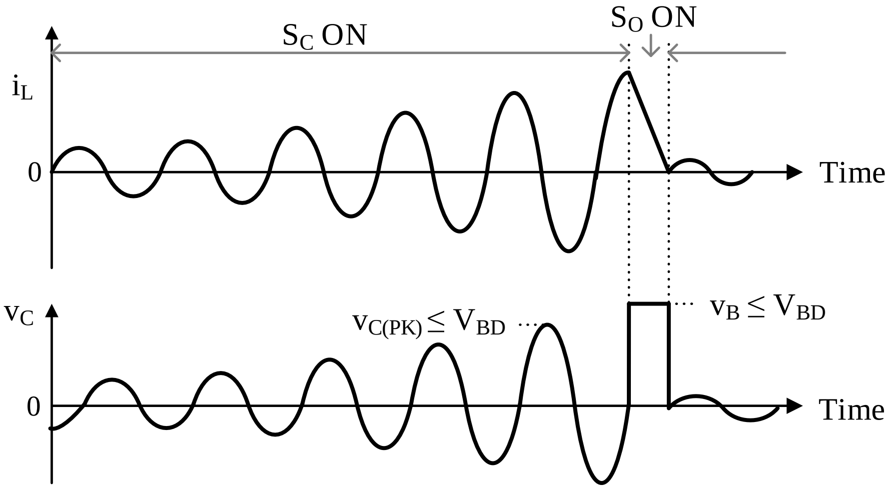

Figure 3-16. Waveforms of the directly drained switched resonant bridge.

Like the serially drained scheme, the directly drained scheme can adjust its damping voltage v_C by controlling t_{ON}. Therefore, it does not require an extra MPP stage. However, compared to the serially drained switched resonant bridge, the variant circuit's switches, S_C and S_O, see the oscillation voltage v_C. Therefore, its damping voltage is limited to V_{BD}.

3.5 Comparison

Figure 3-17 compares v_E's drawn power of different power receivers as a function of their damping voltage. To normalize the results, all power receivers use a 4 µH inductor with

7.85 Ω ESR at the operating frequency. Also, all power receivers operate at 12.5 MHz with 150 mV of coupled v_E. The rectified capacitor is much larger than C_R, so v_{REC} does not change instantaneously. The resonant full-bridge, the resonant half-bridge, and the switched resonant bridge all draws about the same P_E. This agrees with the analysis in 3.1 and 3.4. The investing switched bridge draws about 27% more power from v_E, as the investing switched bridge connects L_R to the highest v_{REC} or $–v_{REC}$ all the time. The result also agrees with our analysis in 3.3.2. The non-investing switched bridge is excluded in this comparison, due to its significant power disadvantage. Although the investing switched bridge draws more power from v_E, its simulated max receiver power $P_{L(MAX)}$ is about the same as the resonant bridges and the switched resonant bridges, as Figure 3-18 shows. This is because the conduction loss P_R in the investing switched bridge is also higher.

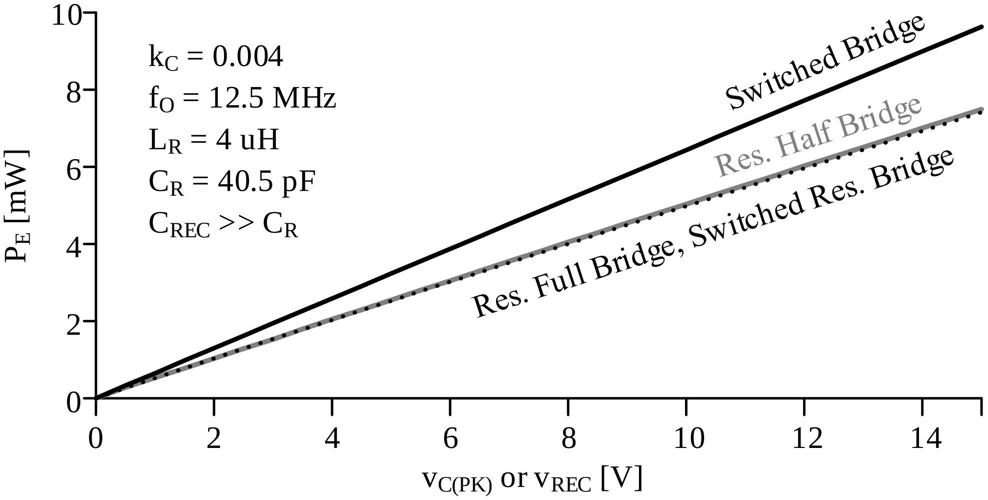

Figure 3-17. Simulated v_E's drawn power.

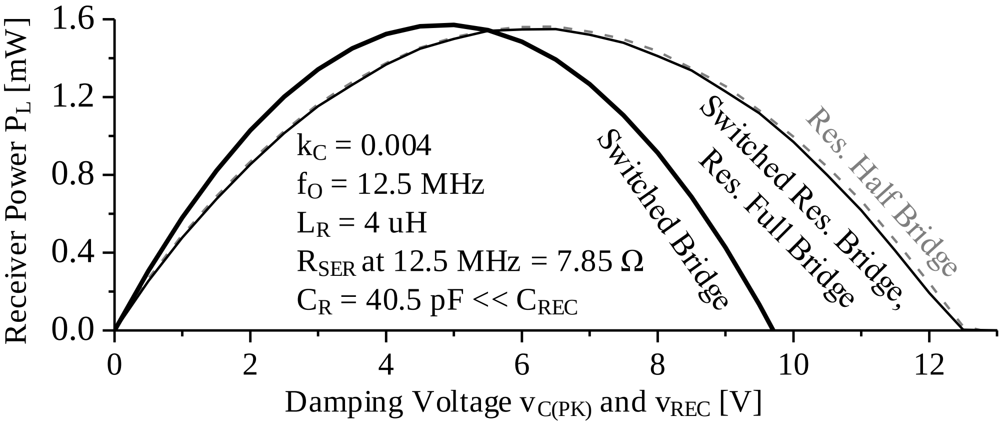

Figure 3-18. Simulated receiver power P_L.

Table 3-1 compares the state-of-the-art power receivers in terms of their power performance, breakdown limits, number of components and other limitations. The process of elimination is used to identify the best power receiver for targeted applications. The non-investing switched bridge is first eliminated due to its significant power disadvantage. Its averaged damping voltage is much lower compared to other power receivers, so its max receiver power is low as well. Next, the multiplying charge pump is eliminated as it outputs no more power than the resonant bridges but requires far more components and is more breakdown limited. The resonant half-bridge is eliminated as well. Although it requires only one switch, it is twice breakdown limited as the resonant full-bridge. Plus, it requires a negative supply, which complicates the design and adds cost. Then directly drained switched resonant bridge is eliminated as well as its serially drained counterpart offers the same performance but has a much higher breakdown limit.

Left are the resonant full-bridge, the investing switched bridge, and the serially drained switched resonant bridge. Among the three, the switched resonant bridge excels as it receives about the same power but requires no MPP buffer and has a much higher breakdown limit. The only challenge is the synchronizer that turns on and off the switches.

As will be discussed in CHAPTER 6, when properly designed, the loss from the synchronizing controller is only up to a few percentages of the output power. Therefore, the serially drained switched resonant bridge is the best power receiver topology overall.

Table 3-1. Comparison of SoA power receivers.

Power Receiver		Averaged Damping Voltage	$P_{L(MAX)}$	Breakdown Limit	Need MPP Charger	Components	Other Requirements
Charge Pump		$0.64v_{C(PK)}$	$\frac{v_{E(PK)}^2}{8R_R}$	$\frac{V_{BD}}{A_{CP}}$	Yes	L_R, L_{MPP}, C_R, 2N C_C, N C_O, 4N FETs	
Resonant Half-Bridge		$0.64v_{C(PK)}$	$\frac{v_{E(PK)}^2}{8R_R}$	$0.5V_{BD}$	Yes	L_R, L_{MPP}, C_R, 2 FETs	Negative supply
Resonant Bridge		$0.64v_{C(PK)}$	$\frac{v_{E(PK)}^2}{8R_R}$	V_{BD}	Yes	L_R, L_{MPP}, C_R, 4 FETs	
Switched Bridge	**Non-Investing**	$v_{E(PK)}$	$\frac{2v_{E(PK)}^2}{\pi Q_R R_R}$	V_{BD}	No	L_R, 4 FETs	Synchronizer
	Investing	$v_{C(PK)}$	$\frac{12v_{E(PK)}^2}{\pi^4 R_R}$	V_{BD}	Yes	L_R, L_{MPP}, 4 FETs	Synchronizer
Switched Resonant Bridge	**Serially Drained**	$0.64v_{C(PK)}$	$\frac{v_{E(PK)}^2}{8R_R}$	$>> V_{BD}$	No	L_R, C_R, 4 FETs	Synchronizer
	Directly Drained	$0.64v_{C(PK)}$	$\frac{v_{E(PK)}^2}{8R_R}$	V_{BD}	No	L_R, C_R, 2 FETs	Synchronizer

CHAPTER 4. COMPACT SWITCHED-RESONANT HALF-BRIDGE

As discussed in the previous chapters, Receiver coils in embedded microsensors are small and their transmitters are unpredictably distant and misaligned, so available power is low and variable. This chapter presents a 180-nm, 6.78-MHz switched resonant half-bridge that only uses two transistors with a transfer rate and duration that are both adjustable. This way, the prototype outputs 13%–85% of the 9.7–1580 μW that a 54.1-mm^2 receiver coil avails when 13 to 38 mm apart from its source. This is up to 38% more power and with a 25% smaller footprint than the best comparable receiver.

4.1 Power Stage

4.1.1 Operation

The basic principle in resonant receivers [6] is that L_R resonates with C_R at v_E's f_O. This way, L_R's current i_L and v_E are in phase, so v_E supplies power across positive and negative half-cycles. L_R and C_R receive and exchange this incoming energy until the switching network drains the tank into v_B.

The deadtime logic in Figure 4-1inserts dead time between M_G's and M_O's conduction periods to keep M_O and M_G from inadvertently draining v_B to ground. One minimum-sized gate and three inverters with transistors of increasing dimensions drive M_G and M_O. I_1 and I_2 are 2× larger than NAND and NOR gates, I_3 and I_4 are 4× larger than I_1 and I_2, and I_5 and I_6 are 4× larger than I_3 and I_4. Although 3× is the optimal gain for the shortest propagation delay, a higher gain reduces the number of inverter stages and the shoot-through power they consume [126].

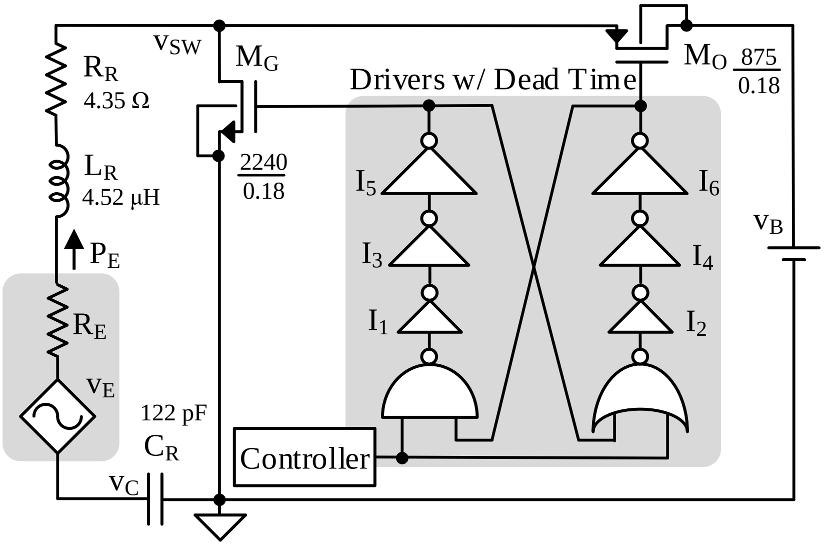
vSW
MG
RR
4.35 Ω
LR
4.52 µH
PE
RE
vE
122 pF
CR
vC
2240
0.18
Drivers w/ Dead Time
MO
875
0.18
I5
I3
I1
I6
I4
I2
vB
Controller

Figure 4-1. Proposed switched resonant half-bridge power receiver.

In the receiver proposed in Figure 4-1, the ground NMOS transistor M_G is normally on. So L_R and C_R receive and exchange the power that v_E continually supplies as P_E. As a result, C_R's energy E_C or $0.5C_Rv_C^2$ and voltage v_C rise from cycle to cycle. Then M_G opens and M_O closes, so the energy accumulated in the LC tank is transferred to v_B.

4.1.2 Energy Transfer

The receiver can transfer energy either every cycle or every few cycles. In Figure 4-2, the power receiver's M_G opens for 10 ns every cycle, so energy is transferred every cycle. As a result, each cycle's $v_{C(PK)}$ remains the same. Figure 4-3 shows the waveforms of the skipping operation. M_G opens for 37.5 ns after skipping N_S cycles (6 cycles in Figure 4-3), M_G opens and M_O closes for 37.5 ns to partially drain the L_RC_R tank into v_B. M_O opens and M_G closes after that. E_C and v_C grow again until the next time M_O and M_G partially drain the tank into v_B.

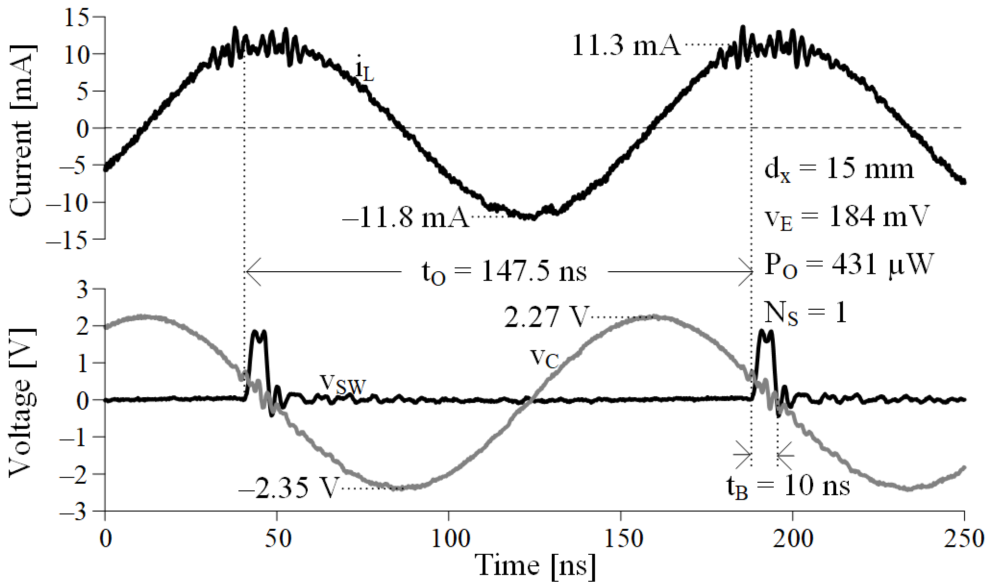

Figure 4-2. Waveforms of the non-skipping proposed switched resonant half-bridge.

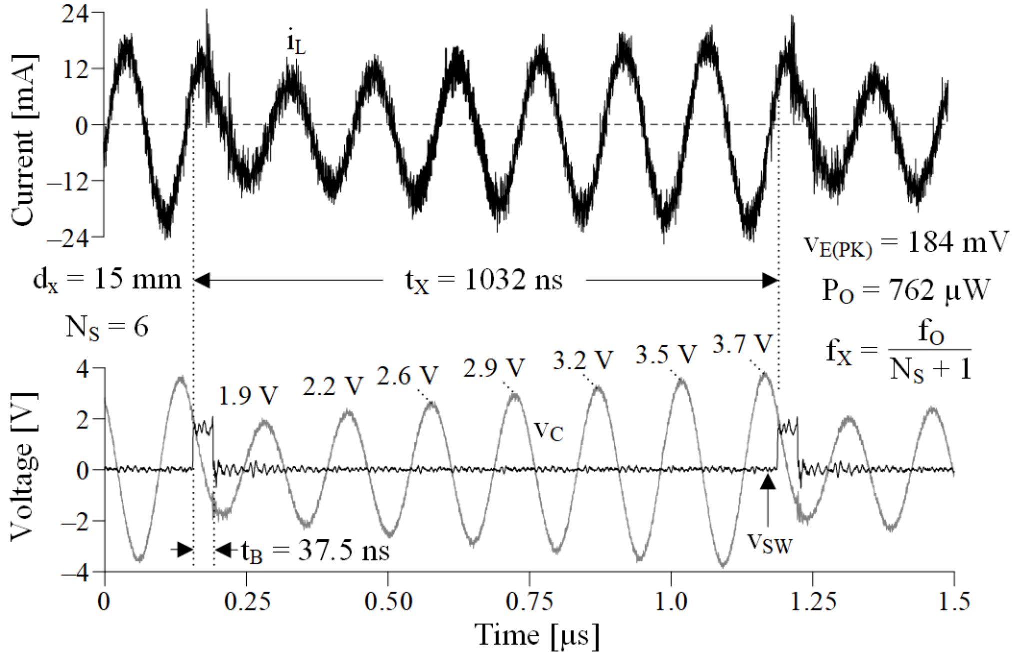

Figure 4-3. Waveforms of the skipping proposed switched resonant half-bridge.

The controller determines when to draw energy from the L_RC_R tank into v_B. It basically dictates when, how long, and how often M_O should drain L_R. To deliver as much power as possible in the shortest time, M_O steers L_R's *peak* current (at 200 ns) into v_B. Since L_R's energy E_L and current i_L peak when C_R's energy E_C and voltage v_C are zero, the controller bleeds L_R as v_C crosses zero. The duration t_{ON} and frequency f_X of these energy transfers depend on how much power L_R avails.

4.1.3 Assessment

Compared to the other switched resonant bridges [117-122], the proposed power stage uses 2 FETs only, so the power stage can be more compact and is more suitable for microsensor applications. Also, the resonant capacitor C_R is grounded. So there is less parasitic capacitance and thus less switching loss. This also makes sensing v_C easier, as will be discussed in CHAPTER 6. Moreover, the power stage uses synchronous switches, so there is no diode loss. Finally, the power stage can adjust both energy transfer frequency f_X and duration t_{ON}. The two-variable space captures more settings than a single variable can, so the maximum power $P_{O(MPP)}$ is higher.

4.2 Design

4.2.1 Parameters

M_G and M_O require gate-drive power P_{MG} to switch between states. They also burn ohmic power P_{MR} when they conduct i_L. Since MOS resistance R_{DS} and total equivalent switching capacitance C_{EQ} rise with channel length, M_G's and M_O's channel lengths are minimum length: 180 nm. R_{DS} falls and C_{EQ} rises with channel width. R_{DS} adds resistance to the LC oscillation loop and thus lowers the available power to the receiver. On the other hand, higher C_{EQ} raises the switching loss P_{SW}. Therefore, for minimum loss, M_G's and M_O's widths should balance the switching loss P_{SW} and the loss in available power when the receiver outputs 300 μW. This is the most probable power level for the blood-pressure monitors and glucose sensors targeted here [9, 10, 42, 127]. Optimizing M_G and M_O for the most likely setting saves (over time) the most energy.

The equivalent charge loss capacitance C_{EQ} includes the M_G gate capacitance C_{GN}, M_O's gate capacitance C_{GP}, M_O's source to well junction capacitance C_{JSW}, and M_G's drain to substrate junction capacitance C_{JDSUB}:

$$C_{GN} = C_{OX} " W_N L_N \,, \tag{4.1}$$

$$C_{GP} = C_{OX} " W_P L_P \,, \tag{4.2}$$

$$C_{JSW} = \frac{C_{J0} " A_{SW}}{\sqrt{1 - v_D / v_{BI}}} \,, \tag{4.3}$$

and

$$C_{JDSUB} = \frac{C_{J0} " A_{DSUB}}{\sqrt{1 - v_D / v_{BI}}} \,. \tag{4.4}$$

C_{EQ} also includes parasitic capacitance at the pins and the pads, which can be estimated from process and datasheets. The total C_{EQ} is estimated as:

$$C_{EQ} = C_{PIN} + C_{PAD} + C_{JDSUB} + C_{JSW} + (2^2 + 1)(0.5C_{GN}) + (2^2 + 1)(0.5C_{GP}) \,. \tag{4.5}$$

Note as the voltage swing across the C_{GD} (~$0.5C_{GN}$) of M_G and C_{GS} (~$0.5C_{GP}$) of M_O doubles v_B, their equivalent capacitance counts four times as much. In total, C_{EQ} includes 2.5 times of C_{GN} and C_{GP}.

$$C_{EQ} = C_{PIN} + C_{PAD} + C_{JDSUB} + C_{JSW} + (2^2 + 1)(0.5C_{GN}) + (2^2 + 1)(0.5C_{GP}) \,. \tag{4.6}$$

Therefore, the total switching loss P_{SW} can be calculated as:

$$P_{SW} = C_{EQ} v_B{}^2 f_X \,. \qquad (4.7)$$

The transmitter's resistance R_T limits how much current and power the source v_S can supply. Separation d_X and geometries of the coils then determine (via coupling factor k_C) what fraction of that power couples to L_R in the form of v_E. Although over-damping v_S is possible, d_X is so high and L_R is so small that only a small fraction of what the transmitter can supply loads v_S [77]. v_E is therefore low at hundreds of mV's.

With millimeter geometries, L_R's resistance R_R is high at 1–10 Ω [115, 116, 123, 124, 128]. Such a high R_R often overwhelms L_T's coupled (reflected) resistance R_C in L_R [129] and limits the current and power that v_E supplies to a level that hardly ever over-damps v_S. As discussed in CHAPTER 2, the maximum power $P_{O(MAX)}$ that a sinusoidal v_E (with peak $v_{E(PK)}$) can supply a load R_{LD} is

$$P_{O(MAX)} = \frac{v_{LD(PK)}{}^2}{2R_{LD}} = \frac{\left(0.5v_{E(PK)}\right)^2}{2\left(R_R + R_E\right)}, \qquad (4.8)$$

which happens when R_{LD} matches R_E + R_R where R_{LD} models the power the receiver absorbs, $v_{LD(PK)}$ is R_{LD}'s peak voltage, and $P_{O(MAX)}$ is the maximum power that L_R, R_C, and R_R avail. The ground switch M_G’s on-resistance adds to the LC tank’s ESR, lowering the available power to the receiver to:

$$P_{O(MAX)}{}' = \frac{\left(0.5v_{E(PK)}\right)^2}{2\left(R_R + R_E + R_{SWN}\right)}\,. \qquad (4.9)$$

Ignoring the non-linearity of the switched circuit, the max received power can be estimated by subtracting the switching loss P_{SW} from the reduced maximum available power $P_{O(MAX)}$':

$$P_{O(MPP)} \approx P_{O(MAX)}{}' - P_{SW} = \frac{\left(0.5v_{E(PK)}\right)^2}{2\left(R_R + R_E + R_{SWN}\right)} - C_{EQ} v_B{}^2 f_X \,. \tag{4.10}$$

Note that Eq. (4.10) assumes the M_O's on duty cycle is very small, so only M_G's on-resistance adds to the LC loop. This assumption is fairly is accurate at MPP when the coupled voltage v_E is low. The validation of this assumption will be discussed in the next chapter.

The optimal NMOS width $W_{N(OPT)}$ should maximize $P_{O(MPP)}$, so

$$\left.\frac{\partial P_{O(MAX)}{}'}{\partial W_N} - \frac{\partial P_{SW}}{\partial W_N}\right|_{W_N = W_{N(OPT)}} = 0 \,. \tag{4.11}$$

Obtaining a closed-form expression for $W_{N(OPT)}$ is difficult, as both $P_{O(MAX)}$' and P_{SW} are complex functions of W_N, as (4.1) to (4.10) show. So in practice, f_X at MPP is first obtained using simulation without W_N and W_P optimization. Then W_N is swept in simulation to find $W_{N(OPT)}$. At $W_{N(OPT)}$, W_P is swept again in simulation to find $W_{P(OPT)}$. Using this method, the optimal M_G's and M_O's widths are found to be 875 μm and 2240 μm, respectively.

Table 4-1 summarizes the parameters, design variables and implied power in calculation, simulation, and measurement. Since the MOSFET models are no longer available from the manufacturer after the IC is fabricated, the parameters for simulations are chosen such that the simulated R_{SWN}, R_{SWP}, and C_{EQ} closely match the calculation.

Measured R_{SWN} and R_{SWP} are higher than estimated values, so the available power $P_{L(MAX)}'$ is 1.3–1.7% lower.

Table 4-1. Parameter Summary

<table>
<tr><th colspan="4">Parameters</th></tr>
<tr><th>Parameter</th><th>Value</th><th>Parameter</th><th>Value</th></tr>
<tr><td>f_O</td><td>6.78 MHz</td><td>$v_{E(PK)}$</td><td>18–282 mV</td></tr>
<tr><td>k_C</td><td>0.07–1.13%</td><td>L_R</td><td>4.52 μH</td></tr>
<tr><td>C_R</td><td>122 pF</td><td>R_L</td><td>4.4 Ω</td></tr>
<tr><th colspan="4">Design Variables</th></tr>
<tr><th></th><th>Calculated</th><th>Simulated</th><th>Measured</th></tr>
<tr><td>R_{SWN}</td><td colspan="2">0.37 Ω</td><td>0.45 Ω</td></tr>
<tr><td>R_{SWP}</td><td colspan="2">3.7 Ω</td><td>5 Ω</td></tr>
<tr><td>C_{EQ}</td><td colspan="2">18.2 pF</td><td>16.5 pF</td></tr>
<tr><th colspan="4">Implied Power</th></tr>
<tr><th></th><th>Calculated</th><th>Simulated</th><th>Measured</th></tr>
<tr><td>$P_{O(MAX)}$</td><td colspan="3">9.2–1580 μW</td></tr>
<tr><td>$P_{O(MAX)}'$</td><td colspan="2">8.5–1490 μW*</td><td>8.4–1470 μW*</td></tr>
<tr><td>$P_{C(f_O)}$</td><td colspan="2">280 μW</td><td>252 μW</td></tr>
</table>

4.2.2 Maximum Output Power

Delivering $P_{O(MAX)}$ is only possible without other losses. Transistors, however, burn power P_{MR} when they conduct and gate-drive power P_{MG} when they switch. Plus, inverters consume shoot-through power P_{ST} when they transition. So the maximum power point (MPP) $P_{O(MPP)}$ results when added losses P_{LOSS} (R_C's P_{RC}, R_R's P_{RR}, P_{MR}, P_{MG}, and P_{ST}) cancel incremental gains in drawn power. Ohmic losses P_R (P_{RC}, P_{RR}, and P_{MR}) climb with output power and driver losses P_D (P_{MG} and P_{ST}) rise with transfer frequency. $P_{O(MPP)}$ is therefore the η_I fraction of $P_{O(MAX)}$ that losses set: $\eta_I \equiv P_{O(MPP)}/P_{O(MAX)}$. Note that this ideality index η_I hinges on finding the MPP.

The receiver transfers energy packets across a duration t_{ON} and at a rate f_X that the controller in Figure 4-1 sets. For f_X, the controller determines the number of cycles to skip N_S (in Figure 4-3) between energy transfers. So f_X is f_O or a fraction of f_O.

To find the MPP, one variable (f_X or t_{ON}) is fixed and the other swept to find the local $P_{O(MPP)}$. Then, with a new fixed value, the other variable is swept and the sequence is repeated to find all other $P_{O(MPP)}$'s (in Figure 4-4). After this process, the controller applies the setting that outputs the highest $P_{O(MPP)}$. Tracking $P_{O(MPP)}$ automatically adjusts for separation, alignment, process, and temperature variations.

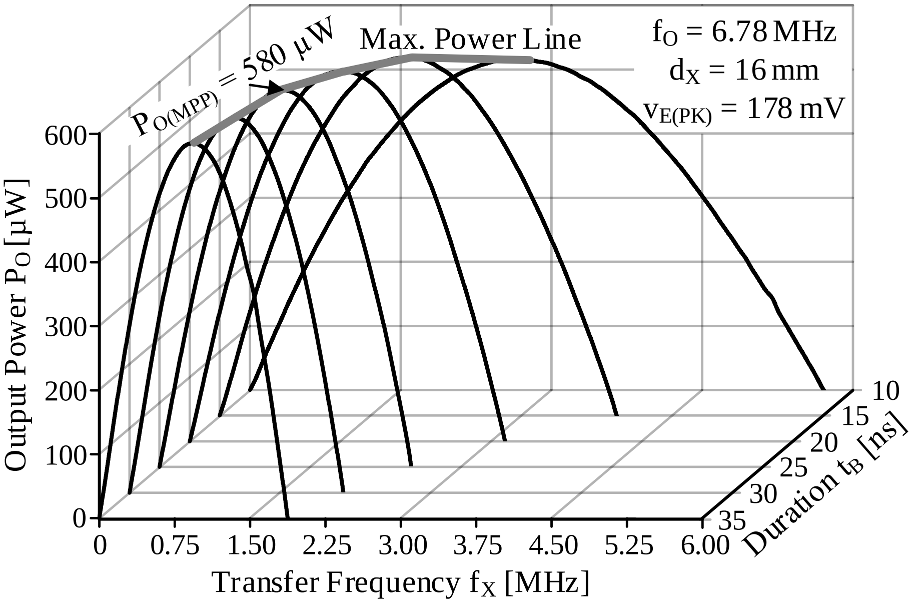

Figure 4-4. Measured output-power space when the coils are 16 mm apart.

$P_{O(MPP)}$ is lower when the coils are farther apart because more separation reduces L_T:L_R's coupling k_C. $P_{O(MPP)}$ in Figure 4-5, for example, is 24 µW at 15 ns and 420 kHz when the coils are 29 mm apart and R_C is 310 mΩ. So the system outputs 59% of the 40 µW that R_C and R_R avail with $v_{E(PK)}$'s 39 mV. t_{ON} is lower when farther apart because less power is available, so the receiver needs less time to transfer power. f_X is also lower because ohmic and driver losses P_R and P_D balance at a lower f_X when delivering lower power.

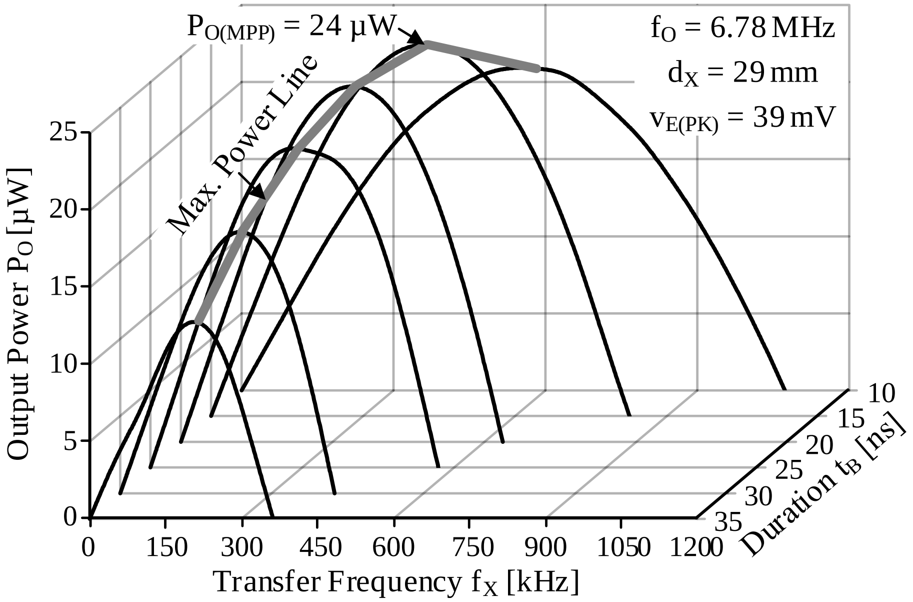

Figure 4-5. Measured output-power space when the coils are 29 mm apart.

The two-variable space in Figure 4-4 and Figure 4-5 capture more settings than a single variable can. With more settings, $P_{O(MPP)}$ can be closer to what R_C and R_R can avail with $P_{O(MAX)}$'. In Figure 4-6, below 17 mm, $P_{O(MPP)}$ is 1.5× to 3.6× higher than when fixing f_X to v_E's 6.78 MHz and adjusting t_{ON} to t_{ON}'s maximum power point $t_{ON(MPP)}$. By adjusting both t_{ON} and f_X, the system extends the harvestable distance 2.1× from 18 to 38 mm.

Relative to fixing f_X to f_O, $P_{O(MPP)}$ is 1.4× to 3.4× higher when fixing f_X to 1.2 MHz and adjusting t_{ON} to $t_{ON(MPP)}$. This is not much lower than when also adjusting f_X to $f_{X(MPP)}$. Losses are minimal across 16 mm at this f_X because $f_{X(MPP)}$ is 1.2 MHz when $v_{E(PK)}$ is 178 mV (at 16 mm). Losses, however, overwhelm drawn power at 28 mm when f_X is 1.2 MHz because f_X is no longer $f_{X(MPP)}$. In other words, the harvestable distance increases 1.4× when also adjusting f_X to $f_{X(MPP)}$.

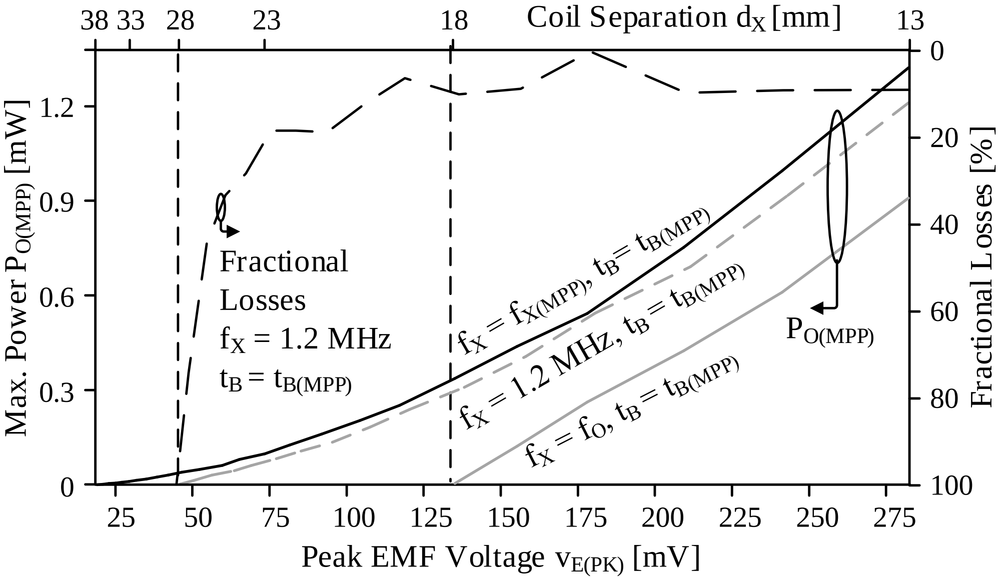

Figure 4-6. Measured maximum power when adjusting one and two variables.

4.2.3 Tuning Accuracy

Maximum output power hinges on tuning the receiver's resonant frequency to the transmitter's f_O. This way, i_L's and v_E's phases match so v_E always supplies power. A deviation in C_R reduces the power that v_E supplies, and as a result, reduces the power that the receiver outputs. In other words, C_R's deviation ΔC detunes the LC. A 1-pF offset from 122 pF, for example, reduces $P_{O(MPP)}$ up to 10% and a 5-pF offset reduces $P_{O(MPP)}$ up to 75%, as simulations in Figure 4-7 show.

Luckily, the controller can compensate for this loss by hastening or delaying transfers. When C_R is lower than targeted, for example, the tank becomes capacitive, so i_L lags v_E. Connecting the battery v_B to the tank sooner with a negative time offset t_{OS}, however, accelerates i_L's transition, which allows i_L to catch up to v_E. Delaying the transfer with a positive t_{OS} can similarly compensate a higher C_R. This way, $P_{O(MPP)}$ is 0.5% lower when C_R is off by 1 pF like Figure 4-7 shows and 22% lower when C_R is off by 5 pF. C_R in Figure 4-1 can therefore be laser-trimmed on-chip with ±1-pF accuracy.

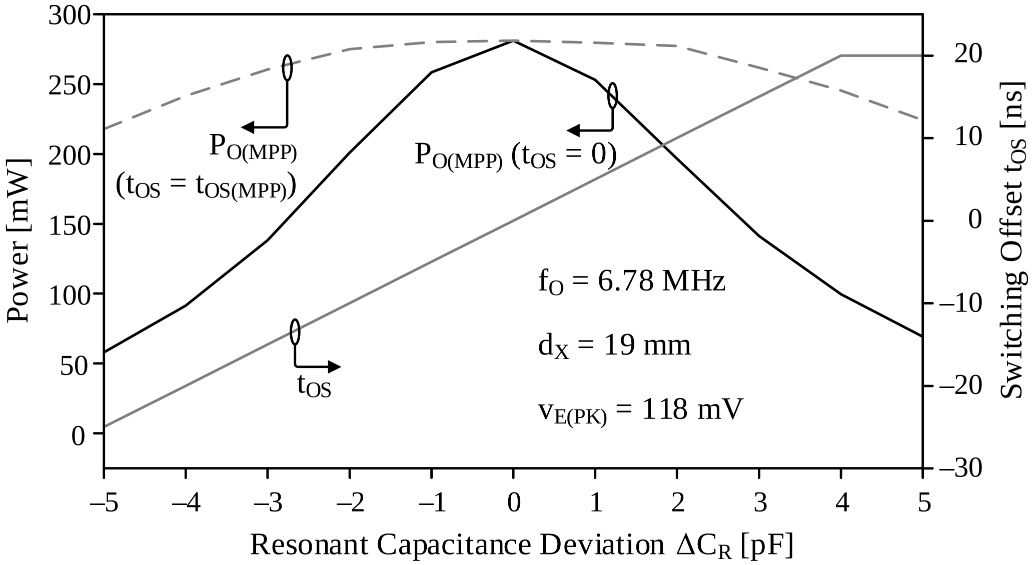

Figure 4-7. Simulated sensitivity of output power to tuning accuracy.

4.3 Measurements

4.3.1 Prototype

To evaluate the performance of the proposed power stage, an IC is fabricated with 180-nm CMOS technology. The fabricated die in Figure 4-8 integrates C_R, M_G and M_O, the gate drivers, and the dead-time logic. The IC occupies 644 µm × 732 µm. C_R is trimmed with a laser to 122 pF ±1 pF to ensure L_R and C_R resonate at 6.78 MHz. The receiver board in Figure 4-9 incorporates the packaged die, L_R, and a 100-nF v_B. The transmitter board in Figure 4-9 includes a half-bridge inverter. This half-bridge can supply up to 41 mW at 6.78 MHz (f_O). The diameters of L_T and L_R are 8 mm. The linear stage in Figure 4-10 adjusts the distance d_X between the coils from 13-mm to 38-mm. So their coupling factor k_C is 0.09% to 1.1%. An off-chip field-programmable array (FPGA) controls the transmitter and the receiver. This FPGA adjusts t_{ON} and f_X in open-loop fashion with interval steps of 5 ns and 53 kHz. For experimental and exploratory purposes, t_{ON} and f_X are adjusted manually. A practical implementation of the controller, however, should find and track the maximum power point automatically.

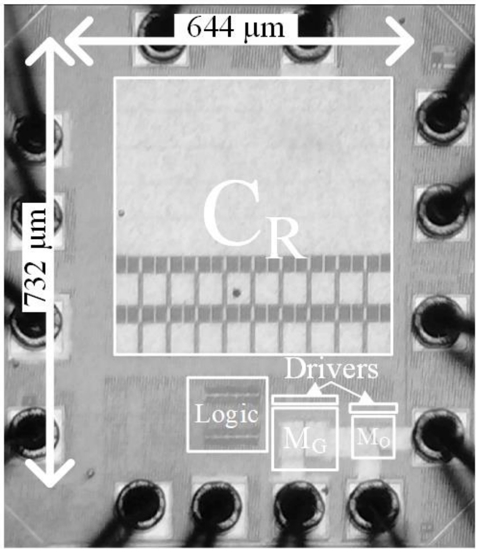
644 μm
732 μm
C_R
Drivers
Logic
M_G
M_O

Figure 4-8. Photograph of the fabricated power stage IC.

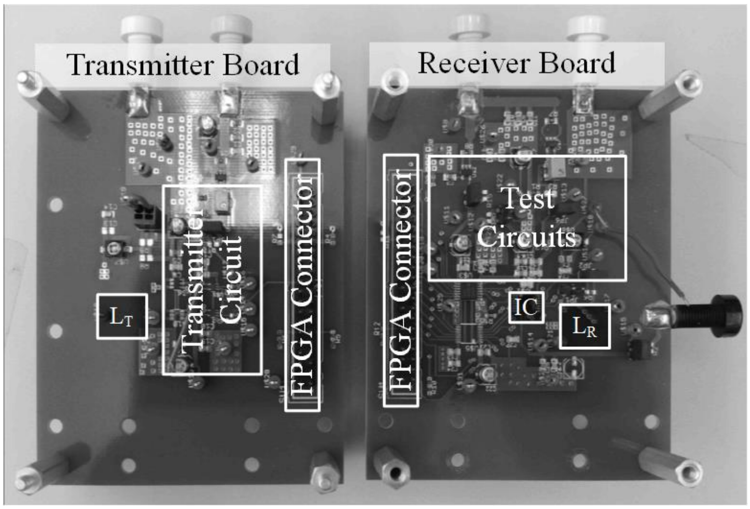
Transmitter Board
Receiver Board
L_T
Transmitter Circuit
FPGA Connector
FPGA Connector
Test Circuits
IC
L_R

Figure 4-9. Photograph of the power transmitter and receiver boards.

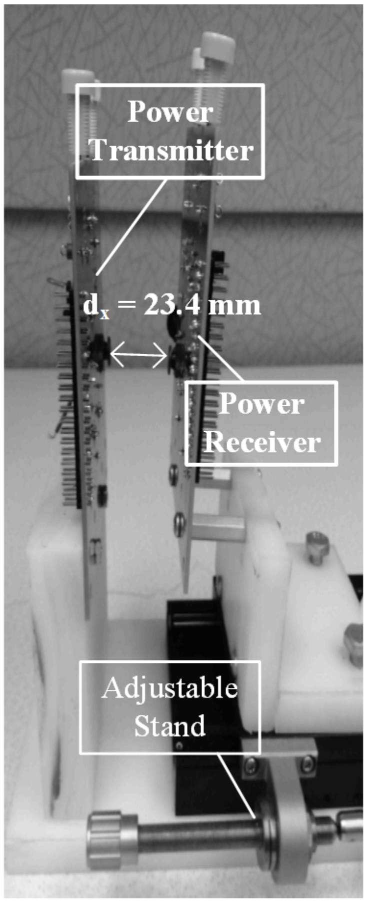

Figure 4-10. Photograph of the linear adjusting stage.

Since v_E is the unloaded EMF voltage induced in L_R, v_E is the open-circuit voltage across L_R. R_C models the receiver's damping effect on the transmitter's reflected source v_E [129]. So when short-circuiting v_E and R_C, R_C consumes the same power that v_S supplies when the transmitter is unloaded. $v_{E(PK)}$ and R_C in measurements are therefore L_R's peak open-circuit voltage and the equivalent resistance that burns v_S's power when the transmitter is unloaded.

4.3.2 Power and Losses

Losses P_{RR} in R_R dominate in Figure 4-11 because the diameter of the receiver coil is only 8 mm, so R_R is high at 4.35 Ω. Power lost P_{RC} to R_E is next, especially when the coils are within 18 mm (4.5 radial distances). At such short distances, the damping effect of the receiver in the transmitter is appreciably more significant. Driver losses P_D follow because MOS ohmic losses P_{MR} match (by design) gate-drive losses P_{MG}. So shoot-through losses P_{ST} raise P_D above P_{MR}'s level. The influence of process-, temperature-, and voltage-induced variations in MOS losses on $P_{O(MPP)}$ is therefore minimal.

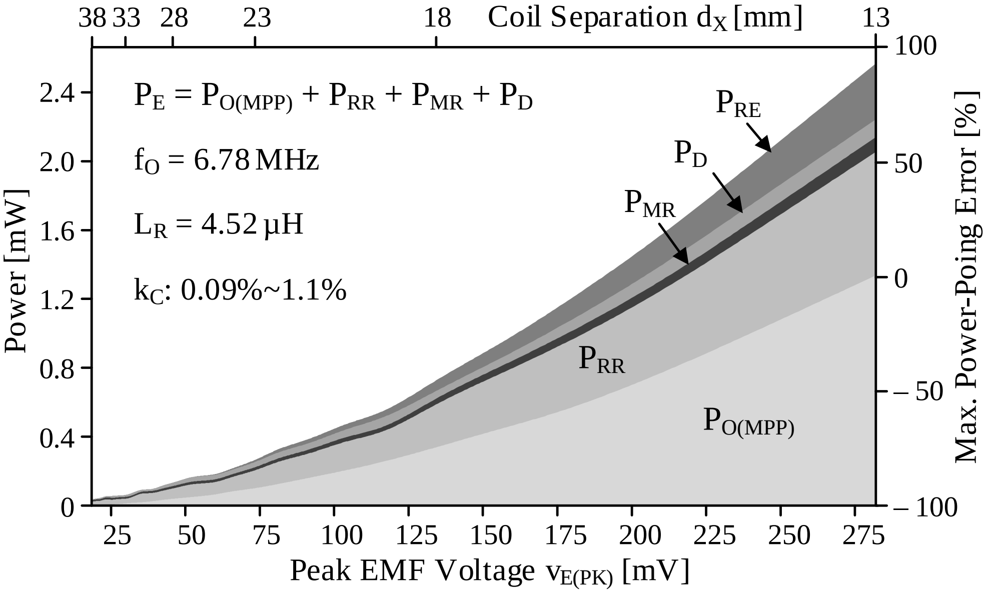

Figure 4-11. Measured losses and resulting maximum power.

Generally, ohmic losses P_R in P_{RE}, P_{RR}, and P_{MR} overwhelm driver losses P_D when the coils are within 18 mm. v_B connected periodically behaves like a resistive load because i_L is nearly sinusoidal. So like a resistive load would, P_R loses as much power as the load receives at the MPP [98]. At close range, as the receiver skips fewer cycles, i_L grows less between energy transfers. As a result, the circuit deviates little from the MPP, so $P_{O(MPP)} \approx P_{LOSS}$. When the coils separate farther, the circuit skips more cycles. As a result, the circuit deviates more from the MPP, so $P_{O(MPP)}$ does not match P_{LOSS}.

For reference, P_O here is the product of the average current into the battery (which was measured) and the battery's voltage v_B. Ohmic losses in Figure 4-11 is derived from measured resistances and currents: $P_R = i_{RMS}{}^2R_{EQ}$. Driver losses P_D were derived from the power supplied and lost to the drivers I_1–I_6 in Figure 4-1 separate power supply fed the drivers for this purpose: to measure P_D. Since v_E supplies v_B, ohmic losses, and P_D, sourced power P_E is $P_{O(MPP)}$ plus P_{RR}, P_{MR}, and P_D. But since the test probes used to measure these parameters add capacitance, *measured* losses are greater than *actual* losses by roughly 2–30 μW.

4.3.3 Charging Performance

The time-domain charging profile demonstrates how fast the power receiver can charge up a 100 nF capacitor to the supply voltage of 1.8V. At separation distances of 17, 20, and 23 mm, $v_{E(PK)}$ are 290, 184, and 118 mV, respectively.

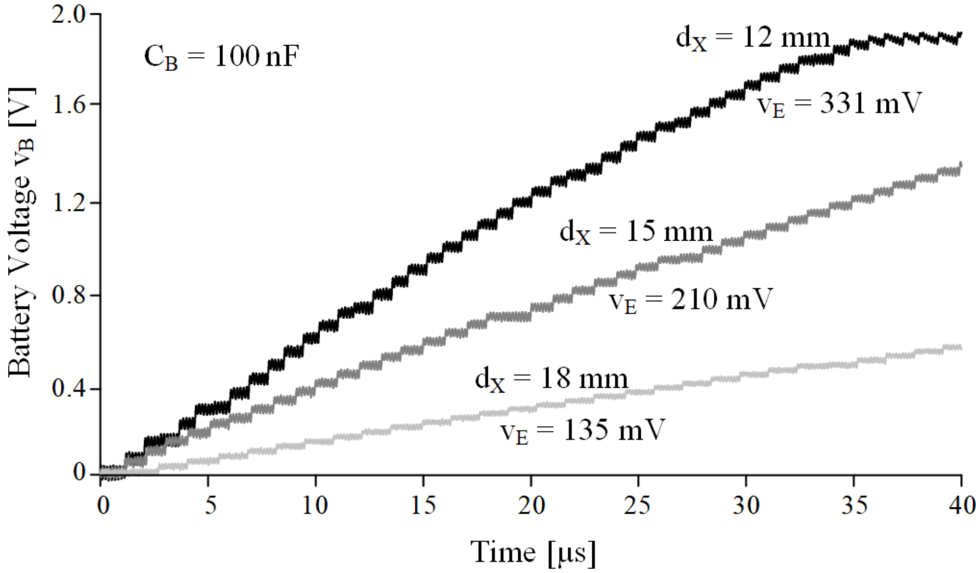

Figure 4-12. Measured charging profile of the switched resonant half-bridge.

The power receiver charges up C_B in 36, 64, and 180 μs, with 50, 28 and 10 mV/μs charging rage, respectively. As expected, higher $v_{E(PK)}$, availing quadratically more power to the receiver, charges C_B faster than lower $v_{E(PK)}$.

4.4 Relative Performance

P_O depends on the source v_S, transmitter's R_T, coil separation d_X and geometries, R_R, and the receiver. k_C comprehends the effects of d_X and coil geometries. η_I compares $P_{O(MPP)}$ with the power that v_S, R_T, k_C's v_E and R_C, and R_R avail. So η_I normalizes receiver performance to nearly all circumstances. This is why η_I is a good metric for comparing power receivers.

As Figure 4-13 shows, the prototype outputs 70% to 84% of the power that R_C's 0–1.9 Ω and R_R's 4.35 Ω avail when the coils are 13 to 28 mm apart. P_R limits η_I to 70%–84% across this distance. Since P_D does not scale with power like P_R, P_D's influence on η_I is increasingly worse past 28 mm. Decreasing t_{ON}'s and f_X's interval steps should improve η_I across 28–38 mm.

Table 4-2 compares the proposed switched resonant half-bridge to other state-of-the-art implementations. The ideality index η_I compares the maximum output power $P_{O(MPP)}$ with the power that transmitter's source voltage v_S, resistance R_T, coupling factor k_C receiver's resistance v_R can avail. η_I, therefore, normalizes the receiver performance to practically all surrounding circumstances. The proposed receiver achieves up to 85% η_I, which is 38% higher than other reported performance. The proposed receiver also requires the least number of components. Although the switched bridges do not need C_R, they require two more switches. Moreover, the synchronizer in a switched bridge needs to break the operation once every several to synchronize the operation. That is why [116], with an on-chip synchronizer, gets 18% less ηI than [115], which excludes the synchronizer loss. The FPGA that implements the function of the controller (and synchronizer) in Figure 4-1drains the LC tank when C_R's energy crosses zero. For this, the circuit can sense C_R's voltage v_C to ground, which is an indicator of C_R's energy $0.5C_Rv_C^2$. Sensing v_C this way, without interrupting the receiver like [116] does, is a significant improvement as the synchronizer sacrifices less power.

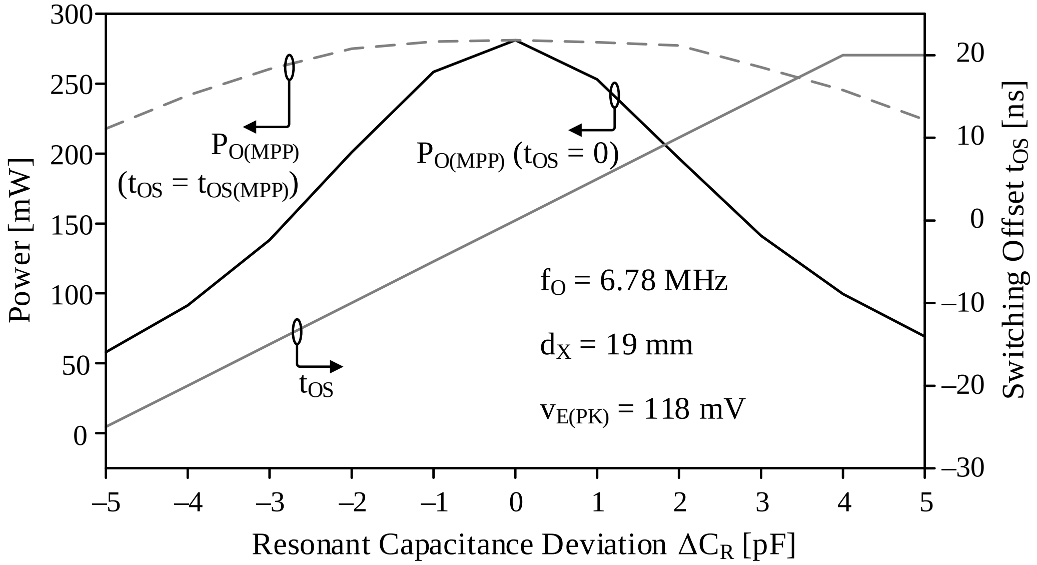

Figure 4-13. Available and measured output power and resulting ideality index.

The two-variable control in the proposed power receiver balances losses so the circuit can work at lower input power. In addition, since the power receiver's switches do not see the oscillation voltage v_C, V_{BD} does not limit v_C. This means, if v_E, R_C, and R_R can avail more power, C_R's energy can grow so that a higher i_L in L_R can draw this power. This is why the power range for the receiver proposed is vast at 1.2–1340 μW.

Table 4-2 Relative performance of the proposed power receiver.

	BioCAS [104]	JSSC [128]	TCAS II	JESTPE [116]	JSSC [124]	TCAS I [123]	JSSC [125]	This Work
	Switched Bridges			Switched	Switched Resonant Half-bridges			
Technology	350 nm	180 nm	180 nm	180 nm	350 nm	Board	180 nm	180 nm
Si Area A_{SI}	0.113 mm^2	0.490 mm^2	0.245 mm^2	0.260 mm^2	[A]3 mm^2	–	0.544 mm^2	0.471 mm^2
f_O	256 kHz	125 kHz	125 kHz	125 kHz	2.00 MHz	1.00 MHz	50 kHz	6.78 MHz
L_T	491 mm^2				15400 mm^2	22700 mm^2		54.1 mm^2
L_T	55 μH	400 μH	400 μH	345 μH	20 μH	4.4 μH	6.5 μH	4.5 μH
R_T at f_O		110 Ω	110 Ω	1.4 Ω	12 Ω	25 Ω	7.1 Ω	5.0 Ω
L_R	177 mm^2	107 mm^3	107 mm^3	107 mm^3	3320 mm^2	707 mm^2	107 mm^3	54.1 mm^2
L_R	55 μH	400 μH	400 μH	400 μH	20 μH	4.4 μH	6.5 μH	4.5 μH
R_R at f_O		9.7 Ω	9.7 Ω	9.7 Ω	6.1 Ω	0.95 Ω	0.11 & 0.13 Ω	4.4 Ω
d_X	10 mm	0–10.6 mm		10–50 mm	80 mm	70 mm	85 mm	
k_C		0.59%–6.7%	0.9%–7.6%		5%	1.3%[A]		0.09%–1.1%[B]
R_C		0.18–16 Ω[C]	0.23–25 Ω[C]	0.04–3.7 Ω[C]			0–1.9 Ω[C]	
$v_{E(PK)}$		39.5–386 mV	46–480 mV	66–585 mV		41 mV[D]		18.5–282 mV[B]
$P_{O(MAX)}$		19.7–724 μW	26.6–830 μW	55.9–3190 μW		224 μW[D]	9.72–1580 μW	
$P_{O(MPP)}$		0–224 μW	8–390 μW	16–557 μW	1.45 W	96.1 μW	0–2.84 μW	1.2–1340 μW
η_I		0%–30.9%	29.6%–46.9%	17.5%–28.6%		42.9%		12.3%–84.8%
$P_{O(MPP)}/A_{SI}$		0.457	1.59 mW/mm^2	2.14 mW/mm	483 mW/mm^2		5.22 μW/mm^2	2.84 mW/mm^2
Components	L_R, C_R, 4	L_R, 4 FETs	L_R, 4 FETs	L_R, 4 FETs	L_R, C_R, 5	L_R, C_R,	L_R, C_R, 2	L_R, C_R, 2

[A]Estimate for rectifier only. [B]Projections from L_R's quality factor. [C]Calculated from v_S, v_E, R_T, and R_R. [D]$v_{E(PK)}$ includes R_C's voltage so

Overall, the 180-nm 6.78-MHz switched resonant half-bridge power receiver proposed and prototyped outputs 1.2–1340 μW of the 9.72–1580 μW that a 54.1-mm^2 receiver coil with 4.4 Ω avails when 13–38 mm apart from a 54.1-mm^2 transmitter coil. The system delivers 38% more power with 25% less space than the best comparable in its class. The power range is wide because, unlike other half bridges, the switches' breakdown voltage does not limit the energy in the resonating tank. The higher coil current that results from resonating more energy can draw more power (when available). Output power is higher because selectively switching two optimal transistors within and across cycles burns less power and avails more settings from which a higher maximum point can result. Transferring this much and this range of power is vital for structurally embedded microsensors and biomedical implants, which are small, immobile, in the dark, and often misaligned and across variable distances from a transmitting source.

4.5 Remaining Challenges

As discussed above, the proposed switched resonant half-bridge power stage can output up to 38% more power with a 25% smaller footprint than the best comparable receiver. However, two more challenges remain for the proposed power stage. The first challenge is the synchronized control. To send energy to the battery, the ground switch M_G and the output switch M_O need to turn on and off synchronously as i_L peaks. The FPGA in Figure 4-14 connects both the power transmitter board and the power receiver board. This way, the receiver's switches are synchronized with the transmitter's input and i_L's peak. However, the wired connection between the transmitter and the receiver defeats the purpose of wireless power transfer. For real applications, the receiver needs to synchronize its operation itself. The second challenge is the MPP control. The proposed switched resonant half-bridge can adjust both energy transfer frequency f_X and energy transfer duration t_{ON} for MPP. However, measuring power across all the possible settings is both time- and power-consuming. Therefore, an MPP theory is needed to predict the best settings for max power.

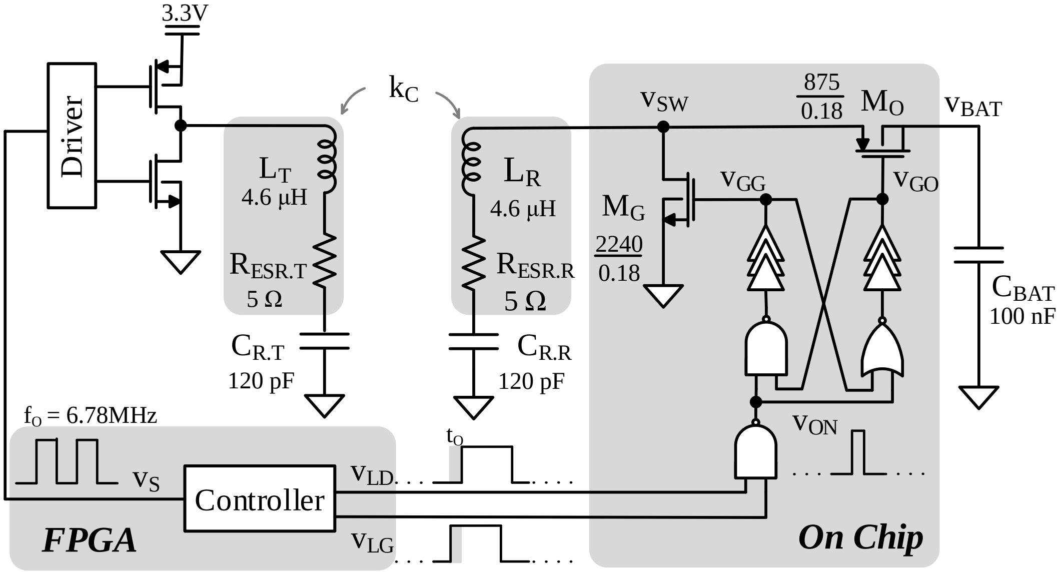

3.3V
Driver
kC
LT
4.6 µH
RESR.T
5 Ω
CR.T
120 pF
LR
4.6 µH
RESR.R
5 Ω
CR.R
120 pF
vSW
875
0.18
MO
vBAT
vGG
vGO
MG
2240
0.18
CBAT
100 nF
vON
fO = 6.78MHz
vS
Controller
vLD
tO
vLG
FPGA
On Chip

Figure 4-14. FPGA synchronizes the transmitter and the receiver.

The next two chapters are dedicated to addressing the two remaining challenges of the proposed switched resonant half-bridge power stage. The MPP theory proposed in CHAPTER 5 predicts the MPP setting with a 98.7% accuracy. CHAPTER 6 discusses the self-synchronization techniques for the proposed switched resonant half-bridge.

CHAPTER 5. THE HIGHEST MAXING POWER POINT

The proposed switched resonant half-bridge adjusts both energy transfer duration and frequency for MPP. However, searching for the optimal f_X and t_{ON} setting thoroughly across the two-variable space can be time- and energy-consuming. Also, coupling varies from time to time in most embedded microsensor applications, which means the optimal setting also needs to be adjusted from time to time. Searching for MPP setting frequently halts the power transfer and causes significant opportunity loss. That's why in this chapter, an MPP theory is developed to predict the optimal setting of the proposed power stage. The theory predicts the optimal time, duration, and frequency of the energy transfers that charge the battery. Measurements of a 0.18-μm CMOS power receiver demonstrate that the receiver outputs more than 98.7% of the actual MPP at the predicted settings when the coupling factor between the transmitting and receiving coils is 0.15%–1.14%.

5.1 Highest Power-Generating Receiver

As discussed in CHAPTER 3 and CHAPTER 4, the switched resonant half-bridge and resonant bridge draw about the same maximum power as the resonant bridge and the switched bridge. However, the switched resonant half-bridge does not require an MPP stage. This is because by controlling the frequency and the duration of energy transfer the circuit can adjust $v_{C(PK)}$ so it remains near $v_{C(OPT)}$. For the proposed switched resonant half-bridge shown in Figure 5-1, since S_G and S_O do not see v_C, V_{BD} does not limit $v_{C(PK)}$. Therefore, the proposed power stage can generate the highest power across a wide coupling range. The problem of finding the highest power-generating receiver reduces to finding the optimal operation settings of the switched resonant half-bridge power stage.

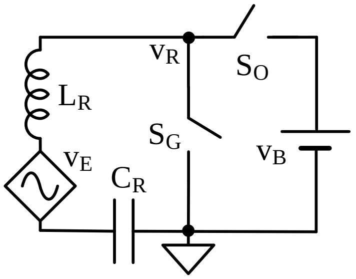

Figure 5-1. Switched resonant half-bridge for highest MPP.

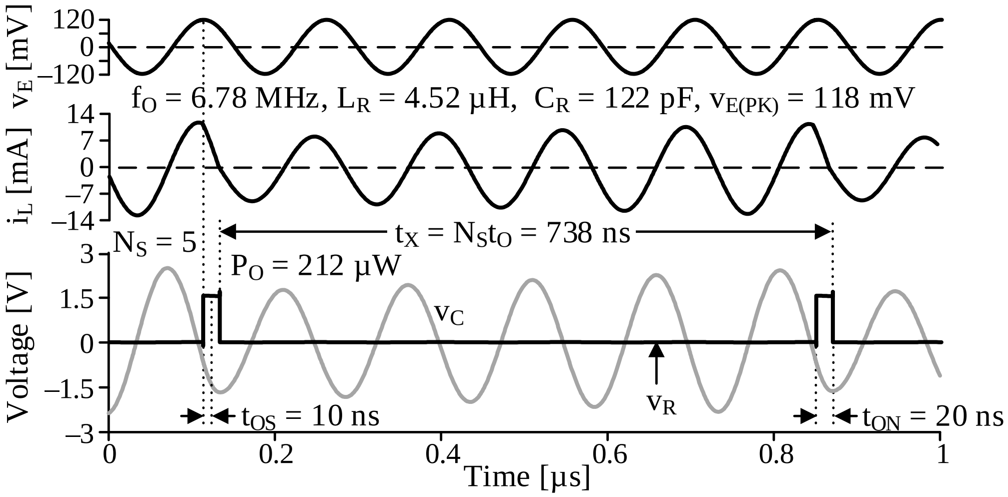

Figure 5-2. Energy transfer frequency, duration, and offset of a switched resonant half-bridge power receiver.

The proposed power stage can adjust its energy transfer frequency and duration for MPP [130]. In addition, the phase offset can be adjusted as well to compensated for the detuning caused by inaccurate C_R [130]. This chapter presents a theory that predicts the optimal (maximum power-point) settings for frequency, duration, and phase, which [130] did not include. The phase offset t_{OS} is the phase difference between the receiver voltage v_R and the coupled voltage v_E. When t_{OS} is zero, v_E peaks halfway across v_R's pulse. For example, in the simulated waveforms of Figure 5-2, as the center of v_R's pulse lags v_E's peak by 10 ns, t_{OS} is 10 ns. The circuit can also adjust the energy-transfer frequency f_X by setting the number of cycles N_S between two consecutive transfers. In Figure 5-2, as the circuit transfers energy to v_B every 5 cycles, the energy transfer period t_X is 5 times of the cycle period t_O so the energy transfer frequency f_X is $f_O/5$. Finally, the circuit can adjust the duration t_{ON} of the transfer: the time that the LC tank connects to v_B. In Figure 5-2, v_B drains L_RC_R for 20 ns, so the t_{ON} is 20 ns.

5.2 Maximum Power Point

The theory below finds MPP settings $t_{OS(MPP)}$, $t_{ON(MPP)}$, and $f_{X(MPP)}$ in two steps. The theory first finds the optimal t_{OS} and t_{ON} settings that maximize P_O at a given f_X. The optimal settings derived $t_{OS(MPP)}'$ and $t_{ON(MPP)}'$ are "local" because they vary with f_X. As will be shown, $t_{OS(MPP)}'$ and $t_{ON(MPP)}'$ are the t_{OS} and t_{ON} that ensure $v_{R(PK)}$'s f_O^{th} harmonic is $0.5v_{E(PK)}$. The optimal "global" setting derived for f_X in step two ($f_{X(MPP)}$) minimizes the losses at this point: when $v_{R(PK)}^{fO}$ is $0.5v_{E(PK)}$. With this, the optimal global setting for t_{ON} ($t_{ON(MPP)}$) is now known: from $t_{ON(MPP)}'$ in step one and $f_{X(MPP)}$ in step two.

5.2.1 Optimal Receiver Voltage

Figure 5-3 models the series-switched resonant receiver. The transmitter couples an open-circuit voltage v_E in L_R. R_E is the reflected resistance from the transmitter [75]. As the receiver draws power, it loads the transmitter, so it lowers the current in the transmitting coil as well as the coupled voltage on L_R. The voltage dropped across R_E models this loading effect. The power receiver is modeled as a series load with a terminal voltage v_R. According to the maximum power transfer theory [98], as the C_R and L_R's voltage cancels each other, the receiver receives the maximum power when v_R shares half of the source voltage v_E, like Figure 5-4 shows.

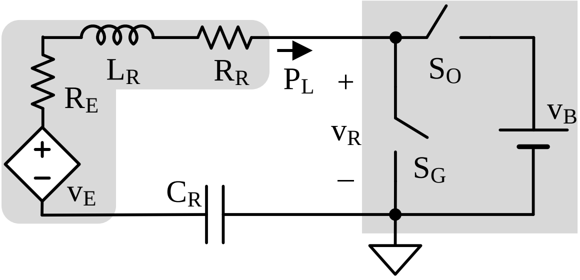

Figure 5-3. Power model of the switched resonant half-bridge power receiver.

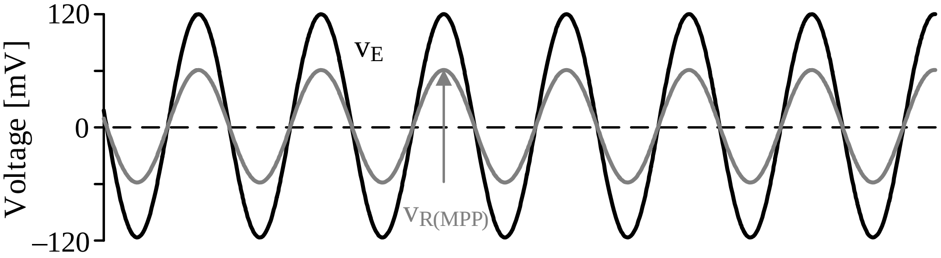

Figure 5-4. Ideal receiver voltage v_R to maximize receiver power.

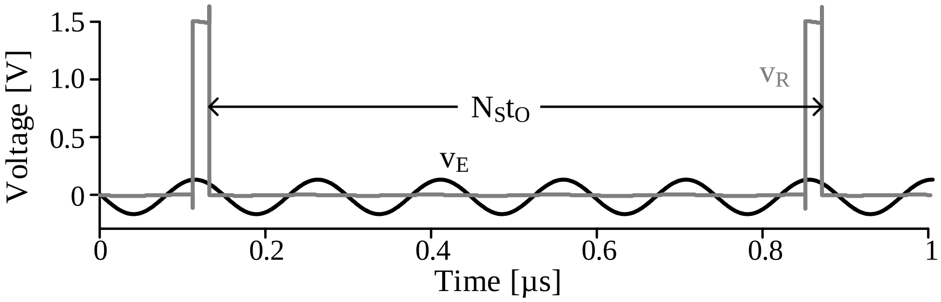

Figure 5-5. Receiver voltage v_R of a switched resonant half-bridge.

In reality, the receiver is a switched network as Figure 5-3 shows. When S_G closes, the ground switch shorts L_R and C_R, so v_R Figure 5-3 is zero. When S_O closes, L_R is connected to v_B, so v_R equals v_B. As the circuit switches periodically, v_R's waveform is a pulse train, as shown in Figure 5-5. Therefore, the receiver voltage v_R of a switched resonant half-bridge cannot be a sinusoidal waveform that matches $0.5v_E$.

However, the receiver voltage v_R is periodical with a N_St_O period, where N_S is the number of cycles between two energy transfers. The Fourier Series can decompose any periodical signal as a series of sinusoidal waves at harmonic frequencies that are multiples of the fundamental frequency. In this case, the fundamental frequency f_X is f_O/N_S. Assume that v_R is symmetrical at the time origin, all the integrations in Therefore, v_R can be expanded as:

$$\begin{aligned} v_R = a_0 + a_1 \cos\left(\frac{2\pi f_O t}{N_S}\right) + a_1 \cos\left(\frac{4\pi f_O t}{N_S}\right) + \ldots + a_{N_S} \cos\left(2\pi f_O t\right) + \ldots \\ + b_1 \sin\left(\frac{2\pi f_O t}{N_S}\right) + b_1 \sin\left(\frac{4\pi f_O t}{N_S}\right) + \ldots + b_{N_S} \sin\left(2\pi f_O t\right) + \ldots \end{aligned}, \quad (5.1)$$

where

$$a_1 = \frac{1}{N_S t_O} \int_{-0.5N_S t_O}^{0.5N_S t_O} v_R dt\ , \quad (5.2)$$

$$a_i = \frac{2}{N_S t_O} \int_{-0.5N_S t_O}^{0.5N_S t_O} v_R \cos\left(\frac{2i\pi f_O}{N_S}\right) dt\ , \quad (5.3)$$

and

$$b_i = \frac{2}{N_S t_O} \int_{-0.5T_O}^{0.5T_O} v_R \sin\left(\frac{2i\pi f_O}{N_S}\right) dt\ . \quad (5.4)$$

Assume that v_R is symmetrical at $t = 0$. All the integrations for b_i in (5.4) result in 0. a_i can be calculated as:

$$a_i = \frac{2}{N_S T_O}\int_{-0.5t_{ON}}^{0.5t_{ON}} v_B \cos\left(\frac{2i\pi f_O}{N_S}\right)dt = \frac{2v_B}{i\pi}\sin\left(\frac{i\pi t_{ON}}{N_S t_O}\right), \tag{5.5}$$

and

$$a_0 = \frac{1}{t_O}\int_{-0.5t_{ON}}^{0.5t_{ON}} v_B = \left(\frac{t_{ON}}{t_O}\right)v_B. \tag{5.6}$$

Note v_R's N_S-th harmonic frequency is the oscillation f_O. Its magnitude is:

$$a_{N_S} = \frac{2v_B}{N_S\pi}\sin\left(\frac{t_{ON}}{t_O}\pi\right). \tag{5.7}$$

The reason for expanding v_R as a Fourier series is that the resonant L_RC_R in Figure 5-3 only band-passes current at f_O. For v_R's other harmonics, L_RC_R behaves as a high impedance and blocks the current path. Therefore, v_R's harmonic at f_O dominates the current and the conduction loss. Therefore, analogous to the linear maximum power transfer theory [98], the proposed theory asserts that at given f_X the receiver draws maximum power when v_R's harmonic at f_O matches $0.5v_E$ in both amplitude and phase:

$${v_{R(PK)}}^{(f_O)} = 0.5v_{E(PK)}, \tag{5.8}$$

and

$$\angle {v_R}^{(f_O)} = \angle v_E. \tag{5.9}$$

The accuracy of the assertions in Eq. (5.8) and Eq. (5.9) will be validated later in this chapter. From Eq. (5.9), since v_R's harmonic at f_O and v_E are in phase, the center of the pulse aligns with v_E's peak. Therefore, the phase offset at the local and the global MPP is zero:

$$t_{OS(MPP)} = t_{OS(MPP)}{}' = 0\,. \tag{5.10}$$

Combining Eq. (5.7) and Eq. (5.8) relates $t_{ON(MPP)}'$ and t_X:

$$v_{R(PK)}{}^{(f_O)} = \left(\frac{2}{\pi}\right)\left(\frac{f_X}{f_O}\right) v_B \sin\left[\pi\left(\frac{t_{ON}}{t_O}\right)\right]\Bigg|_{t_{ON(MPP)}'} = \frac{v_{E(PK)}}{2}\,. \tag{5.11}$$

Solving Eq. (5.11) yields:

$$t_{ON(MPP)}' = \left(\frac{t_O}{\pi}\right)\sin^{-1}\left[\left(\frac{\pi}{4}\right)\left(\frac{v_{E(PK)}}{v_B}\right)\left(\frac{f_O}{f_X}\right)\right]. \tag{5.12}$$

Equation (5.12) calculates the optimal $t_{ON(MPP)}'$ for given f_X. With $t_{ON(MPP)}'$ obtained, the next step is to find the global optimal $f_{X(MPP)}$ that minimizes the overall losses when $v_{R(PK)}{}^{(f_O)} = 0.5v_{E(PK)}$.

To validate the conclusion in Figure 5-6 plots the simulated and measured P_O across t_{OS} when f_X = 850 kHz and t_{ON} = 25 ns. In measurement, t_{OS} is adjusted from zero in either direction with a 1.25 ns resolution. In both simulation and measurement, the circuit outputs the highest power when $t_{OS} = 0$. P_O drops as t_{OS} deviates from zero in either direction.

To validate the MPP criteria in (5.8), Figure 5-7 plots the calculated, simulated, and measured $v_{R(PK)}{}^{(f_O)}$ at MPP when k_C is 0.07–1.13%. At $k_C > 0.15\%$, both simulated and measured is within 4% of $0.5v_{E(PK)}$, corroborating the theory well. However, when k_C is less than 0.15%, the measured $v_{R(PK)}^{(f_O)}$ deviates up to 21% from $0.5v_{E(PK)}$. The increased error is mostly due to the finite resolutions for t_{ON} and f_X. In measurement, t_{ON} is adjusted with a 5 ns resolution, and f_X is adjusted with a 53 kHz resolution, respectively, due to measurement equipment's limitation.

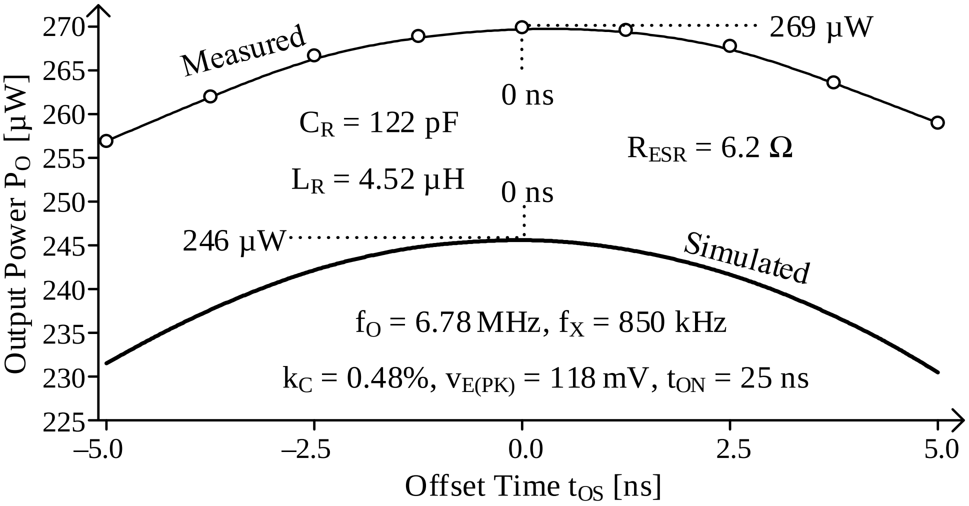

Figure 5-6. Output power across offset time.

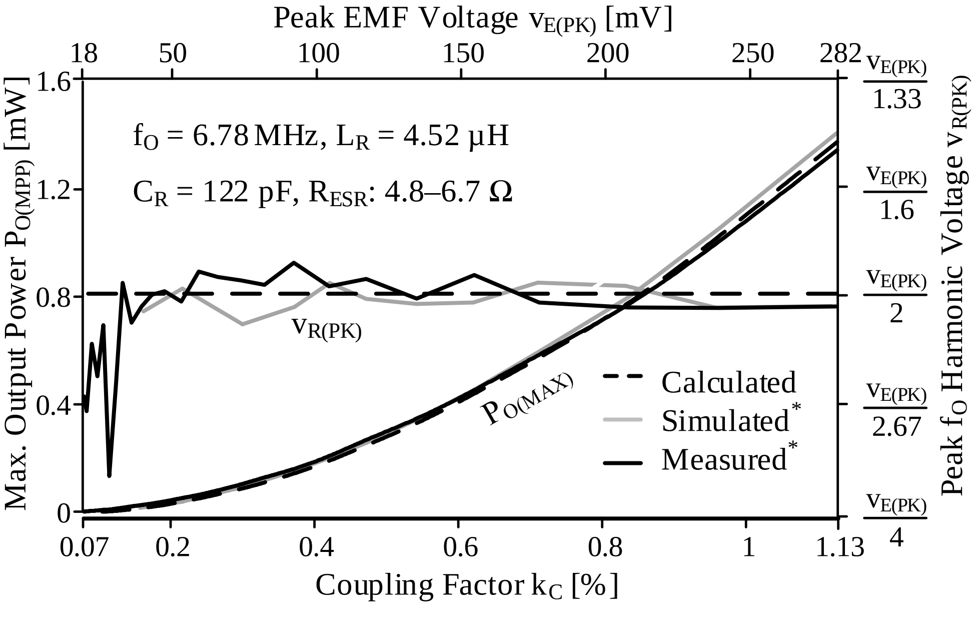

[*] $v_{R(PK)}$ is derived from (5.11) using simulated or measured $t_{ON(MPP)}$ and $f_{X(MPP)}$.

Figure 5-7. Maximum output power and receiver's peak f_O harmonic voltage.

Figure 5-8 plots the simulated and measured P_O across t_{ON} when $f_X = 0.125f_O$. The simulated P_O peaks at t_{ON} = 23 ns, deviating 1 ns from the theory's predicted 24 ns. The measured P_O peaks at t_{ON} = 25 ns with 5 ns resolution. Simulated k_{SW} ranges from 0.86% to 1.14%. Figure 5-6 plots the simulated and measured P_O across t_{OS} when f_X = 850 kHz and t_{ON} = 25 ns. In both simulation and measurement, the circuit outputs the highest power when $t_{OS} = 0$. P_O drops as t_{OS} deviates from zero in either direction. Figure 5-7 plots the calculated, simulated, and measured $v_{R(PK)}$'s harmonic at f_O at MPP when k_C is 0.07–1.13%. At $k_C > 0.15\%$, both simulated and measured $v_{R(PK)}$'s harmonic at f_O is within 4% of $0.5v_{E(PK)}$, corroborating the theory well. However, when k_C is less than 0.15%, the measured $v_{R(PK)}$'s harmonic at f_O deviates up to 21% from $0.5v_{E(PK)}$, due to the finite resolutions for t_{ON} and f_X (5 ns and 53 kHz, respectively).

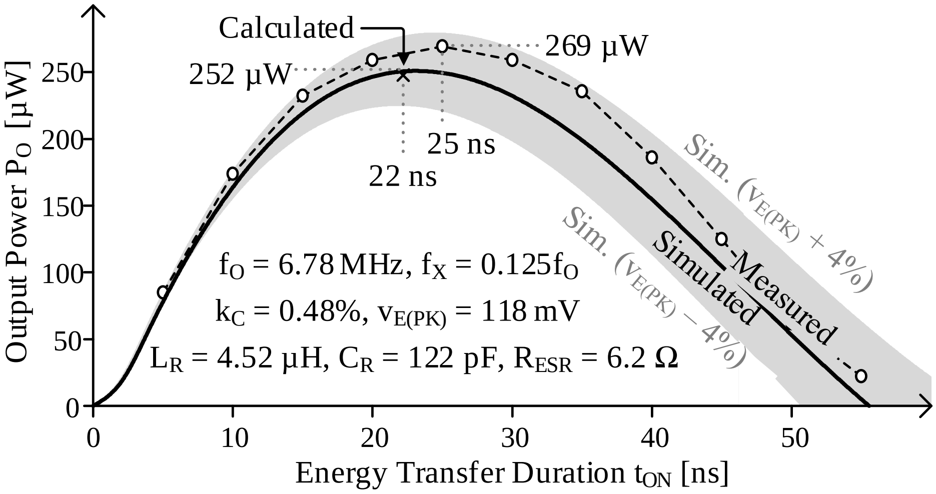

Figure 5-8. Output power across duration.

To evaluate the accuracy of the predicted $t_{ON(MPP)}'$ in (5.12), Figure 5-9 compares the calculated, simulated, and measured $t_{ON(MPP)}'$ across f_X with 118 mV of $v_{E(PK)}$ and 6.2 Ω of R_{ESR}. While the simulated $t_{ON(MPP)}'$ closely matches the theory' prediction, the measured $t_{ON(MPP)}'$ has a resolution of 5 ns and reflects the trend of prediction.

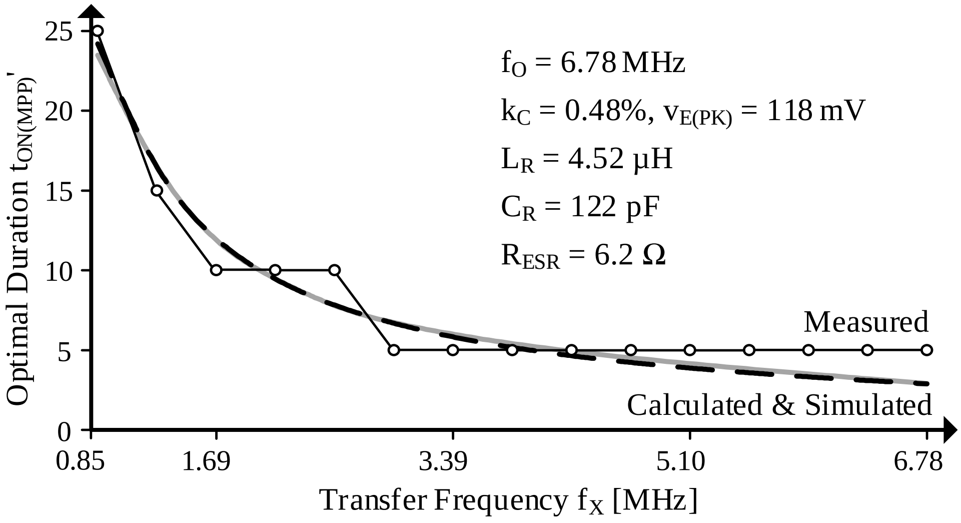

Figure 5-9. Optimal duration.

5.2.2 *Optimal Transfer Frequency*

The next step for MPP is to find the optimal f_X that maximizes the global P_O with the corresponding $t_{OS(MPP)}$' and $t_{ON(MPP)}$' found in the previous step. The global $f_{X(MPP)}$ needs to minimize the total losses of the switched resonant half-bridge. Therefore, it is necessary to first identify all the losses of the circuit.

A. Nonlinear Loss

As discussed in 2.4, the receiver receives the maximum power when it impresses an optimal voltage v_{MPP} across the receiver coil L_R. In a switched resonant half-bridge, the voltage impressed across L_R is v_C. So v_{MPP} is $0.5Q_Rv_{E(PK)}$, as derived in Eq. (3.11). Drawing the maximum available power $P_{L(MAX)}$' presupposes $v_{C(PK)}$ is $v_{C(OPT)}$ every cycle. However, as Figure 5-10 illustrates, $v_{C(PK)}$ grows from cycle to cycle between energy transfers. $v_{C(PK)}$ therefore deviates from $v_{C(OPT)}$, so actual drawn power P_L is lower than $P_{O(MAX)}$. As depicted in Figure 5-11, the difference between the drawn power $P_{L(i)}$ at the i-th cycle and $P_{O(MAX)}$ is defined as the nonlinear loss $P_{NL(i)}$, since the loss is due to the nonlinearity in the operation. As P_L' peaks parabolically at $v_{C(OPT)}$ [131], $P_{NL(i)}'$ grows quadratically with $v_{C(i)}$ deviations:

$$P_{NL(i)} = P_{O(MAX)}'\left(\frac{\Delta v_{C(i)}}{v_{C(OPT)}}\right)^2 = P_{O(MAX)}\left(\frac{v_{C(i)} - v_{C(OPT)}}{v_{C(OPT)}}\right)^2. \tag{5.13}$$

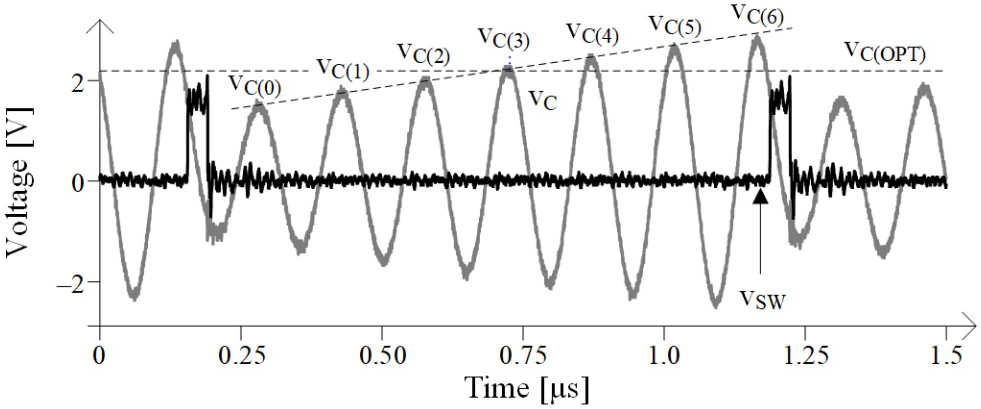

Figure 5-10. $v_{C(PK)}$ deviates from $v_{C(OPT)}$ in the switched resonant half-bridge skipping operation.

Here, $P_{O(MAX)}'$ is the maximum receiver power availed by v_E, R_E, R_R, and R_{SW}:

$$P_{O(MAX)}' = \frac{\left(0.5v_{E(PK)}\right)^2}{2\left(R_E + R_L + R_{SW}\right)} = \frac{\left(0.5v_{E(PK)}\right)^2}{2R_{ESR}}. \tag{5.14}$$

Note the reflected R_E in Eq. (5.14) varies with k_C. At lower k_C, the transmitter reflects less R_E on the receiver. As a result, R_{ESR} and $P_{O(MAX)}'$ also vary with k_C. The overall nonlinear loss P_{NL} is the average over N_S cycles:

$$P_{NL} = P_{NL(AVG)} = \frac{1}{N_S}\sum_{i=1}^{N_S} P_{NL(i)} = \frac{1}{N_S}\sum_{i=1}^{N_S}\left(P_{O(MAX)}' - P_{L(i)}\right). \tag{5.15}$$

As shown in Figure 5-11, P_{NL} is lowest when $v_{C(PK)}$'s average $v_{C(OPT)}$.

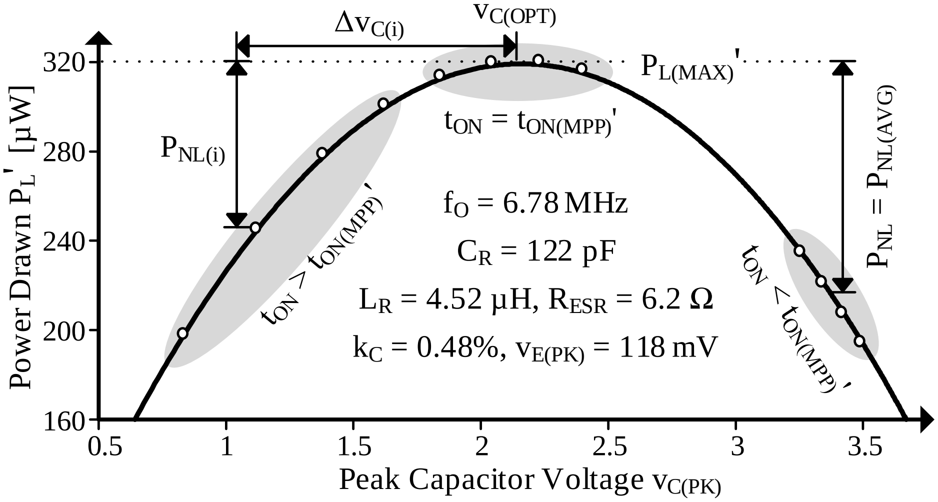

Figure 5-11. Drawn power and resulting nonlinear loss.

$P_{L(i)}$ is the difference between $P_{O(MAX)}'$ and $P_{NL(i)}$, so according to Eq. (5.14) and Eq. (5.15):

$$P_{L(i)} = P_{O(MAX)}' - P_{NL(i)} = P_{O(MAX)}'\left[1-\left(\frac{v_{C(i)}-v_{C(OPT)}}{v_{C(OPT)}}\right)^2\right]. \qquad (5.16)$$

As P_{NL}(i) is a function of the capacitor peak voltage $v_{C(PK)}$, to derive the P_{NL}, the first step is to calculate $v_{C(PK)}$ of each cycle. Between energy transfers, the LC tank collects across cycles the power L_R sources. The difference between consecutive cycles i – 1 and i's peak C_R energy, therefore, reflects energy the L_R sources across cycle i [131]:

$$P_{L(i)}t_O = E_{C(i)} - E_{C(i-1)} = 0.5C_R\left(v_{C(i)}{}^2 - v_{C(i-1)}{}^2\right). \qquad (5.17)$$

Combining Eq. (5.15) and Eq. (5.17) yields:

$$0.5C_R\left(v_{C(i+1)}-v_{C(i)}\right)\left(v_{C(i+1)}+v_{C(i)}\right) = P_{O(MAX)}'\left[\frac{v_{C(i)}\left(2v_{C(OPT)}-v_{C(i)}\right)}{v_{C(OPT)}{}^2}\right]t_O. \qquad (5.18)$$

Since the quality factor Q_R of the LC is normally much greater than one, oscillation growth from cycle to cycle is slow. Assuming $v_{C(i+1)} + v_{C(i)} \approx 2v_{C(i)}$, (5.18) can be simplify ed as:

$$v_{C(i+1)} - v_{C(i)} = \left(\frac{t_O P_{O(MAX)}'}{2C_R v_{C(OPT)}^2} \right) \left(2v_{C(OPT)} - v_{C(i)} \right). \tag{5.19}$$

Replacing $P_{O(MAX)}'$ and $v_{C(OPT)}$ with expressions in Eq. (5.14) and Eq. (3.11) yields

$$v_{C(i+1)} - v_{C(i)} = \left(\frac{\pi}{Q_R} \right) \left(2v_{C(OPT)} - v_{C(i)} \right). \tag{5.20}$$

Also, Eq. (5.20) can be re-written as:

$$v_{C(i+1)} - 2v_{C(OPT)} = \left(1 - \frac{\pi}{Q_R} \right) \left(v_{C(i)} - 2v_{C(OPT)} \right). \tag{5.21}$$

Assume $v_{C(PK)}$ is closest to $v_{C(OPT)}$ at the m-th cycle, using (5.21), $v_{C(PK)}$ at i-th cycle can be calculated as:

$$v_{C(i)} = 2v_{C(OPT)} - v_{C(OPT)} \left(1 - \frac{\pi}{Q_R} \right)^{i-m}. \tag{5.22}$$

To validate the $v_{C(i)}$ calculation, Figure 5-12 compares the simulated v_C growth from cycle to cycle with 150 mV $v_{E(PK)}$ a5 6.78 MHz against the iterative calculation in (5.22). The iterative calculation closely matches the simulation.

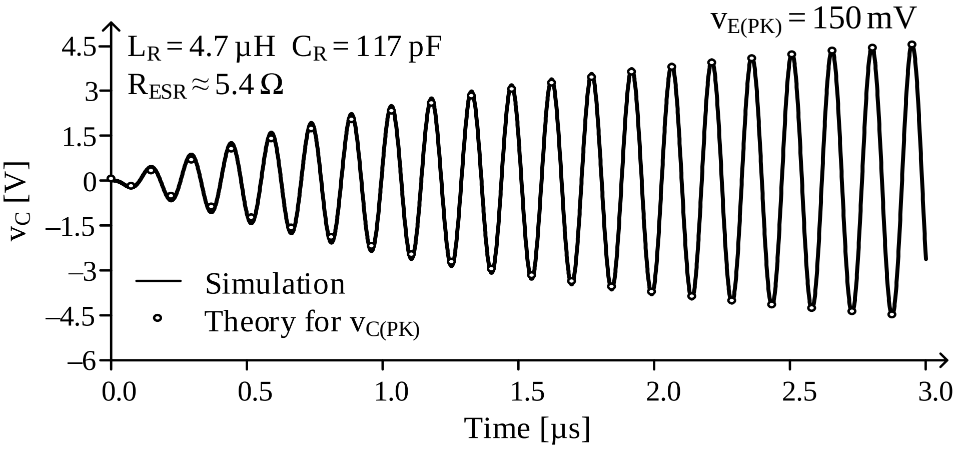

Figure 5-12. Simulated capacitor voltage across uncollected cycles.

Replacing $v_{C(i)}$ in Eq. (5.13) with Eq. (5.22), $P_{NL(i)}$ can be expressed as:

$$P_{NL(i)} = P_{O(MAX)}'\left(1-a^{i-m}\right)^2, \tag{5.23}$$

where

$$a = 1-\frac{\pi}{Q_R}. \tag{5.24}$$

Therefore,

$$\begin{aligned} P_{NL} &= \frac{1}{N_S}\sum_{i=1}^{N_S} P_{NL(i)} = \frac{P_{O(MAX)}'}{N_S}\sum_{i=1}^{N_S}\left(1-a^{i-m}\right)^2 \\ &= \frac{P_{O(MAX)}'}{N_S}\sum_{i=1}^{N_S}\left(1-2a^{i-m}+a^{2i-2m}\right) \\ &= P_{O(MAX)}'\left[1-\frac{2a^{-m}}{N_S}\left(\frac{1-a^{N_S}}{1-a}\right)+\frac{a^{-2m}}{N_S}\left(\frac{1-a^{2N_S}}{1-a^2}\right)\right] \end{aligned}. \tag{5.25}$$

The only unknown variable in Eq. (5.25) is m. So the next step is to determine the cycle m that v_C is closest to $v_{C(OPT)}$. As discussed before, at the local maximum point, intuitively,

$v_{C(PK)}$ centers around $v_{C(OPT)}$. Therefore, it is fair to assume the nonlinear loss of the first cycle approximately equals that of the last cycle:

$$P_{NL(1)} \approx P_{NL(N_S)}, \tag{5.26}$$

which gives:

$$P_{O(MAX)}'\left(1-a^{1-m}\right)^2 \approx P_{O(MAX)}'\left(1-a^{N_S-m}\right)^2. \tag{5.27}$$

This way, m is related to N_S. Since a is close to but smaller than one, (5.27) can be simplified as:

$$1-a^{1-m} \approx a^{N_S-m}-1. \tag{5.28}$$

So

$$a^{-m} \approx \frac{2}{a+a^{N_S}} \approx \frac{2}{1+a^{N_S}}. \tag{5.29}$$

Substituting a^{-m} in Eq. (5.25) with Eq. (5.29), P_{NL} at the local maximum point can be re-written as:

$$P_{NL(MPP)}' = P_{O(MAX)}'\left[1-\left(\frac{4a}{1-a^2}\right)\left(\frac{a^{-0.5N_S}-a^{0.5N_S}}{a^{-0.5N_S}+a^{0.5N_S}}\right)\left(\frac{1}{N_S}\right)\right]. \tag{5.30}$$

Alternatively, P_{NL} can be written as:

$$P_{NL(MPP)}' = P_{O(MAX)}'\left[1-\left(\frac{4a}{1-a^2}\right)\left(\frac{1-a^{f_O/f_X}}{1+a^{f_O/f_X}}\right)\left(\frac{f_X}{f_O}\right)\right]. \tag{5.31}$$

B. Charge Loss

The circuit also loses charge power as parasitic capacitances charge and discharge. This charge loss P_C is proportional to f_X:

$$P_C = v_{DD}q_Cf_X = v_{DD}^2k_{SW}C_{EQ}f_X\,. \tag{5.32}$$

where C_{EQ} is the total equivalent capacitance that charges and discharges in one switching cycle. k_{SW} is the soft-switching factor. Without t_{DT}, M_O hard-switches: burns power to charge v_{SW}'s parasitic capacitance C_{EQ}, so $k_{SW} = 1$. With t_{DT}, L_X's current charges C_{EQ} before M_O closes, so M_O partially soft-switches: closes with lower than v_B voltage drop. L_X's current also charges C_{EQ} above v_B before M_G closes, so M_G switches with higher charge loss. As a result, k_{SW} can be higher or lower than 1. The analysis assumes $k_{SW} = 1$. The accuracy of this assumption will be verified by simulations and measurements later. Output power P_O is the $P_{L(MAX)}$' that nonlinear and charge losses P_{NL} and P_C avail:

$$P_O = P_{O(MAX)}\,' - P_{NL} - P_C\,.\,. \tag{5.33}$$

For global MPP, $f_{X(MPP)}$ needs to minimize the total losses $P_{NL(MPP)}$' + P_C:

$$\frac{\delta P_{O(MPP)}\,'}{\delta f_X} = -\frac{\delta P_{NL(MPP)}\,'}{\delta f_X} - \left.\frac{\delta P_C}{\delta f_X}\right|_{f_{X(MPP)}} = 0\,. \tag{5.34}$$

Expanding Eq. (5.34) with expressions in Eq. (5.31) and Eq. (5.32) yields:

$$P_{O(MAX)}\,'\left(\frac{2a}{1+a}\right)\frac{\left(-\ln a\right)\left(a^{-0.5N_S} - a^{0.5N_S}\right)}{\left(a^{-0.5N_S} + a^{0.5N_S}\right)^2} = \frac{P_{C(f_O)}}{{N_S}^2}\,. \tag{5.35}$$

Again, since Q_R is normally much greater than one, a is close to one. Using Taylor expansion, the following terms in (37) can be approximated and simplified as:

$$a^{-0.5N_S} + a^{0.5N_S} \approx 2\,, \tag{5.36}$$

and

$$\frac{\left(a^{-0.5N_S} - a^{0.5N_S}\right)}{N_S} \approx 1 - a\ . \tag{5.37}$$

With the approximations, Eq. (5.35) can be simplified as:

$$P_{O(MAX)}'\left(\frac{2a}{1+a}\right)\frac{(-\ln a)\,N_S\,(1-a)}{4} \approx \frac{P_{C(f_O)}}{{N_S}^2}\,. \tag{5.38}$$

Again, use Taylor expansion to approximate the term in Eq. (5.38):

$$-\ln a = \ln\left[1+\left(\frac{1}{a}-1\right)\right] \approx \frac{1-a}{a}\,. \tag{5.39}$$

Solving Eq. (5.38) with the approximation in Eq. (5.39) yields the optimal number of cycles N_S between energy transfers:

$${N_S}^3 \approx \left(\frac{4P_{C(f_O)}}{P_{O(MAX)}'}\right)\left(\frac{Q_R}{\pi}\right)^2. \tag{5.40}$$

Therefore, the global optimal $f_{X(MPP)}$ can be obtained:

$$f_{X(MPP)} = f_O\left[\left(\frac{\pi}{2Q_R}\right)^2\left(\frac{P_{L(MAX)}'}{P_{C(f_O)}}\right)\right]^{1/3}. \tag{5.41}$$

where $P_{C(f_O)}$ is the charge loss when $f_X = f_O$. The global optimal $t_{ON(MPP)}$ is, therefore, $t_{ON(MPP)}'$ at $f_{X(MPP)}$:

$$t_{ON(MPP)} = t_{ON(MPP)}'\Big|_{f_X = f_{X(MPP)}} . \tag{5.42}$$

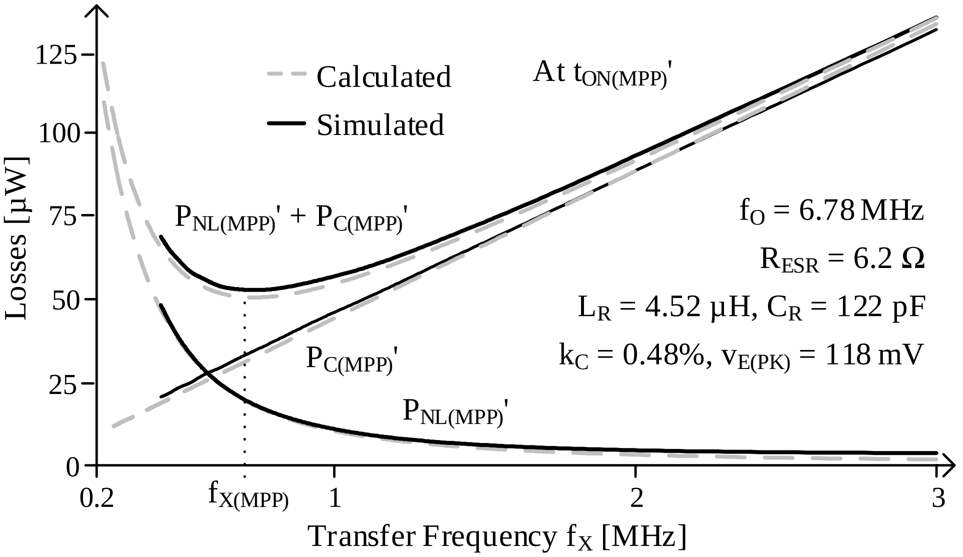

Figure 5-13. Losses and resulting optimal transfer frequency.

To validate the theory on $f_{X(MPP)}$, $P_{NL(MPP)}'$, and P_C, Figure 5-13 compares the simulated losses with the theory's prediction in (8) and (18). The theory accurately predicts the simulated P_{NL} and P_C with less than 5% error when f_X is 420 kHz–3MHz. Note that, unlike conduction and switching losses, P_{NL} is not lost as heat. Since the receiver coil L_R is so small and distant, drawn P_E is much lower than the power the transmitter can actually supply. So P_E cannot over-damp the transmitter under these conditions. P_{NL} is therefore power that the transmitter avails, but the receiver fails to collect.

5.2.3 Maximum Output Power

With the losses (P_{NL} and P_C) and MPP settings ($t_{OS(MPP)}$, $t_{ON(MPP)}$, $f_{X(MPP)}$) obtained in the previous two subsections, the output power is $P_{L(MAX)}'$ minus the losses at the MPP settings:

$$P_{O(MPP)} = P_{L(MAX)}' - P_{NL(MPP)} - P_{C(MPP)}. \tag{5.43}$$

Figure 5-14 compares the calculated, simulated, and measured P_O across f_X at 118 mV of $v_{E(PK)}$ and 6.2 Ω of R_{ESR}. As the number of half cycles skipped N_S rises (or f_X drops), $v_{C(PK)}$'s spread widens. This means, more and more half cycles deviate further away from the maximum power point P_{MPP0}. In other words, the sacrificial loss P_{NL} drops with f_X. Testing accuracy and measurement noise produce an error. With up to ±5 mV of resolution and noise errors, measured v_E is up to ±4% off, which means calculated and simulated projections are off by a corresponding amount. Figure 5-8 and Figure 5-14 show that measured data is within the projected error window. The hard-switching assumption in the calculations also contributes error. But like Figure 5-13 shows, calculations and simulations match, so this error is small. At the theory's predicted $f_{X(MPP)}$ of 700 kHz, the measured P_O is only 1% lower than the actual $P_{O(MPP)}$.

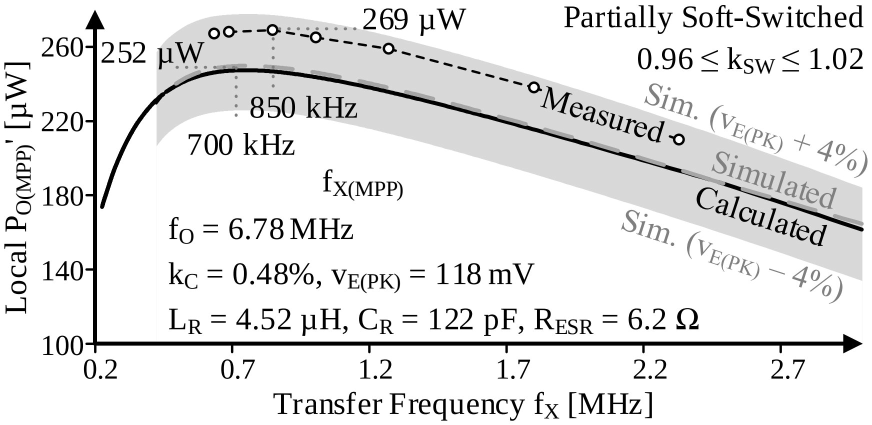

Figure 5-14. Optimized output power.

To evaluate P_O, the simulation monitors the average net current into v_B. P_L' can be obtained from L_R's voltage and current. The simulation estimates the ohmic loss P_R on R_{ESR} from the i_L waveform. P_L' minus P_O and P_R gives the charge loss P_C.

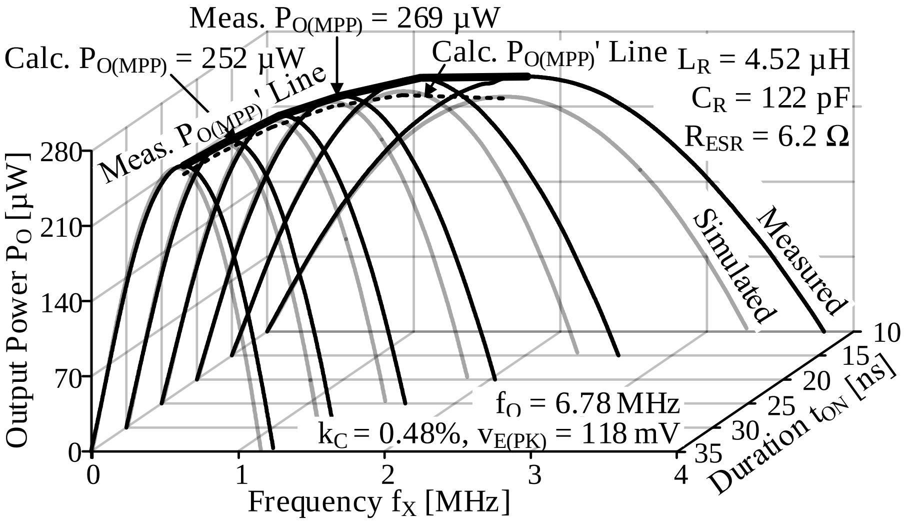

Figure 5-15. Variable space for output power.

Figure 5-15 plots the simulated and measured P_O over the variable space by sweeping t_{ON} and f_X with 5 ns and 53 kHz of resolution, respectively. The measured P_O maximizes at 269 µW when t_{ON} = 25 ns. The FPGA controller cannot respond within 5 ns, so 5 ns is the practical limit. Higher bandwidth is not necessary because, as Figure 5-15 shows, P_O is not very sensitive to t_{ON} near P_O's maximum power point: P_O varies 2% with ±5-ns variations in t_{ON}.

5.3 Measurements

5.3.1 Prototype

To validate the theory, the switched resonant half-bridge power receiver prototype in CHAPTER 4 is measured. The dead time logic in Figure 4-1 inserts delays to prevent M_G and M_O from turning on at the same time and shorting v_B to the ground. The receiver prototype uses an off-chip coil PA6512-AE from Coilcraft that measures 4.52 µH. The integrated resonant capacitor C_R is laser trimmed to 122 pF with ±1-pF accuracy. L_R and C_R resonate at 6.78 MHz.

The linear stage in Figure 4-10 adjusts the distance d_X between the coils from 13 mm to 38 mm, so k_C is 0.07%–1.13%. Although separation is 38 mm, the coils are 4.5 radial lengths apart (where radial lengths refers to the radii of the coils), which is as far apart as some of the best inductively coupled systems can output power, like in [12, 84, 122, 124]. This 38-mm (power) transmission distance is suitable for implanted biosensors like glucose and blood-pressure sensors, since such sensors are typically implanted underneath the skin [10], [132]. The corresponding R_C varies 0–1.9 Ω, so the total R_{ESR} varies 4.8–6.7 Ω. An FPGA controls t_{OS}, t_{ON} and f_X of the power receiver with 1.25 ns, 5 ns, and 53 kHz of resolution, respectively.

Figure 5-16 shows the measured waveforms of v_C, i_L, and v_R at 118 mV of induced v_E. The receiver transfers power to v_B for 25 ns every 8 cycles.

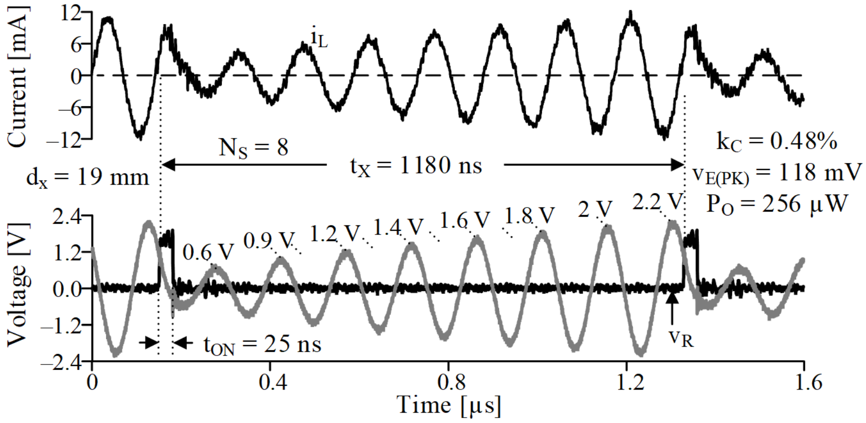

Figure 5-16. Measured waveforms at MPP.

5.3.2 Optimal Settings

Figure 5-17 compares the calculated, simulated and measured $t_{ON(MPP)}$ and $N_{S(MPP)}$. The calculated and simulated $t_{ON(MPP)}$ and $f_{X(MPP)}$ are rounded up to the closest 5 ns or 53 kHz to match the measurement resolution. The simulated and measured $t_{ON(MPP)}$ are often 5–10 ns higher than the theory's prediction. The simulated and measured $N_{S(MPP)}$ are often higher as well.

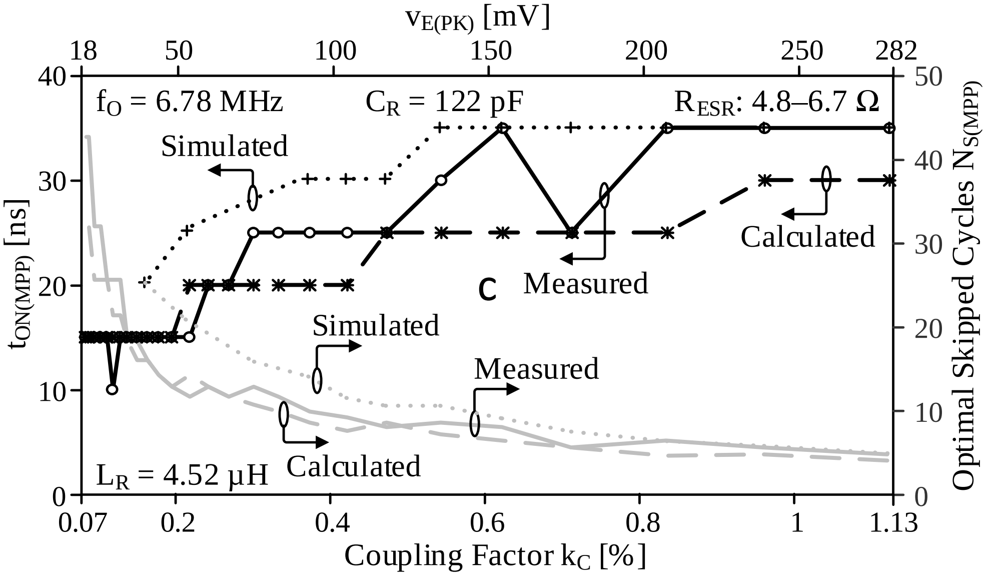

Figure 5-17. Optimal duration and number of cycles between transfers.

5.3.3 MPP Error

Figure 5-18 compares the measured P_O at the theory's predicted MPP settings with the actual $P_{O(MPP)}$. The MPP error denotes the percentage difference between P_O at the predicted MPP setting and the actual $P_{O(MPP)}$. The circuit outputs 344 μW halfway across the coupling k_C range tested, which is sufficient for microsensor applications such as blood-pressure and glucose sensors [10] and [132].

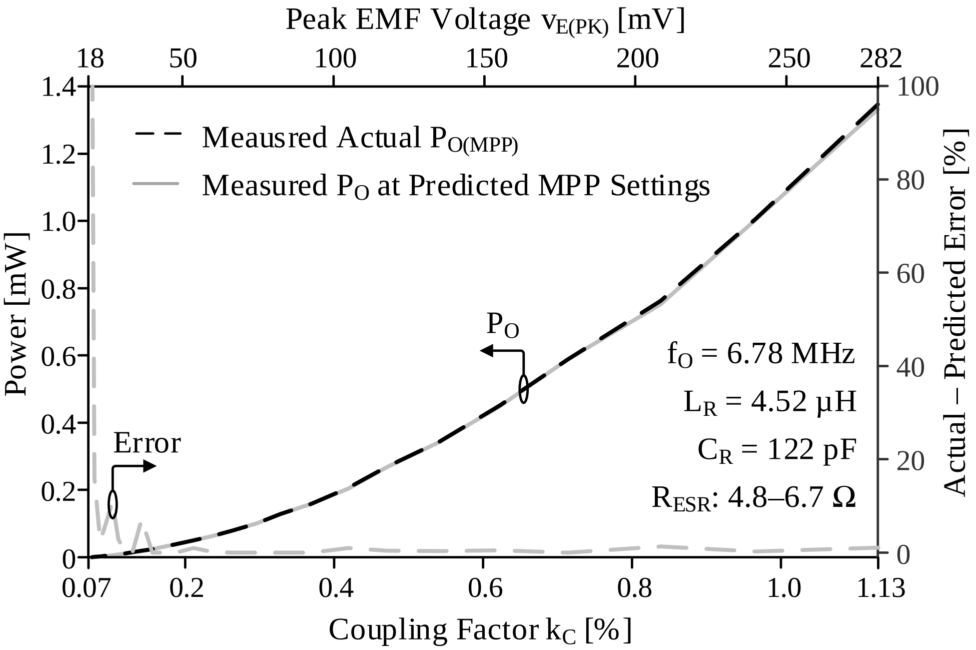

Figure 5-18. P_O at the predicted MPP setting and the actual MPP setting.

Table II summarizes and compares the calculated MPP settings and power with simulation and measurement when $k_C > 0.15\%$. The theory's predicted $t_{ON(MPP)}$ is 17–30% lower than the simulation and 2–24% lower than the measurement, while the predicted $f_{X(MPP)}$ is 21–66% higher than the simulation and 2–32% higher than the measurement. Testing accuracy and noise produces an error in v_E that, along with the approximations in (35) and (38), offsets projected $f_{X(MPP)}$, and by translation, $t_{ON(MPP)}$ from their actual values by up to –30% and +66%. P_O, however, is still within 1.3% of its maximum power point $P_{O(MPP)}$ because P_O (in Figure 5-15) is fairly insensitive to settings near $P_{O(MPP)}$. These inaccuracies in $f_{X(MPP)}$ and $t_{ON(MPP)}$ are therefore acceptable. In practice, rather than the accuracy of the MPP settings, it is more important that P_O at the predicted setting is as close to the actual $P_{O(MPP)}$ as possible, so the MPP error is low. The MPP error is within 3.8% for simulation and within 1.3% for measurement. Since the series switched resonant half-bridge outputs as much or more power than other receivers, the $P_{O(MPP)}$ theorized here is also the highest $P_{O(MPP)}$ a receiver can output.

Table 5-1. MPP Settings Summary

Parameter*	**Calculated**	**Simulated**		**Measured**	
		Value	Error	Value	Error
$t_{OS(MPP)}$	0	0	0	0	0
$t_{ON(MPP)}$	16–29 ns	15–35 ns	–(17–30%)	15–35 ns	–(2–24%)
$f_{X(MPP)}$	0.44–1.7 MHz	0.26–1.4 MHz	21–66%	0.43–1.4 MHz	2–32%
Actual $P_{O(MPP)}$		13–1400 μW		24–1350 μW	
Predicted $P_{O(MPP)}$		13–1380 μW		24–1330 μW	
MPP Error		< 3.8%		< 1.3%	

*Parameters are obtained for 0.15–1.13% of k_C.

To sum up, this chapter explores and theorizes the MPP operation of the switched resonant half-bridge power receiver. The theory predicts the optimal phase, duration, and frequency of energy transfer in a closed form fashion. To prove the theory, a power receiver prototype is fabricated in 0.18 μm CMOS technology. Measurements show that at the theory's predicted settings, the receiver outputs more than 98.7% of the actual maximum power when the coupling is 0.15%–1.13%.

5.4 Discussions

The maximum power point of the switched resonant bridge has been explored in other literature as well. [123], [118, 121, 124] explored maximum end-to-end efficiency (MPE) for strongly coupled switched resonant bridges and half bridges. When weakly coupled, the receiver barely loads the transmitter [130], so the maximum power point (MPP) is also the MPE. Theorized MPEs in [118, 121, 124] fix f_X at $2f_O$, which is not optimal because switching (charge) losses are not minimized this way [131], and the MPE is not global.

Although [123] varies f_X, it does not account for these switching losses. Plus, [123] linearizes the operation of the circuit, which means [123] also discounts the nonlinear effects of the multi-cycle switching system. This thoery shows that both losses are significant when weakly coupled and shows how these losses can be minimized. More generally, the theory proposed here adjusts all variables and accounts for all losses to ensure the MPP is global and the highest possible.

The developed theory facilitates the implementation of a maximum power point tracking (MPPT). Similar to deriving $t_{ON(MPP)}'$ in (5.11), the $f_{X(MPP)}'$ at given t_{ON} that maximizes the local P_O can be obtained as:

$$v_{R(PK)}^{(f_O)} = \left(\frac{2}{\pi}\right)\left(\frac{f_{X(MPP)}'}{f_O}\right) v_B \sin\left[\pi\left(\frac{t_{ON}}{t_O}\right)\right] = \frac{v_{E(PK)}}{2}. \qquad (5.44)$$

Equation (5.44) is very interesting, as it shows the local optimal $f_{X(MPP)}'$ is proportional to the coupled voltage v_E. Thus, the local MPP can be monitored by tracking v_E with f_X. Possible MPPT schemes will be discussed in CHAPTER 7.

CHAPTER 6. SYNCHRONIZING CONTROLLER

Although the switched resonant half-bridge power receiver proposed in CHAPTER 4 can output high power across a wide coupling range, its synchronized control remains a challenge. As Figure 4-14 shows, the prototype built in CHAPTER 4 uses an FPGA to synchronize the receiver operation with the transmitter. The wired connection between the transmitter and the receiver defeats the purpose of wireless power transfer. That prototype is for functionality and performance verification of the power stage only. To complete the system, the receiver needs to be self-synchronized. This chapter presents a self-synchronized switched resonant half-bridge wireless charger that adjusts energy transfer frequency for maximum power point (MPP). An integrated high-voltage-sensing synchronizer allows the charger to operate beyond the CMOS breakdown voltage and therefore extends its workable coupling range. A prototype wireless charger is fabricated with 180 nm technology. The measured prototype outputs up to 89% of the available power across 0.067%~7.9% coupling range. The output power (in percentage of available power) and coupling range are 1.3× and 13× higher than the comparable state of the arts.

6.1 Self-Synchronized Switched Resonant Half-Bridge

6.1.1 System Operation

The switched resonant half-bridge in Figure 6-1 uses a resonant tank L_R–C_R to boost current and power from v_E. The L_R and C_R are tuned to v_E's frequency f_O, so v_E constantly sources power into the LC tank. R_E represents the coupled resistance from the transmitter, while R_R is the ESR of L_R at f_O.

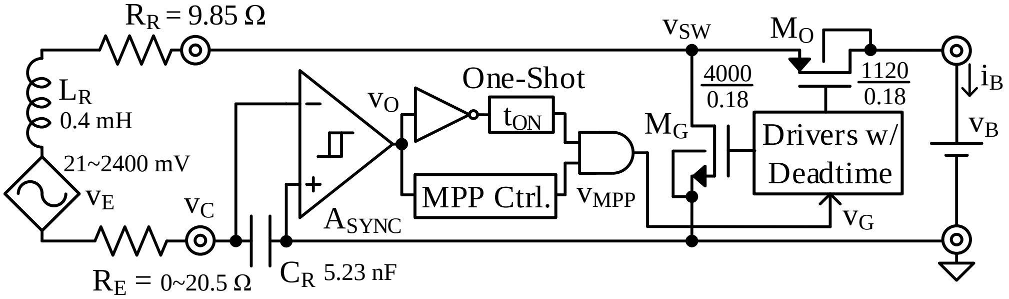

Figure 6-1. Switched resonant half-bridge wireless charger.

To transfer energy, the power stage alternately switches between two modes: receiving energy from v_E and transfer received energy to v_B. The ground switch M_G closes for most of the cycle t_X, so L_R–C_R receives and stores energy from v_E. So v_C's oscillation grows. Then, M_G opens and the output switch S_O closes for t_{ON}, the energy accumulated is transferred to the battery v_B. The deadtime logic inserts around 1 ns delay so M_G or M_O only turns on when the other switch is completely off. This prevents both switches from turning on at the same time and discharge the battery. The ground switch M_G and the output switch M_O are 4000 µm and 1120 µm wide, respectively. The sizes are optimized in the same way as described in Sub-section 4.2 to minimize the losses for 300 µW, which is the most probable power level for targeted glucose and blood-pressure sensing applications [9, 10].

For MPP, the energy transfer needs to be synchronized with the oscillation. For this, the synchronizer A_{SYNC} in Figure 6-2 detects the negative zero crossings of v_C. Once a crossing is detected, a one-shot circuit triggers a fixed pulse t_{ON}, which is gated by the MPP controller's output v_{MPP}, as Figure 6-2 shows. The charger only transfers power to battery when v_{MPP} is high. This way, the MPP controller adjusts the energy transfer frequency f_X by the number of cycles between energy transfers.

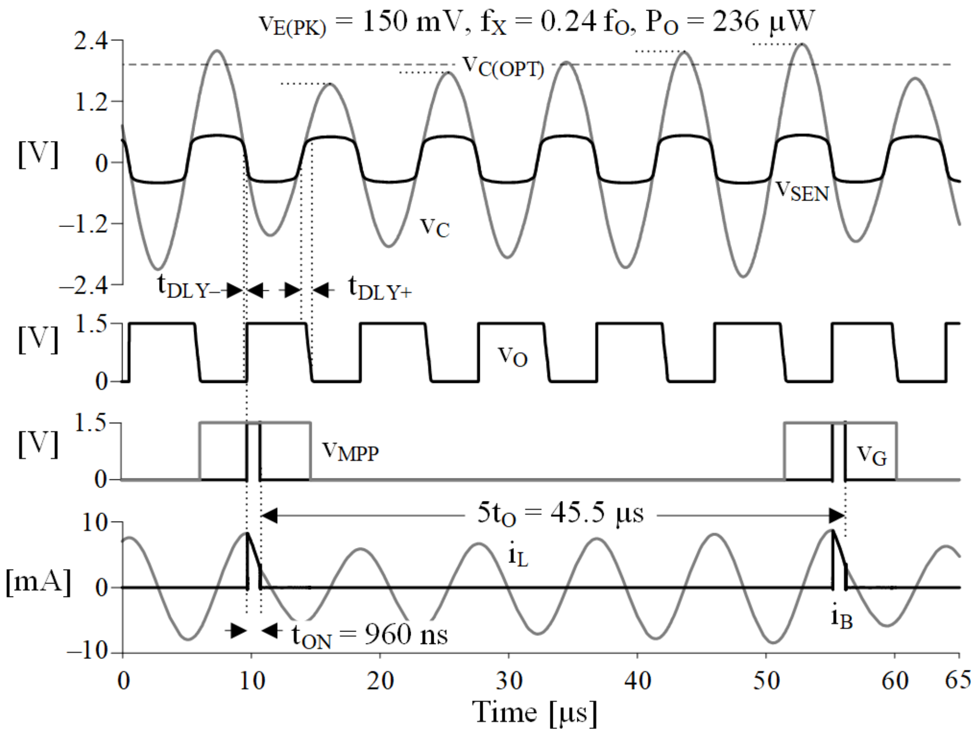

Figure 6-2. Simulated wireless charger waveforms at 150 mV $v_{E(PK)}$.

6.1.2 Maximum Power Point

The goal of the inductively coupled wireless charger design is to maximize its output power to charge up the battery as fast as possible. For MPP, the receiver needs to drain just enough energy such that the averaged $v_{C(PK)}$ over cycles is at its optimal level $v_{C(OPT)}$ [77], as the v_C waveform in Figure 6-2 shows, where

$$v_{C(OPT)} = \left(\frac{\pi L_R f_O}{R_E + R_R}\right) v_{E(PK)}. \tag{6.1}$$

To maintain the $v_{C(PK)}$ around $v_{C(OPT)}$, the energy transfer duration t_{ON} and energy transfer frequency f_X can be adjusted. Although adjusting both t_{ON} and f_X gives the highest power, it complicates the controller design. Fortunately, near MPP, P_O is not sensitive to t_{ON}

variation. In [99], $P_{O(MPP)}$ is lowered by less than 1.3% even if t_{ON} is 24% off its optimal value. Adjusting f_X alone gives about the same $P_{O(MPP)}$ while simplifying control.

According to the MPP theory developed in CHAPTER 5, the receiver power is maximum when the offset time t_{OS} is zero. However, in this design, as the energy transfer starts after (rather than during) i_L peaks, it is delayed by $0.5t_{ON}$. So $t_{OS} = 0.5\ t_{ON}$. Luckily, the fixed t_{OS} delay can be compensated by tuning C_R, as discussed in Sub-section 4.2.

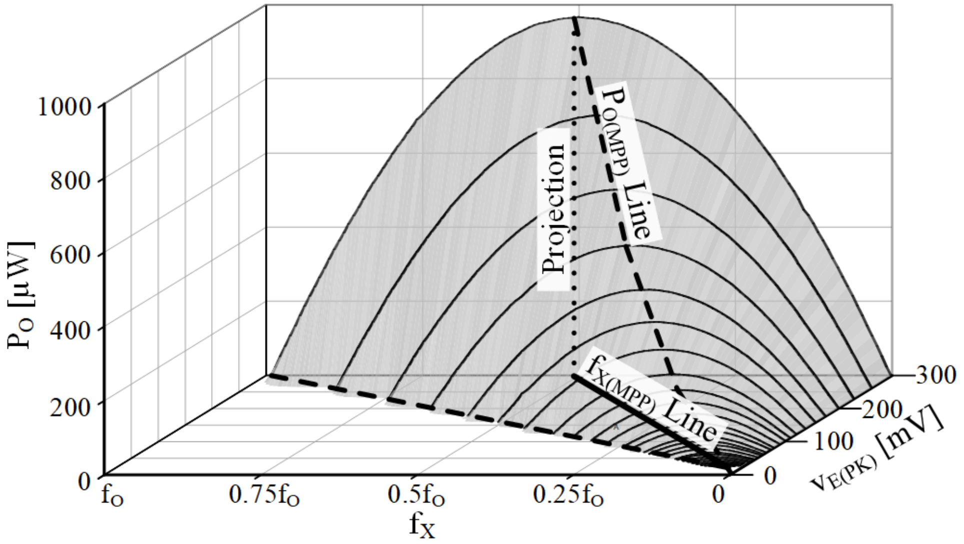

Figure 6-3. Measured P_O across $v_{E(PK)}$ and f_X.

Figure 6-3 shows how P_O varies across f_X at different $v_{E(PK)}$. At very low f_X, the battery draws little power from the LC, so the energy in the LC builds up high. As a result, v_C grows beyond $v_{C(OPT)}$ so P_O is low. Similarly, at high f_X, v_C stays below $v_{C(OPT)}$, so P_O is low too. P_O maximizes at $f_{X(MPP)}$. The MPP theory in [99] predicts that $f_{X(MPP)}$ grows proportionally with $v_{E(PK)}$:

$$f_{X(MPP)} = \left(\frac{\pi}{4}\right)\left(\frac{v_{E(PK)}}{v_B}\right) \Big/ \sin\left[\left(\frac{t_{ON}}{t_O}\right)\pi\right] \propto v_{E(PK)}. \tag{6.2}$$

6.2 *Circuit Implementation*

6.2.1 Synchronizing Comparator

For MPP, the synchronizer needs to synchronize the energy transfer with i_L's peak [99]. Sensing i_L directly is difficult, because i_L is low in milliamperes and adding sensing resistance significantly lowers the available power from the receiver coil. The other option is to sense v_C, as i_L peaks when v_C crosses zero. However, sensing v_C is also challenging, as v_C swings between positive and negative, and its magnitude can exceed the circuit's breakdown.

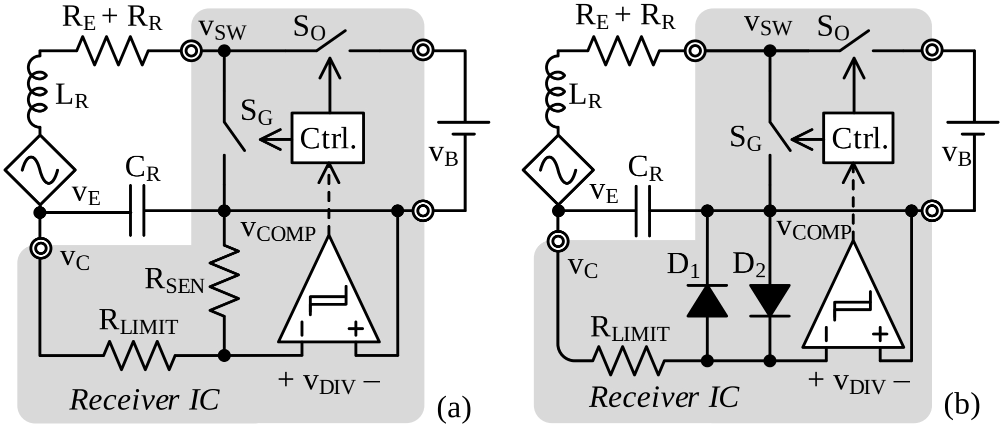

Figure 6-4. High voltage sensing with (a) resistive voltage divider and (b) variable-ratio voltage divider.

To protect the sensing circuit from breakdown, a voltage divider first divides and lowers v_C. Although a resistive ladder in Figure 6-4(a) can work as a voltage divider, its dividing ratio is fixed. As the coupling factor k_C varies for orders of magnitude in practical applications, v_{SEN} scales proportionally. As a result, v_{SEN} is too high for breakdown at high k_C, but too low for sensing at low k_C. To reduce the coupling sensitivity, the diode-clamped voltage divider in Figure 6-4(b) divides the voltage with a variable ratio. The circuit is composed of a pair of oppositely connected diodes D_1 and D_2 and a current limiting resistor R_{LIMIT}. When v_C's amplitude is within a diode voltage v_D, neither D_1 nor D_2 conducts, so

v_{DIV} follows v_C. As v_C's amplitude grows beyond v_D, either D_1 or D_2 conducts current and clamps v_{DIV} at $\pm v_D$, as Figure 6-2 shows. This way, the dividing ratio is low (< 1) at high v_C, but high (= 1) at low v_C.

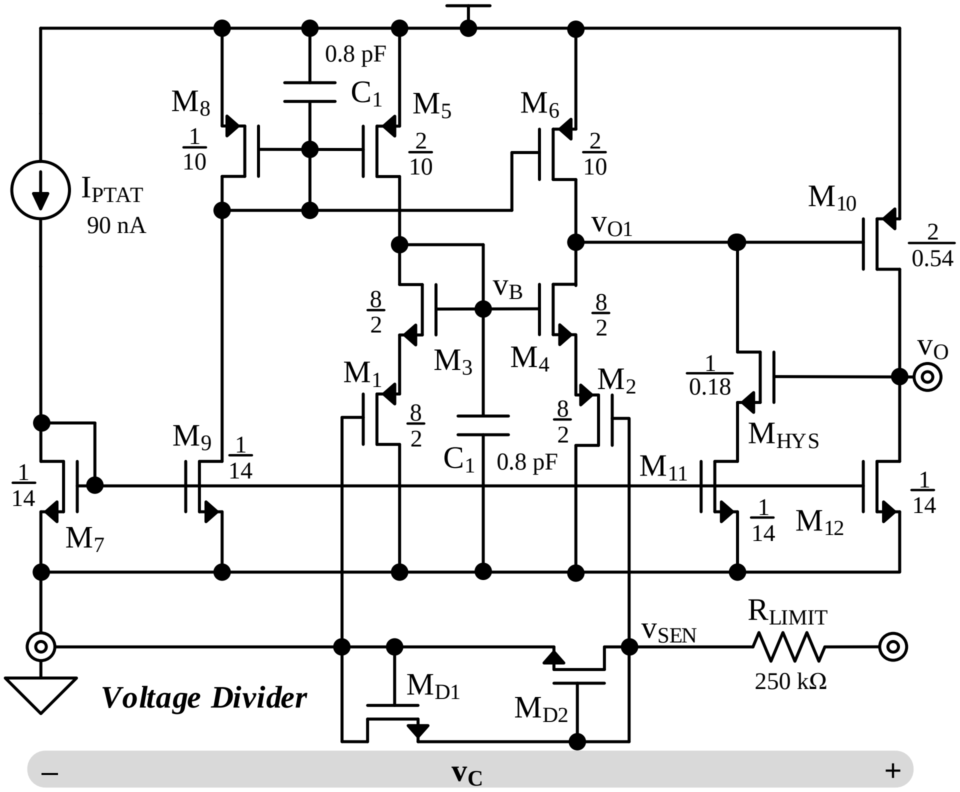
* NMOS bulk connected to GND. PMOS bulk connected to source

0.8 pF
C1
M8
1/10
M5
2/10
M6
2/10
IPTAT
90 nA
M10
2/0.54
vO1
vB
8/2
8/2
M3
M4
M1
M2
8/2
8/2
vO
1/0.18
MHYS
C1
0.8 pF
M9
1/14
1/14
M7
M11
1/14
M12
1/14
vSEN
RLIMIT
250 kΩ
MD1
MD2
Voltage Divider
–
vC
+

Figure 6-5. Synchronizer circuit with voltage divider.

The diodes D_1 and D_2 are implemented using two diode-connected N-type MOSFET, as shown in Figure 6-5. In measurement, the coupling k_C grows from 0.067% to 7.9%, so v_C varies 36× from 0.56 V to 20 V. However, as Figure 6-6 shows, the divided voltage v_{SEN} varies less than 2.7× in simulation due to the M_1 and M_2's square root voltage suppression.

A comparator in Figure 6-5 compares v_{SEN} with the ground to detect v_C's zero crossings and synchronizes the energy transfer. The comparator needs to (i) take negative input as v_{DIV} swings from $-v_D$ to $+v_D$, and (ii) minimizes the negative output delay t_{DLY-} for MPP [99]. Minimizing t_{DLY-} aligns energy transfer with i_L's peak. The aligned operation keeps i_L and v_E in phase, so the drawn power is maximum [99]. For (i), a PMOS pair, M_1 and M_2, are used. M_1's gate is grounded which generates a bias voltage v_B for M_4's pull-up path. Above-zero v_{DIV} crushes M_4's v_{GS}, so M_6 pulls v_{O1} up slowly with fixed 180 nA. As v_{DIV} drops below zero, M_2's current grows quadratically with the voltage drop and pulls v_{O1} down quickly. Plus, the bodies of all PMOS' in Figure 6-5 are connected to their respective sources. As v_{DIV} drops below zero, M_2's source and body follow, preventing the circuit from breakdown. For (ii), a secondary common-source stage M_{10} expediates v_O's pulling-up as v_{O1} rises. Combining that v_{O1} pulls down fast and v_O pulls up fast, the measured t_{DLY-} (120 ns ~ 180 ns) is much shorter than t_{DLY+} (1 μs ~ 1.8 μs), as Figure 6-2 shows.

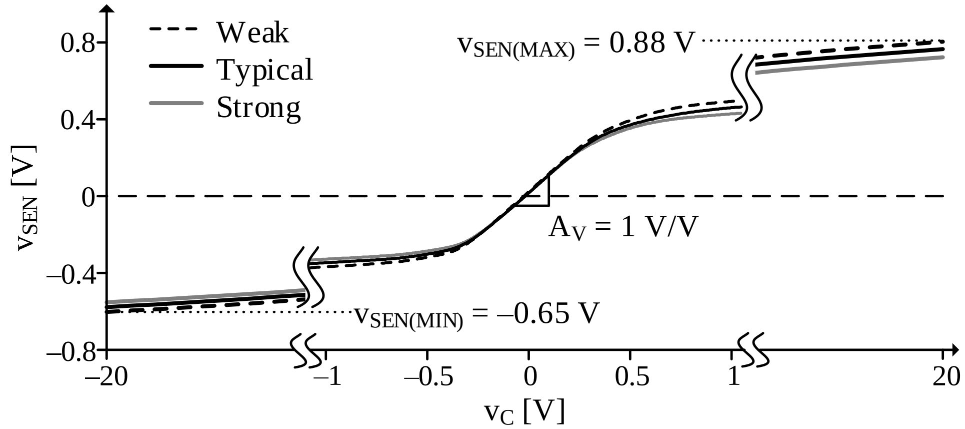

Figure 6-6. Simulated output curve of the voltage divider.

The voltage divider induces loss as the R_{LIMIT} steals and burns a fraction of i_L. At high v_C, ignoring the voltage drop on the diodes, the fractional loss that parallel R_{LIMIT} induces is equivalent to a series resistance of 0.3Ω [133], which lowers $P_{O(MPP)}$ by 3%. At low v_C, as the diodes voltage drop lowers the current across R_{LIMIT} more, R_{LIMIT}'s loss is less than 3%.

6.2.2 Current Reference

A PTAT current source circuit in Figure 6-7 provides a current bias to the synchronizing comparator discussed above. The synchronizing comparator is slower at high temperature, due to the reduced g_m of the transistors. The PTAT bias current reduces the t_{DLY-} variation with temperature. High bias current compensates for the slower circuit at high temperatures and vice versa.

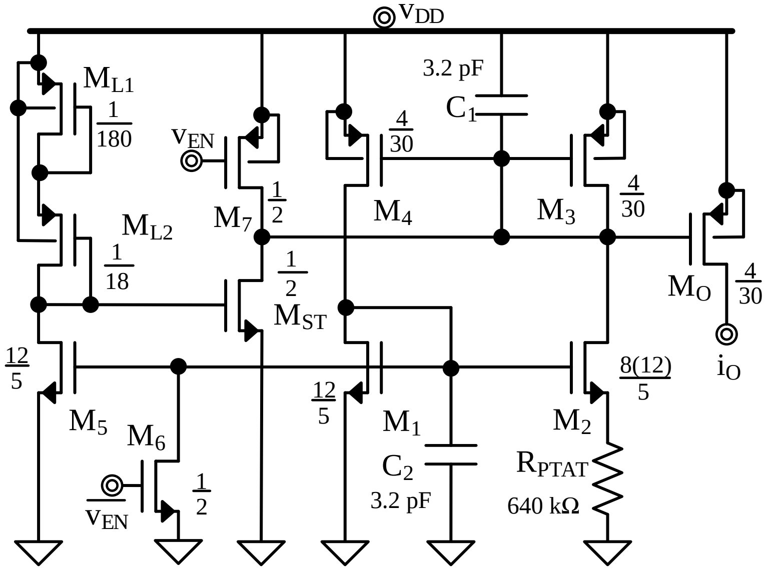
vDD
ML1
1/180
vEN
M7
1/2
4/30
3.2 pF
C1
M4
M3
4/30
ML2
1/18
1/2
MST
MO
4/30
iO
12/5
M5
M6
vEN
1/2
12/5
M1
C2
3.2 pF
M2
8(12)/5
RPTAT
640 kΩ

Figure 6-7. PTAT current source.

6.2.3 *MPP Control*

The MPP controller in Figure 6-8 is implemented on an FPGA for testing flexibility. The MPP controller controls which cycle to transfer energy to the battery by gating some of the pulses to the driver, as Figure 6-2 shows. This way, by controlling the number of cycles between energy transfer, the MPP controller controls the averaged energy transfer frequency f_X:

$$\overline{f_X} = \frac{1}{N_S} f_O, \qquad (6.3)$$

where N_S is the number of cycles between energy transfers.

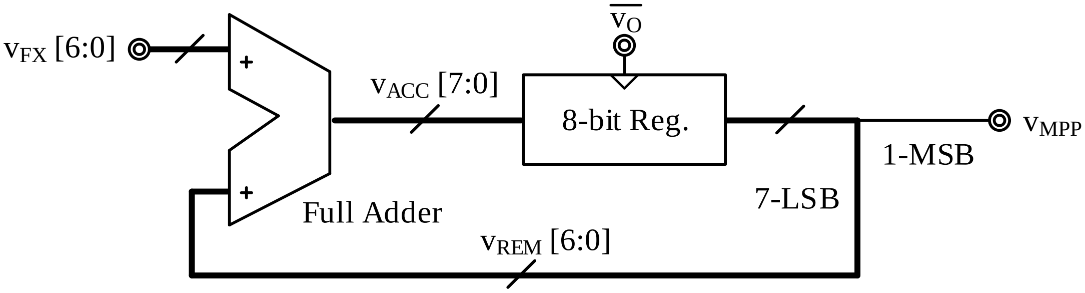

Figure 6-8. 6-bit digital delta sigma skip control.

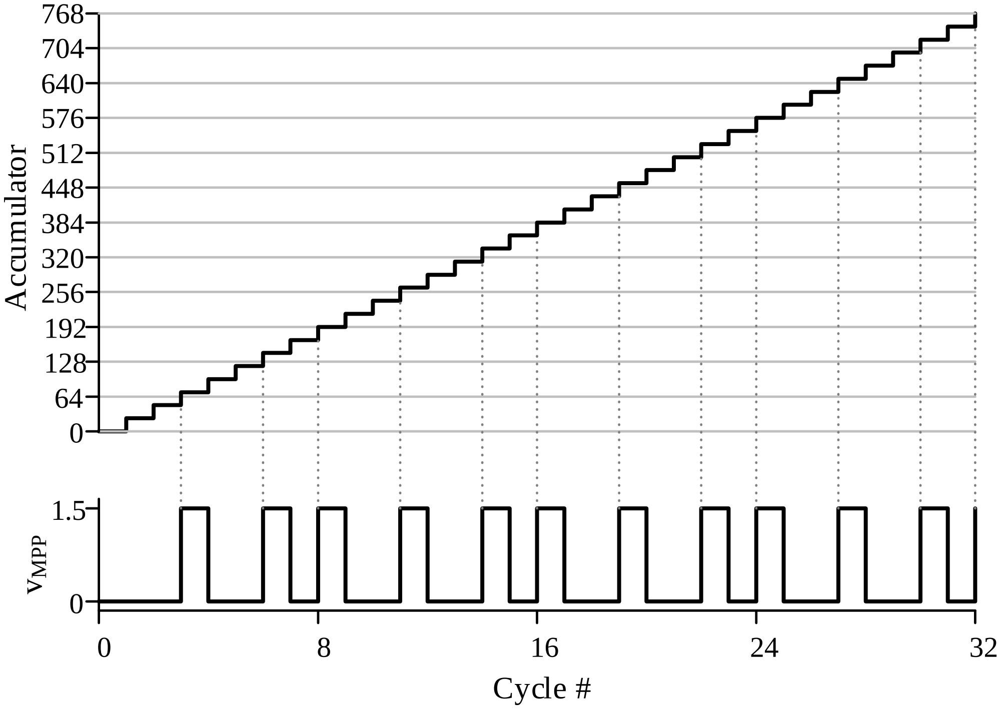

Figure 6-9. Operation of the DSM MPP controller.

The MPP controller is implemented with a 7-bit-input, 1-bit-output digital-to-digital delta-sigma modulator (DSM) frequently found in fractional-N PLL designs [134, 135], as shown in Figure 6-8. Figure 6-9 illustrates the operation of the DSM MPP controller. The full adder and 8-bit registers add v_{FX} to the accumulator. Once the accumulator reaches multiples of the full scale or 128 in this case, the MSB of the 8-bit registers overflows, which pushes v_{MPP} high and enables an energy transfer. The 7-bit LSB of the 8-bit registers rolls over for the next cycle's accumulation. The accumulator self-adds v_{FX} every cycle and overflows once it reaches 128, the averaged energy transfer frequency is:

$$f_X = \frac{v_{FX}}{128} f_O , \tag{6.4}$$

where v_{FX} can be configured from 1 to 127. So the resolution of f_X adjustment is $f_O/128$ or 859 Hz.

6.3 Measurements

6.3.1 Prototype

To demonstrate the charger's functionality and performance, a prototype is built with 180-nm CMOS technology. The charger IC, as shown in Figure 6-10, integrates the power stage (M_G, M_O, and the driver) and the synchronizer (I_{PTAT}, A_{COMP}, V_{DIV}) while occupying only 220 µm × 381 µm of silicon area.

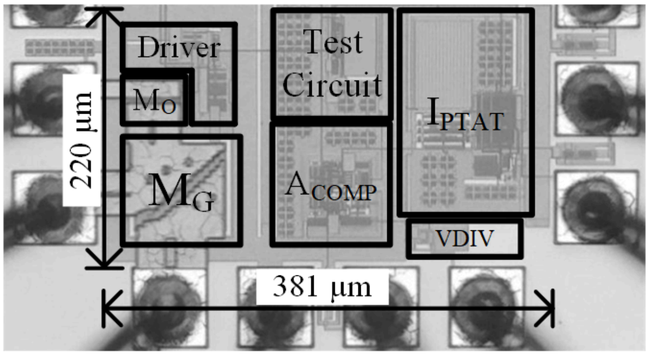

Figure 6-10. Photos of the wireless charger IC.

The MPP control and one-shot circuit in Figure 6-1 are implemented on an FPGA for testing flexibility. The receiver PCB and the FPGA are connected using the GPIO port, as shown in Figure 6-11. The wireless charger uses the 0.4 mH Coilcraft 4513TC as the receiver coil. The linear stage in Figure 6-12 adjusts the distance between the wireless charger and the source from 0 to 38 mm, which is up to 3.2 × of the transmitter/receiver coil dimension. As a result, the coupled open-circuit voltage v_E on the receiver coil ranges from 24 mV to 2.8 V. The transmitter couples up to 20.5 Ω back on the receiver coil.

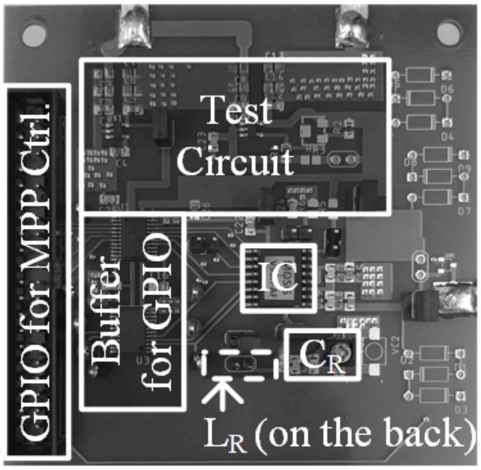
GPIO for MPP Ctrl.
Test Circuit
Buffer for GPIO
IC
C_R
L_R (on the back)

Figure 6-11. Photos of the wireless charger PCB.

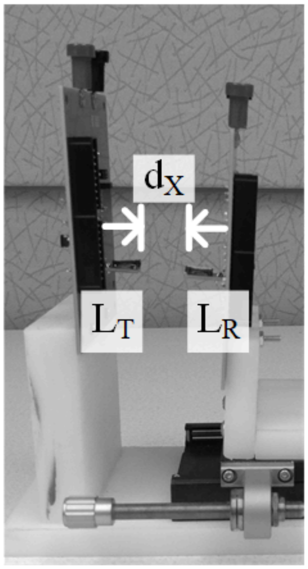

Figure 6-12. Linear stage that controls the distance between the transmitter and receiver coils.

Figure 6-13 shows the measurement setup. The output power P_O is measured by monitoring the average output current and the battery voltage. The amplitude of the coupled voltage v_E is measured by open circuiting the power receiver. The resonant capacitor is adjusted to compensate for the non-zero t_{OS}, such that P_O is maximum.

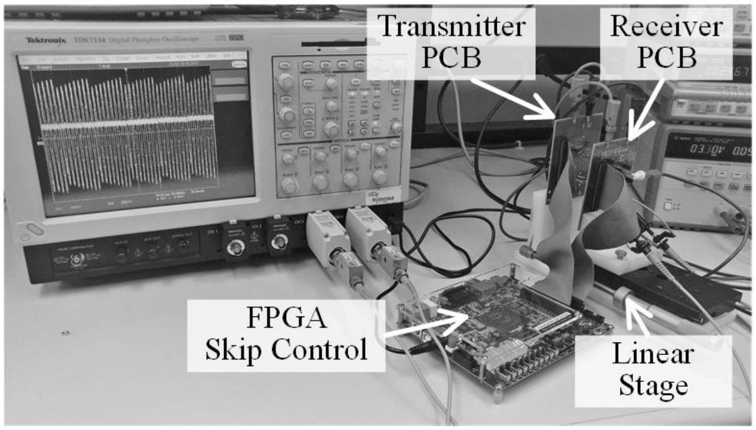

Figure 6-13. Measurement setup.

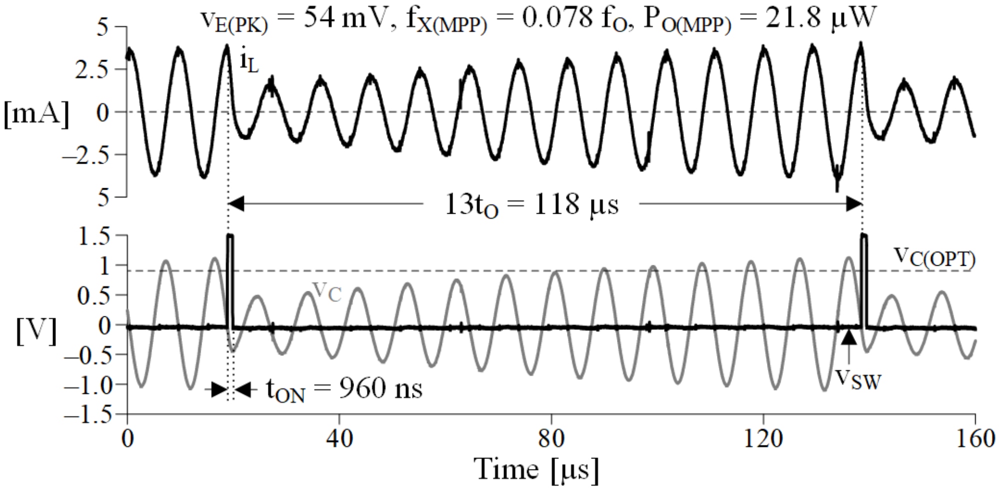

Figure 6-14. Measured MPP receiver waveforms when $k_C = 0.15\%$.

Figure 6-14 and Figure 6-15 show the measured v_{SW}, v_C and i_L waveforms at MPP when the receiver is 28 mm and 10 mm away from the power source. The couplings are 0.15% and 1.1%, respectively. At 0.15% coupling, the frequency control word v_{FX} is set to 10. So according to Eq. (6.4) and Eq. (6.3), the wireless charger on average skips 12.8 cycles between energy transfer for MPP. In other words, $f_{X(MPP)} = 0.078\ f_O$. At 1.1% coupling, the frequency control word v_{FX} is set to 86, so wireless charger on average transfers energy every 1.5 cycles. To achieve the fractional number of cycles, the wireless charger transfers energy alternatively every one or two cycles. So $f_{X(MPP)} = 0.67\ f_O$.

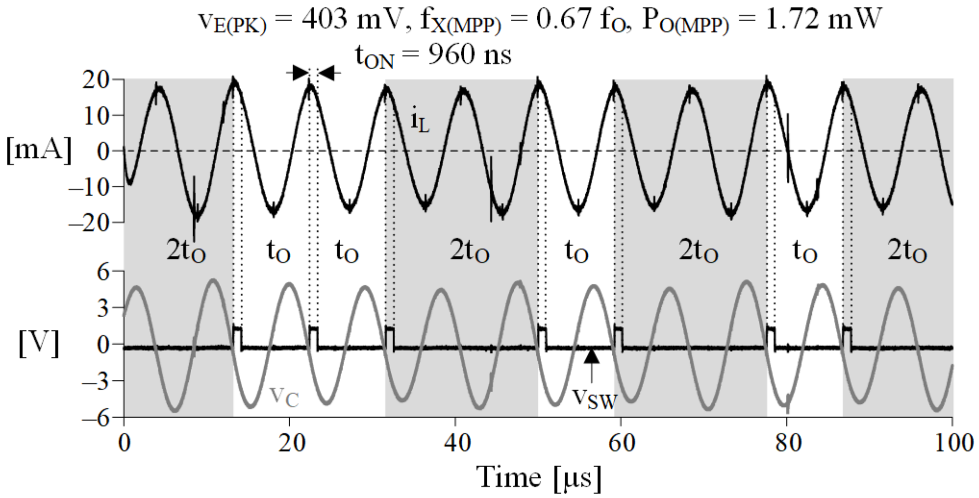

Figure 6-15. Measured MPP receiver waveforms when $k_C = 1.1\%$.

6.3.2 Charge Profile & Ideality Index

To evaluate the charger's performance, a charging test is performed that charges up a 1.1 µF capacitor C_O from 1 V to 1.8 V when the receiver is 13 mm, 18 mm, 23 mm, and 28 mm away from the power source. At the above distances, the receiver fully charges C_O in 3.6 ms, 7.9 ms, 20 ms, and 63 ms, respectively, as shown in Figure 6-16. The corresponding charging currents are 3.2 µA, 9.9 µA, 250 µA, 500 µA, respectively.

The maximum output power $P_{O(MPP)}$ is the key performance of the wireless charger. However, different wireless chargers' $P_{O(MPP)}$ is not comparable, as $P_{O(MPP)}$ scales with the transmitter's power and coupling. To assess the relative performance of the wireless charger, $P_{O(MPP)}$ needs to be normalized. Maximum available power $P_{O(MAX)}$ defines the highest power the receiver can possibly draw from the transmitter at the given coupling:

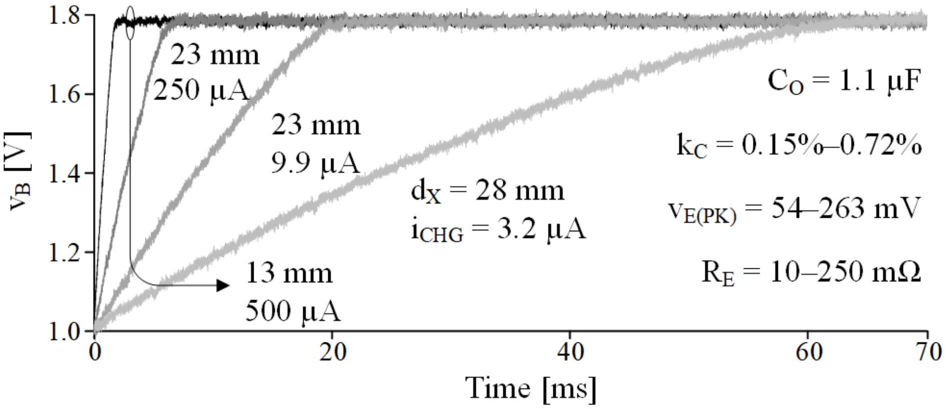

Figure 6-16. Measured charging waveforms at 13~28 mm distance.

$$P_{O(MAX)} = \left(\frac{0.5v_{E(PK)}}{\sqrt{2}}\right)^2 \left(\frac{1}{R_R + R_E}\right). \tag{6.5}$$

The ideality factor η_I references $P_{O(MPP)}$ to $P_{O(MAX)}$ and normalizes $P_{O(MPP)}$ with non-receiver variables:

$$\eta_I = \frac{P_{O(MPP)}}{P_{O(MAX)}}. \tag{6.6}$$

Figure 6-17 shows the measured η_I when d_X ranges from 0–38 mm. Ideality η_I is high (> 60%) at 7 – 27 mm. Past 27 mm, η_I starts to drop gradually to zero. This is because, as the power source separates further from the wireless charger, it couples less v_E on the receiving coil and, according to (2), the wireless charger skips more cycles between energy transfer for MPP. As a result, each cycle's $v_{C(PK)}$ deviates further from $v_{C(OPT)}$, causing a non-linear loss P_{NL} [99]. As deviation grows, P_{NL} increases and lowers η_I.

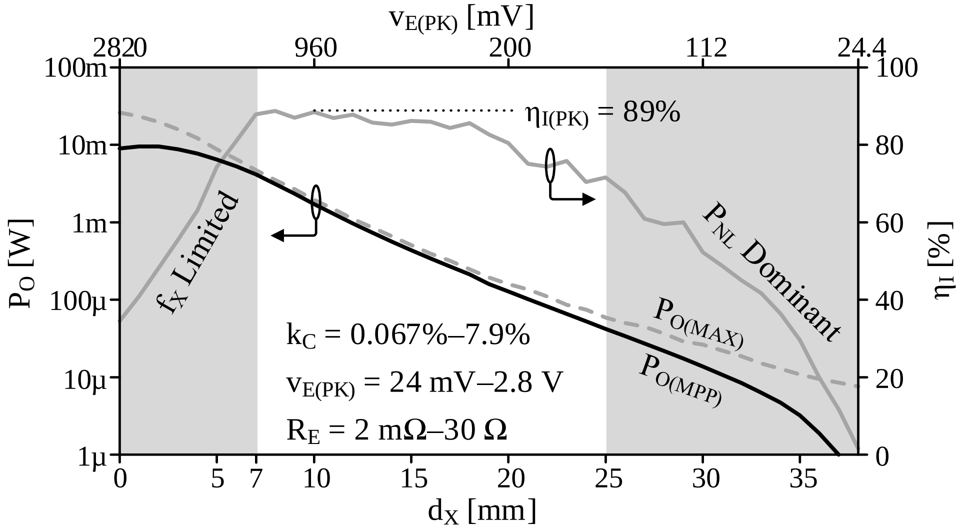

Figure 6-17. Measured ideality factor across power transmission distance d_X.

On the other end, when d_X is shorter than 7 mm, η_I is also low. This is because, as the transmitting source couples more v_E on the receiving coil, $f_{X(MPP)}$ scales up linearly and eventually reaches the oscillation frequency f_O. Beyond that, f_X cannot grow anymore, because the wireless charger can at most transfer energy once per oscillation cycle. Therefore, the MPP controller can no longer adjust for the desired $f_{X(MPP)}$, so η_I starts to drop. As shown in Figure 6-18, $f_{X(MPP)}$ reaches f_O as $v_{E(PK)}$ grows above 0.58 V. Then $f_{X(MPP)}$ is capped to f_O and $P_{O(MPP)}$ becomes f_X-limited. Transferring energy for a longer duration t_{ON} improves η_I when the coupling is high and $P_{O(MPP)}$ is f_X-limited. However, for targeted biomedical implant applications, high coupling is unlikely. Plus, adjustable t_{ON} requires additional circuitry and quiescent power. So t_{ON} is fixed at 960 ns.

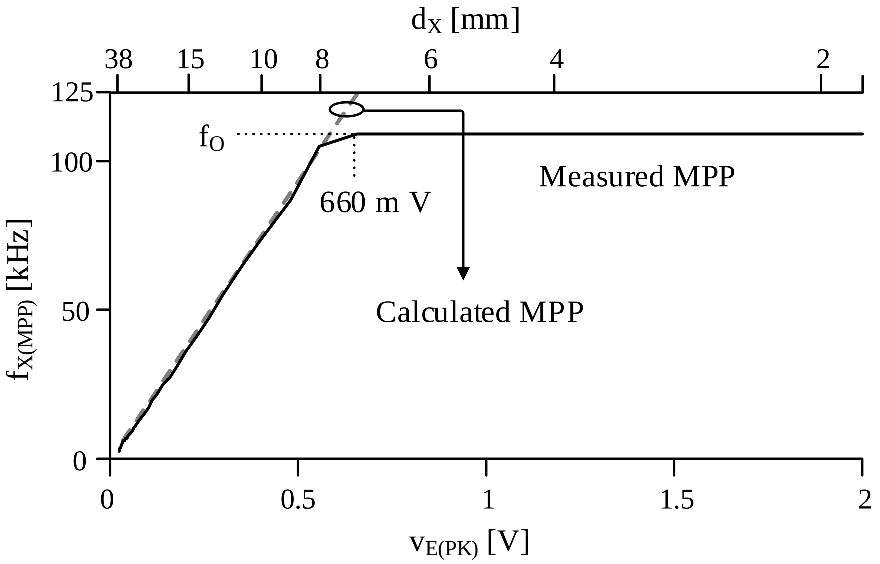

Figure 6-18. Measured $f_{X(MPP)}$ across $v_{E(PK)}$.

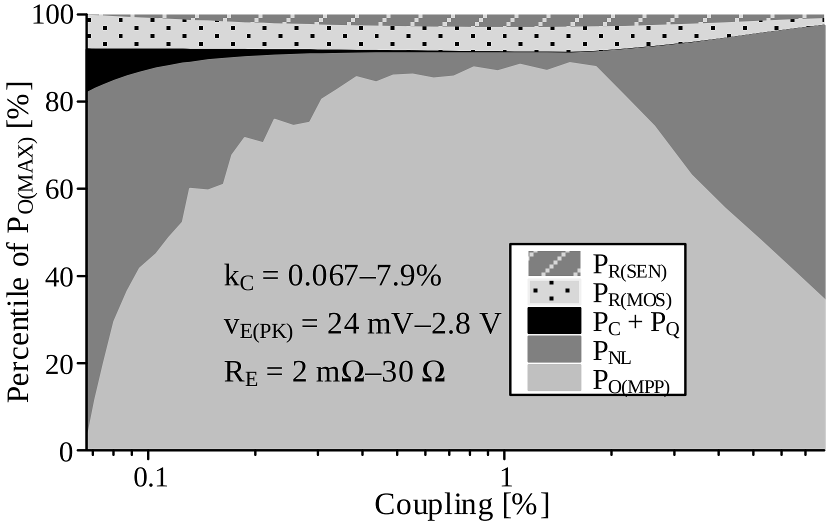

Figure 6-19. Loss breakdown of the self-synchronized power receiver.

Figure 6-19 shows the loss breakdown of the proposed switched resonant half-bridge with self-synchronization as a percentage of the maximum available power $P_{O(MAX)}$. Below 0.7% of k_C, the nonlinear loss P_{NL} dominates. This is because, at very low v_E, the oscillation voltage v_C is low. Connecting the battery almost completely drains the LC tank and kills the oscillation. As a result, the v_C deviates widely from its optimal value, so the P_{NL} is high.

P_{NL} dominates as kC grows beyond 1.2%. This is because the MPP controller can no longer adjust for the desired $f_{X(MPP)}$ so $P_{O(MPP)}$ becomes f_X-limited.

6.3.3 Relative Performance

Figure 6-20 compares the proposed charger's η_I across k_C with the state of the arts. The wireless chargers in [123], [80], and [136] are based on switched resonant half-bridge and its variations. Although [80] achieves an ideality as high as 85%, the charger cannot self-synchronize. Therefore, the system is incomplete. The charger in [123] has no synchronizer either. Plus, as the charger completely drains LC tank's energy each time, the energy transfer is not optimal. So ideality is low at 42.9%. The charger in [136] is self-synchronized and achieves 67.7% of η_I. However, its power stage cannot operate beyond the circuit's breakdown, so the coupling range is 16× narrower. The charger in [136] includes a maximum power point tracking (MPPT) that this design does not have. However, the MPPT is based on a one-time calibration, so its power consumption is ignored when calculating the ideality. [136] is not included in Fig. 14, as the coupling information cannot be extracted from the paper.

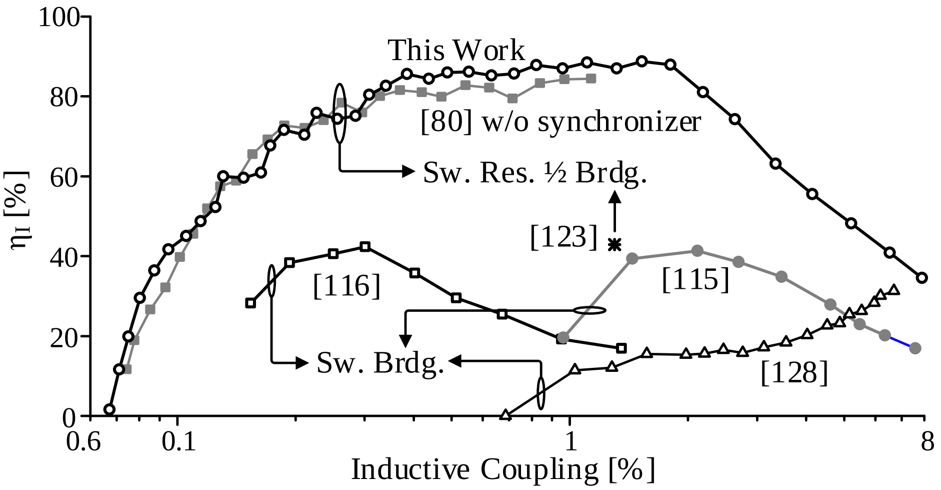

Figure 6-20. Measured ideality index.

The switched bridges in [128], [115], and [116] energizes and de-energizes L_R directly with the battery. As the switches in the switched bridge see the inductor voltage, the circuit cannot operate beyond breakdown. So the workable coupling ranges are much lower compared to the proposed design. The chargers in [128] and [115] cannot self-synchronize, so the systems are incomplete. Although the charger in [116] includes an integrated synchronizer, the synchronizer needs to break the charging operation, resulting in additional opportunity loss. As a result, its $\eta_{I(PK)}$ is 42.4%.

Table 6-1 summarizes and compares the performance of the proposed design with the state of the arts. The charger systems in [123], [80], [128], and [115] are incomplete as they do not include a synchronizer. Still, among all designs, the proposed design achieves the highest η_I of 89% and the widest k_C range of 41 dB. Compared to other self-synchronized wireless chargers, the proposed wireless charger improves η_I and k_C range by 1.3× and 13×, respectively.

Table 6-1. Relative Performance

	JSSC [128]	TCAS II [115]	JESTPE [116]	TCAS I [123]	TCAS II [80]	JSSC [125]	This Work
Receiver Type	Switched Bridges			Switched Resonant Half-bridges			
Technology (μm)	0.18	0.18	0.18	Board	0.18	0.18	0.18
Si Area (mm^2)	0.49	0.245	0.260	–	0.471	0.544	0.084
f_O (MHz)	0.125	0.125	0.125	1	6.78	50	0.11
k_C (%)	0.59–6.7	0.9–7.6	–	1.3	0.09 –1.1	–	0.067–7.9
$v_{E(PK)}$ (mV)	39.5–386	46–480	66–585	41	18.5–282	–	24–2880
$P_{O(MPP)}$ (μW)	0–224	8–390	16–557	96.1	1.2–1340	0–2.84	0.1–26000
Over-V_{BD} Operation	No	No	No	Yes	Yes	No	Yes
Self-Sync.	No	No	Yes	No	No	Yes	Yes
MPPT	No	No	No	No	No	Yes	No
$\eta_{I(PK)}$ (%)	30.9*	46.9*	42.4*	42.9	84.8	67.7	88.8
Dynamic Range (dB)	21	19	19	–	24	17	41

*Ideality inferred from the reported $P_{O(MPP)}$, $v_{E(PK)}$, R_R, and estimated R_F, using (3) and (4). R_F is estimated as in [7].

To sum up, an inductively coupled wireless charger needs to output the highest power possible across a wide coupling range for practical applications. The switched resonant half-bridge outputs the highest power over a wide coupling range, as the circuit can operate beyond the circuit's breakdown voltage and adjusts energy transfer patterns for MPP. However, the over-breakdown operation makes synchronizing the control a challenge. This chapter proposes a self-synchronized switched resonant half-bridge inductively coupled wireless charger. Using a high-voltage-sensing circuit, the charger synchronizes the control with minimal loss. A prototype is fabricated using 180-nm CMOS technology. Measurements show that the proposed design improves the output power and workable coupling range by 1.3× and 13× over the state of the art.

6.4 Discussion: Inductively Coupled vs. RF

This chapter presents a self-synchronized switched resonant half-bridge power receiver that can output up to 89% of the available power. It is interesting to see how the inductively coupled power receiver compares with another popular wireless power transfer technology: RF power transfer.

6.4.1 Inductively Coupled

A typical L-coupled power transfer system is shown in Fig. The power transmitter's L_T-C_T is usually driven by a power inverter [137]–[121] which is modeled by a low-impedance square-wave voltage source v_S. Since L_T-C_T only band-passes current at the resonant, the equivalent driving voltage at the transmitter is v_S' fundamental tone at f_O:

$$v_{S(PK)}^{(f_O)} = \left(\frac{4}{\pi}\right) v_{S(PK)}. \tag{6.7}$$

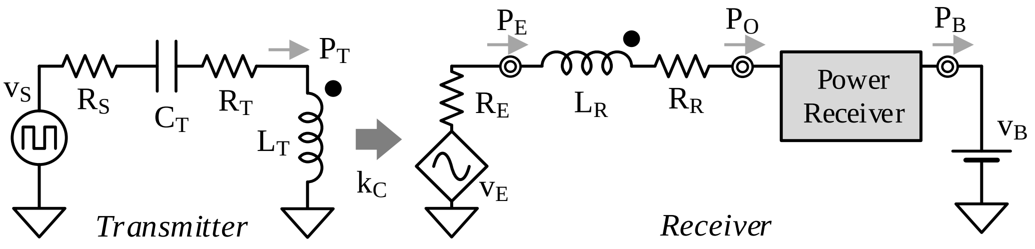

Figure 6-21. Inductively coupled power transfer system.

As discussed in the previous chapters, The key to drawing max power from L_R is that the receiver "load match" the source impedance [99], as Fig. 7 shows. A capacitor C_R is often used to create resonance and raise L_R's current, so as to boost the power drawn from v_E [99]. P_O is maximum when $v_R = 0.5\ v_E$ [98]:

$$P_{O(MAX)} = \frac{\left(0.5v_{E(RMS)}\right)^2}{R_E + R_R} = \frac{\left(\frac{0.5v_{E(PK)}}{\sqrt{2}}\right)^2}{R_E + R_R}. \tag{6.8}$$

When closely coupled, $R_E >> R_R$. So $P_{O(MAX)} \approx P_{E(MAX)}$ and does not scale with d_X:

$$P_{O(MAX)}\Big|_{R_E >> R_R} \approx P_{E(MAX)} = \frac{\left(0.5v_{S(PK)}{}^{(f_O)}\right)^2}{2R_T} \neq f\left(d_X\right). \tag{6.9}$$

At high d_X, the receiver barely loads the transmitter, so $R_E << R_R$. As a result, $P_{O(MAX)}$ scales quadratically with $v_{E(PK)}$:

$$P_{O(MAX)}\Big|_{R_R >> R_E} \approx \frac{\left(\frac{0.5v_{E(PK)}}{\sqrt{2}}\right)^2}{R_E} \propto \left(\frac{1}{d_X{}^3}\right)^2. \tag{6.10}$$

To validate the theory above, Figure 6-22 compares the Spice simulated $P_{O(MAX)}$ with the calculation when the coupling k_C ranges from 0.01%-100%. Proportional to $v_{E(PK)}$ [80], k_C

also drops cubically with d_X. The simulation adjusts the effective receiver load as a resistor in Figure 6-21 for $P_{O(MAX)}$. The simulated $P_{O(MAX)}$ closely matches the theory's prediction. Below $k_{C(SAT)}$ (~1.5%), $P_{O(MAX)}$ drops –20dB/dec with $v_{E(PK)}$. Beyond $k_{C(SAT)}$ $P_{O(MAX)}$ saturates as the power is limited by the available power from the transmitter. The simulation matches the calculation within 0.1% to 0.2% error when $v_{E(PK)}$ is above 20 mV. Below 20 mV, the error increases to –0.4% to 2.5% due to the dynamic range limitation of the simulation.

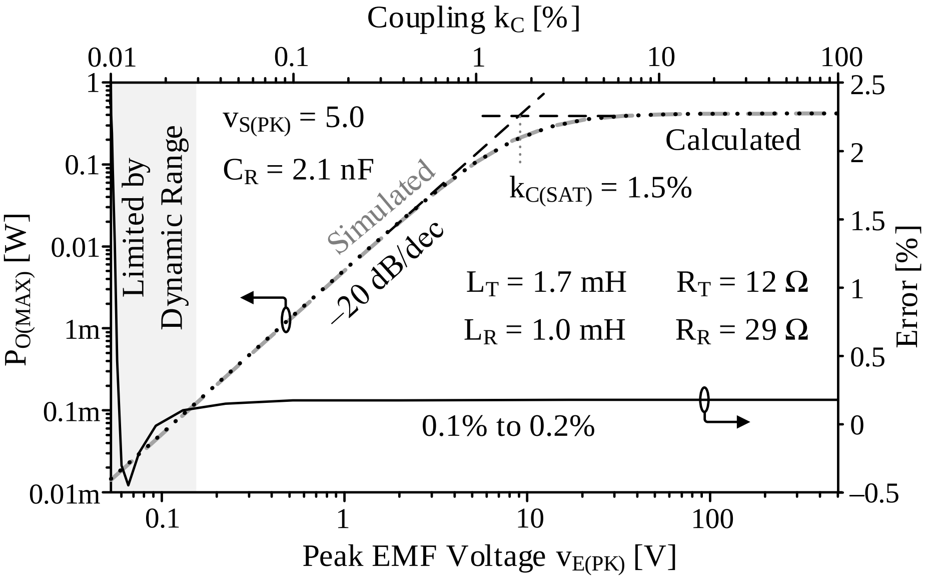

Figure 6-22. Calculated and circuit simulated $P_{O(MAX)}$ at different $v_{E(PK)}$.

6.4.2 RF

An RF antenna projects its power P_T to a sphere surface A_T, as Figure 6-23 shows. For a non-isotropic antenna, the power radiation is not uniform in every direction. Antenna gain G_T characterizes the non-uniformity of power density in different directions. So the power density at d_X is both a function of d_X and angle θ, as Figure 6-23 shows:

$$PD_T = \frac{P_T G_T}{A_T} = \frac{P_T G_T}{4\pi {d_X}^2}. \tag{6.11}$$

For dipole antennae, PD_T maximizes at $\theta = 0$ and minimizes at $\theta = \pm 90°$. The received power is proportional to both of PD_T, the effective receiver antenna aperture A_R', and the receiver's antenna gain G_R [90]:

$$P_O\Big|_{d_X > 4d_\lambda} = PD_T A_R' G_R = \left(\frac{P_T G_T}{4\pi d_X^{\;2}}\right)\left(\frac{d_\lambda^{\;2}}{\pi}\right) G_R \,. \qquad (6.12)$$

Equation (6.12) is widely referred to as the Friis formula. Note the formula is reasonably accurate in the far-field region when $d_X > 4d_\lambda$, where d_λ is the length of the half-wave dipole antenna.

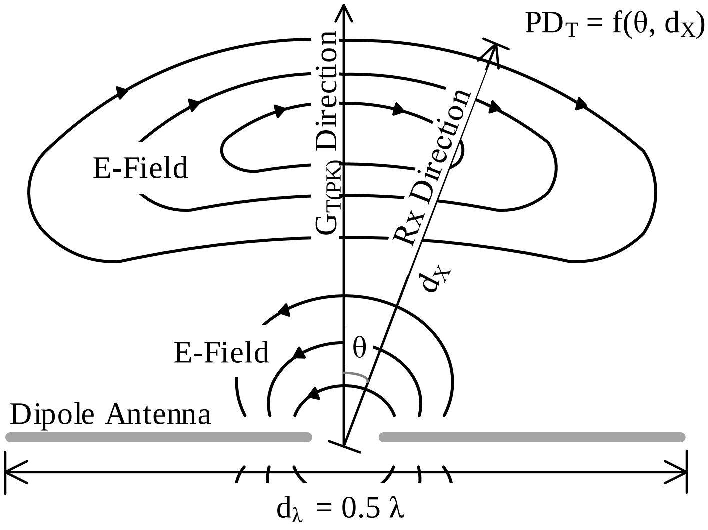
$PD_T = f(\theta, d_X)$
$G_{T(PK)}$ Direction
R_X Direction
E-Field
d_X
E-Field
θ
Dipole Antenna
$d_\lambda = 0.5\,\lambda$

Figure 6-23. Dipole antenna momentary electric field.

The RF power transfer system generates the highest output power when both transmitter and receiver antennae align along their peak power density direction, so $P_{O(MAX)}$ drops quadratically with d_X:

$$P_{O(MAX)}\Big|_{d_X > 4d_\lambda} = P_T G_{T(PK)} \left(\frac{d_\lambda}{2\pi d_X}\right)^2 G_{R(PK)} \propto \frac{1}{d_X^{\;2}} \,. \qquad (6.13)$$

$G_{T(PK)}$ of a dipole antenna is normally 2.15 dBi [138]. $G_{R(PK)}$ is the peak antenna gain of the receiver.

6.4.3 Comparison: An Example

As an example, this section compares the power density decay of a 125 kHz L-coupled power system with a 2.45 GHz RF power system. While both 125 kHz and 13.56 MHz are widely used for L-coupled power transfer, 125 kHz operation lowers the switching loss and is more suitable for low-power microsensor applications. 2.45 GHz is widely used for RF power transfer, so the power link can be shared with the data link such as Wifi and Bluetooth.

For a compact system, the transmitter needs to be small in all directions. The transmitter’s dimension d_L characterizes the side length of the smallest square that the transmitter can fit into. A 2.45 GHz half-wave dipole measures 6.1 cm, which fits right into 4.3×4.3×0.2 cm^3 cubic of space, so its d_L is 4.3 cm. For a fair comparison, the L-coupled transmitter coil is also limited to the same cubic of space, as Figure 6-23 shows. The inductor coil used here is a 250-turn, 43 mm diameter, single-row coil. The calculated inductance is around 1 mH [139]. For the receiver, the L-coupled power system uses the Coilcraft 4513TC 1 mH coil with 31 mV/µT sensitivity. The RF system uses the patch antenna SWLP.2450.10.4.A.02 from Taoglas. Figure 6-23 shows their dimensions. Parameters of the transmitters and receivers are summarized in Table 6-2.

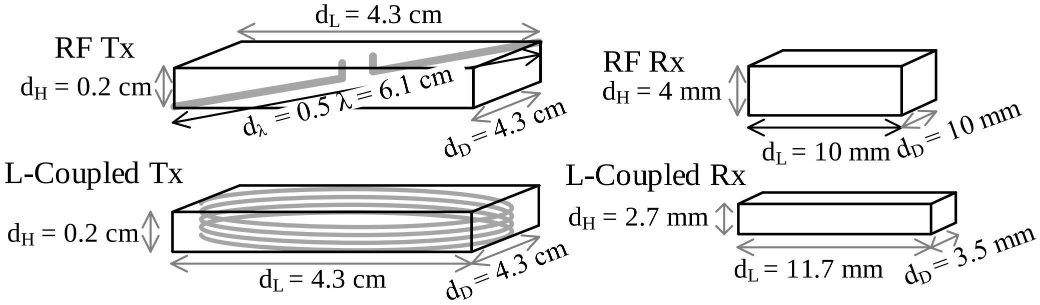
RF Tx
d_L = 4.3 cm
d_H = 0.2 cm
d_λ = 0.5 λ = 6.1 cm
d_D = 4.3 cm
RF Rx
d_H = 4 mm
d_L = 10 mm
d_D = 10 mm
L-Coupled Tx
d_H = 0.2 cm
d_L = 4.3 cm
d_D = 4.3 cm
L-Coupled Rx
d_H = 2.7 mm
d_L = 11.7 mm
d_D = 3.5 mm

Figure 6-24. Dimensions of the L-coupled and RF transmitters and receivers.

Table 6-2. Parameters for the inductively coupled and RF system.

Parameter	Value	Parameter	Value
RF Power Receiver: TAOGLAS SWLP.2450.10.4.A.02			
d_H	4 mm	d_D	10 mm
d_L	10 mm	$G_{R(PK)}$	–1 dBi
L:L Power Transmitter Coil [139]			
μ_{EFF}	12.6 mN·A^{-2}	L_T	1.7 mH
N_T	250	R_T @ f_O	12.1 Ω
d_H	2 mm	f_O	125 kHz
r_T	21.5 mm	$v_{S(PK)}$	5 V
L:L Power Receiver Coil: Coilcraft 4513TC			
d_H	2.7 mm	L_R	1 mH
d_L	11.7 mm	$R_{ESR.R}$ @ f_O	23.9 Ω
d_D	3.5 mm	S_{RX}	31 mV/μT
RF Power Transmitter: Dipole [138]–[140]			
f_O	2.45 GHz	d_λ	61 mm
λ	122 mm	$G_{T(PK)}$	2.15 dBi

Figure 6-25 compares the η_{PD} of the above discussed L-coupled and RF power transfer systems. The solid lines indicate the η_{PD} calculated from the theory, while the dashed line indicates the qualitatively projected η_{PD} of the RF system in the near-field region. The Friis equation is only accurate for the far-field region. The power in the near-field region much more complex, as it is subject to the antenna's shape and position [141]. The discussion is beyond this research's scope. Up to d_L, L-coupled system's η_{PD} stays flat, as the transmitting source limits $P_{O(MAX)}$. In this region, the L-coupled system's η_{PD} is always higher, as the L-coupled receiver can potentially source all the power that the transmitter avails, while the RF system always loses a portion of the power it radiates into space (% P_{LOSS}). Past d_L, $P_{O(MAX)}$ or η_{PD} drops 3 times faster than the RF system. Past 3.5 d_L, η_{PD} of the L-coupled system is surpassed by the RF system. More generally, RF system outputs higher power in the far-field region, while the inductively coupled system output higher power in deep near-field region.

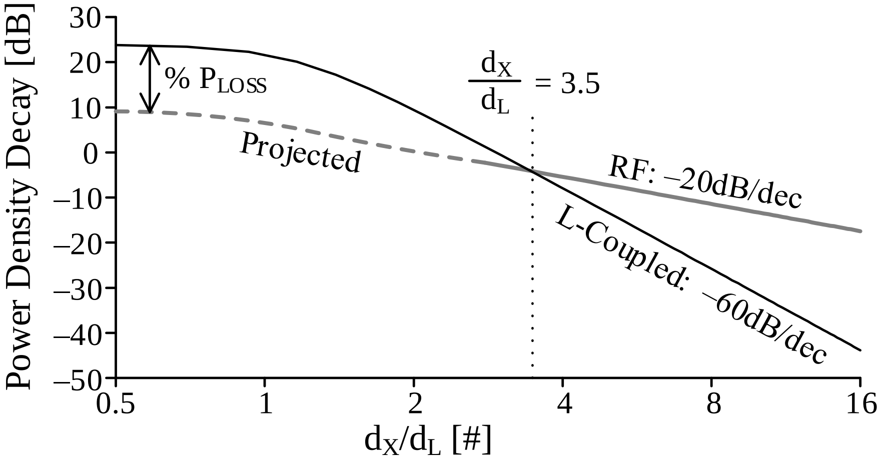

Figure 6-25. Comparison between inductively coupled RF power density attenuation over distance.

To sum up, this discussion compares the maximum output power performance of the two most popular wireless power transfer technologies: L-coupled and RF. With normalized transmitter power and size, up to d_L, L-coupled power receiver outputs higher power density η_{PD}, as it can output as much power as the transmitter avails, while the RF system always loses the power that radiates into space. However, past d_L, the L-coupled system's η_{PD} decays 3 times as fast as the RF system over d_X. So beyond 3.5 d_L, RF's η_{PD} beats the L-coupled.

CHAPTER 7. CONCLUSIONS

7.1 Research Objective

Embedded microsensors can sense, process, and transmit information that saves energy, cost, and lives Their tiny onboard batteries, nevertheless, cannot sustain their operation for long. Harvesting ambient energy, such as light or motion can help replenish the battery and extend the lifetime. However, such energy sources are rarely available in an embedded environment. Often, the only option left is to recharge the battery wirelessly using a pair of inductively coupled coils.

Powering embedded microsensors via a pair of inductively coupled coils is challenging for three reasons. First, coupling in these applications is very weak because the separation between the transmitter and receiver coils far exceeds the radius of the coils. Such a tiny, weakly coupled and often misaligned receiver coil only couples millivolts, so drawing power is difficult. Second, applying a high voltage boosts coil current and, in consequence, outputs more power, but only to the extent that the circuit's breakdown voltage allows. In other words, the circuit is breakdown limited. Third, tiny coils are so resistive that ohmic losses also constrain output power.

With this understanding, the research will then explore and develop a low-loss CMOS power receiver with a microwatt controller that can operate the system so output power is maximally high. The ultimate goal is to build a power-receiver system that can draw and output more power than the state of the art, and that way, expand the functionality, life, and application space of emerging biomedical implants and structurally embedded microsensors.

7.2 Contributions

7.2.1 Evaluation of the SoA Power Receivers

The first contribution of this research is the evaluation of SoA power receivers and the identification of the best technology. In most embedded microsensor applications, the coupling between the transmitter and the receiver coils is often very low. So the coupled voltage v_E is low in millivolts. Applying a high, alternating voltage v_R across the receiver coil, as shown in boosts the current i_L and thus the drawn power from v_E. However, the quadratic growing conduction loss may negate the gain in drawn power when the current is too high. Therefore, the key to generating the highest power is to apply the optimal voltage across the receiver coil.

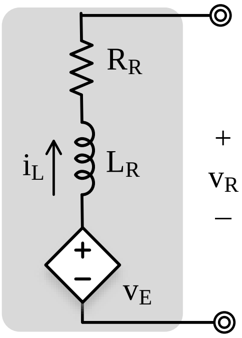

Figure 7-1. Applying an alternating high voltage v_R boosts i_L and power from v_E.

The resonant full-/half-bridge, the investing switched bridge, and the switched resonant bridge all impress an alternating high voltage across the receiving coil L_R but in different ways. The resonant half/full bridges in Figure 3-1 and Figure 3-5 parallel a resonant capacitor C_R with L_R. In this case, v_R is the resonate voltage v_C. To regulate the v_C at its optimal level $v_{C(OPT)}$, an extra buffer stage is needed to regulate the rectified voltage v_{REC}, as v_{REC} caps v_C. The extra buffer stage adds losses and components to hurting the efficiency and compactness of the system. Plus, the maximum v_{REC} is limited by the circuit's breakdown. So the receiver can reach MPP only for a narrow coupling range. The investing switched bridge impresses a high, alternating v_R by connecting L_R directly to $\pm v_{REC}$. Similarly, an extra buffer regulates v_{REC} so the output power is maximum. Still, the maximum v_{REC} is limited by breakdown, so the MPP coupling range is low. The switched resonant bridge connects a resonant capacitor C_R in series with the bridge circuit. For most of the cycle the bridge circuit shorts, so v_R in this case is mostly v_C. Unlike the other two types of power receivers, the switched resonant bridge can adjust v_C level by adjusting the energy transfer duration. This eliminates the need for additional buffer stage. Plus, as the switches in the bridge do not see v_C, v_C is not breakdown limited.

As all three types of power receivers adjust v_R for MPP, they output about the same power, as shown in Figure 3-18. However, the switched resonant does not require a buffer stage, so the system can be more compact. Plus, the switched resonant bridge power receiver is not breakdown limited, so it can reach MPP for a wider coupling range. Therefore, it is the best SoA power receiver for powering embedded microsensors.

To assess the relative performance of the power receiver, an ideality index is proposed. The receiver efficiency is not a good performance metric here, as the goal is to maximize the power not efficiency. The maximum output power, however, scales with the coupling, transmitting power, and coil inductance. So it does not reflect the performance of the receiver itself. The ideality factor η_I references the maximum output $P_{O(MPP)}$ to the maximum available power $P_{O(MAX)}$ and normalizes $P_{O(MPP)}$ with non-receiver variables:

$$\eta_I = \frac{P_{O(MPP)}}{P_{O(MAX)}}. \tag{7.1}$$

For this reason, the ideality index η_I is used to assess the relative performance of the power receiver.

Generated Peer-Reviewed Conference Publication(s):

- N. Xing and G. A. Rincon-Mora, "Generating the highest power with a tiny and distant inductively coupled coil," *2016 IEEE 25th International Symposium on Industrial Electronics*, pp. 477-80, June 2016.

7.2.2 MPP Power Stage

The second contribution of this research is a novel switched resonant half-bridge that adjusts both energy transfer duration and frequency for MPP. The proposed switched resonant half-bridge, as shown in Figure 7-2 operates and switches between two modes. During the energy accumulating mode, the ground switch M_G conducts, closing the LC oscillation loop. So the LC tank constantly receives and accumulates energy from the coupled source v_E. During the energy transferring mode, the output switch M_O closes, transferring the energy accumulated in the LC partially to the battery v_B.

The circuit can adjust both energy transfer duration t_{ON} and frequency f_X for MPP. In this case, the voltage v_R impressed across L_R is mostly the oscillating voltage v_C. Transferring energy for longer and more frequently leaves less energy in the LC tank, so the averaged v_C magnitude is lower. Similarly, transferring energy less often or shorter leaves more energy in the LC tank, so the averaged v_C magnitude is higher. This way, the switched resonant half-bridge adjusts both t_{ON} and f_X for MPP, as Figure 7-3 shows.

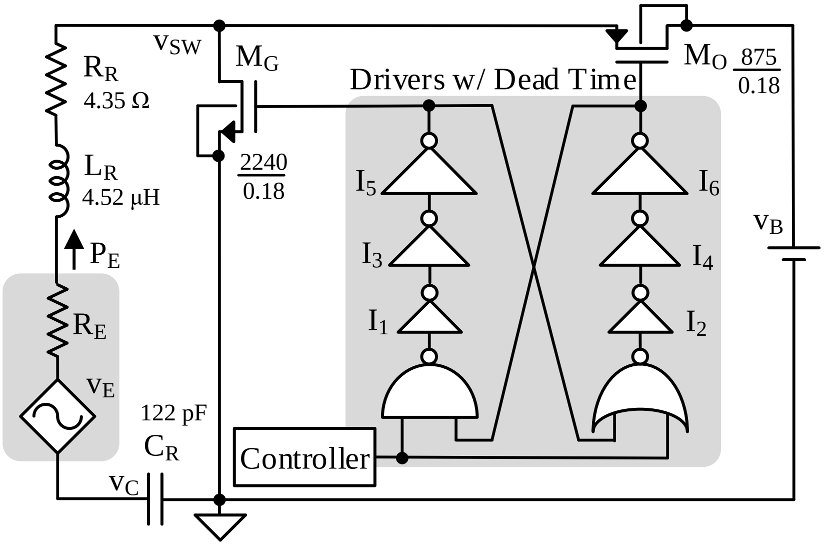
vSW
MG
RR
4.35 Ω
LR
4.52 μH
PE
RE
vE
122 pF
CR
vC
2240
0.18
Drivers w/ Dead Time
MO
875
0.18
I5
I6
I3
I4
I1
I2
vB
Controller

Figure 7-2. The switched resonant half-bridge that adjusts both energy transfer duration and frequency for MPP.

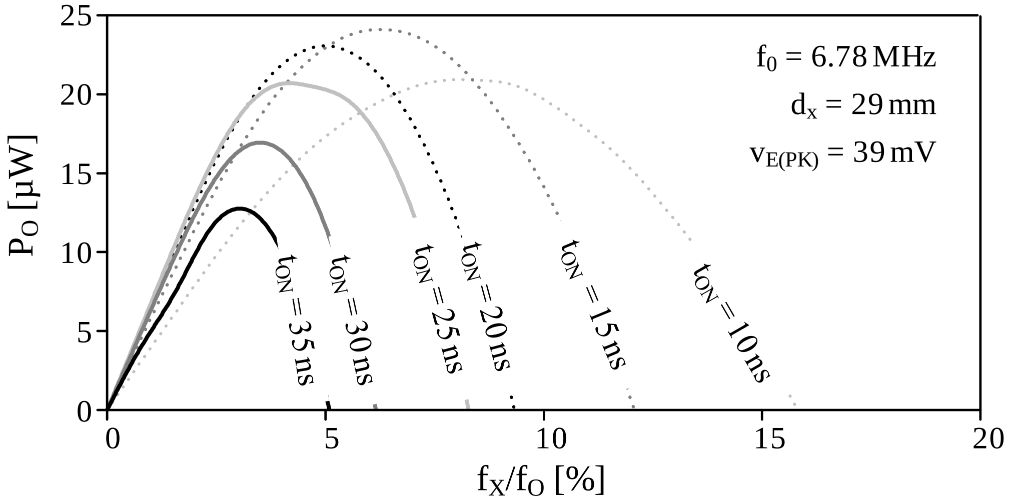

Figure 7-3. Adjusting both t_{ON} and f_X for MPP with 39 mV coupled voltage.

Compared to the other switched resonant bridges [117-122], the proposed power stage uses 2 FETs only, so the power stage can be more compact and is more suitable for microsensor applications. Also, the resonant capacitor C_R is grounded. So there is less parasitic capacitance and thus less switching loss. This also makes sensing v_C easier. Moreover, the power stage uses synchronous switches, so there is no diode loss. Finally, the power stage can adjust both energy transfer frequency f_X and duration t_{ON}. The two-variable space captures more settings than a single variable can, so the maximum power $P_{O(MPP)}$ is higher. A prototype is built using 180-nm CMOS technology. The prototype operates at 6.78 MHz and outputs 13%–85% of the 9.7–1580 μW that a 54.1-mm^2 receiver coil avails when 13 to 38 mm apart from its source. This is up to 38% more power and with 25% smaller footprint than the best comparable receiver.

Generated Peer-Reviewed Journal(s):

- N. Xing and G. A. Rincón-Mora, "180-nm 85%-efficient inductively coupled switched resonant half-bridge power receiver," *IEEE Transactions on Circuits and Systems II: Express Briefs,* vol. 66, no. 6, pp. 983-987, 2019.

7.2.3 MPP Theory

The third contribution is the development of an MPP theory that predicts the optimal settings for the proposed switched resonant half-bridge. The proposed switched resonant half-bridge achieves up to 85% ideality, as it can adjust both energy transfer duration t_{ON} and frequency f_X for MPP. However, searching for the optimal f_X and t_{ON} setting thoroughly across the two-variable space can be time- and energy-consuming. Also, coupling varies from time to time in most embedded microsensor applications, which means the optimal setting also needs to be adjusted from time to time. Searching for MPP setting frequently halts the power transfer and causes significant opportunity loss. Therefore, in this research, a theory that predicts the optimal settings of t_{ON} and f_X is developed.

Briefly, the switched resonant half-bridge reaches MPP when two criteria are met: (1) the receiver voltage v_R's harmonic at f_O matches $0.5v_E$ in both phase and magnitude, and (2) the energy transfer frequency f_X balances the nonlinear loss and the charge loss. Criterion (2) is quite self-explanatory. However, criterion (1) is not so straight-forward. An intuitive explanation of (1) is that, as the L_R and C_R only bandpass current at f_O, it is the v_R's harmonic at f_O that dominates the current. Therefore, matching the v_R's harmonic at f_O to $0.5v_E$ results in close-to-MPP output power. With the two criteria, the optimal t_{ON} and f_X can be obtained as:

$$f_{X(MPP)} = f_O\left[\left(\frac{\pi}{2Q_R}\right)^2\left(\frac{P_{L(MAX)}'}{P_{C(f_O)}}\right)\right]^{1/3} \tag{7.2}$$

and

$$t_{ON(MPP)} = \left(\frac{t_O}{\pi}\right)\sin^{-1}\left[\left(\frac{\pi}{4}\right)\left(\frac{v_{E(PK)}}{v_B}\right)\left(\frac{f_O}{f_{X(MPP)}}\right)\right]. \tag{7.3}$$

Although the predicted $t_{ON(MPP)}$ and $f_{X(MPP)}$ do not match the measurement well (with up to 32%), the output power at the predicted setting is very close to the actual measured $P_{O(MPP)}$. As Figure 7-4 shows, at the theory's predicted settings, the receiver outputs more than 98.7% of the actual maximum power when the coupling is 0.15%–1.13%.

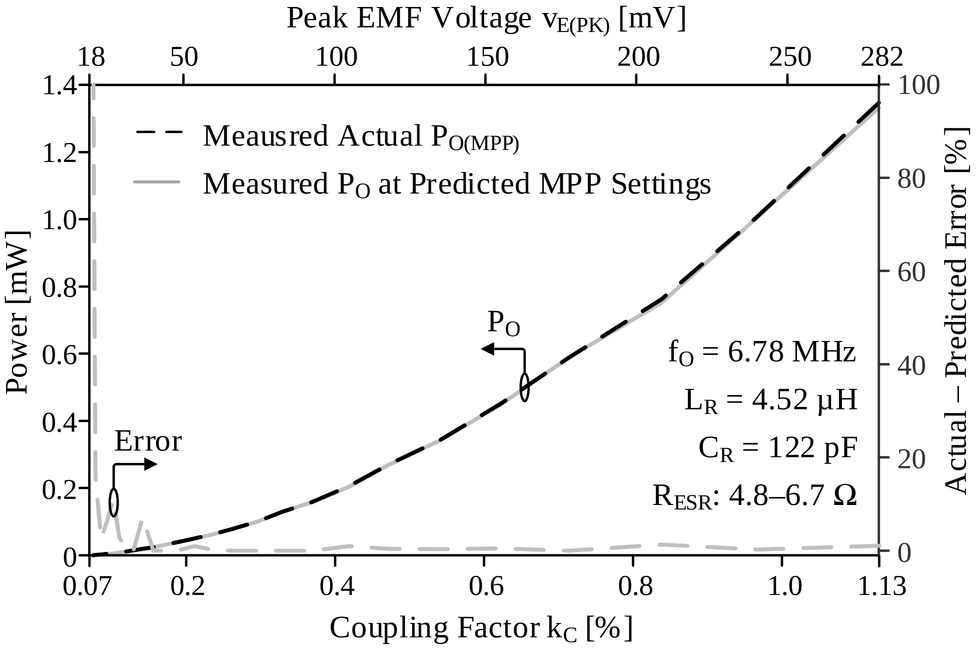

Figure 7-4. P_O at the theory's predicted setting and the actual $P_{O(MPP)}$.

Generated Peer-Reviewed Conference Publication(s):

- N. Xing and G. A. Rincon-Mora, "Power analysis and maximum output-power scheme for inductively coupled resonant power receivers," *2017 IEEE 60th International Midwest Symposium on Circuits and Systems*, pp. 293-6, August 2017.

Generated Peer-Reviewed Journal(s):

- N. Xing and G. Rincon-Mora, "Highest maximum power point of radially distant inductively coupled power receivers with deep submicron CMOS," *IEEE Transactions on Industrial Informatics*, no. DOI: 10.1109/TII.2019.2910092.

7.2.4 System Integration

The last main contribution of this research is the system integration of the switched resonant half-bridge. Although the switched resonant half-bridge charger can output high power across a wide coupling range, its synchronized control remains a challenge. For MPP, the circuit needs to transfer energy from the LC tank to the battery around i_L's peak. Sensing i_L directly is difficult, as i_L is low and varies orders of magnitude in targeted applications. Plus, any resistance added to the LC loop significantly lowers the available power to the receiver. An alternative way is to sense v_C's zero-crossing, as that's when i_L peaks. However, sensing v_C's zero crossings is challenging as well. This is because v_C can also vary orders of magnitude in real applications and exceed the breakdown voltage. Moreover, the v_C can swing below zero.

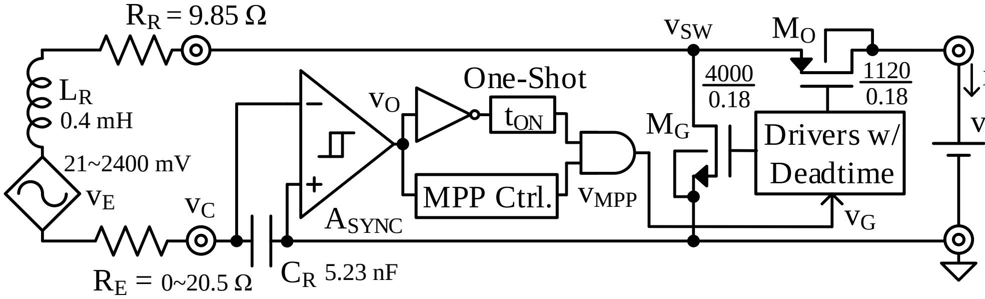

Figure 7-5. Self-synchronized switched resonant half-bridge power receiver.

To address the challenges, the synchronizing comparator A_{SYNC} in Figure 7-5 pre-divides the capacitor voltage v_C with a variable-ratio divider. The dividing ratio is higher when the input is high, so the comparator output v_O does not exceed the breakdown and protects the circuit. The dividing ratio drops to one when the input is low, so v_O is high enough for the comparator input. The voltage divider induces loss as it steals and burns a fraction of i_L. However, the loss is less than 3%.

The energy transfer frequency controller is implemented on an FPGA for testability. The controller block is fully synthesizable with the comparator output as the only clock. So the controller can be migrated on-chip if required. The controller linearly controls the energy transfer frequency f_X with a $f_O/128$ resolution.

The measured self-synchronized switched resonant half-bridge achieves an ideality as high as 89%, which is 1.3× higher than the comparable state of the arts. Also, because the power stage and the synchronizing comparator can handle high voltage above breakdown, the circuit’s coupling is as wide as 41 dB, which is 13× higher than the comparable state of the arts.

Generated Peer-Reviewed Conference-Publication(s):

- N. Xing and G. A. Rincon-Mora, "Highest Wireless Power: Inductively Coupled Or RF?" *2020 IEEE International Symposium on Quality Electronics Design*, accepted for publication.

Generated Peer-Reviewed Journal(s):

- N. Xing and G. Rincon-Mora, "180-nm 0.067%-7.9% coupled-range 89%-efficient self-synchronized inductively coupled wireless charger," Submitted *IEEE Transactions on Circuits and Systems II: Express Briefs*

7.3 Remaining Challenges & Future Research

The final design in CHAPTER 6 significantly improves the power receiver’s ideality and coupling range over the state of the arts by 1.3× and 13×, respectively. However, the technology still has limitations. This section discusses the limitations of the proposed technology and potential future research paths.

7.3.1 Zero-Energy Start-up

The proposed self-synchronized switched resonant half-bridge power receiver in Figure 7-5 requires initial energy to turn on the ground switch M_G. Without the initial energy to turn on M_G, the LC loop stays open and cannot collect energy from the coupled source v_E. This is a serious limitation compared to the resonant bridge. In a resonant bridge, the LC loop is always closed, so energy can accumulate from zero in the LC tank and get transferred to the rectified capacitor.

Zero-energy start-up capability is critical for many embedded microsensor applications. The onboard batteries of these embedded microsensors are usually tiny. Plus, the availability of the power source is uncertain in many applications. As a result, the onboard battery depletes easily. To revive the system from a completely discharged state, a zero-energy startup is necessary.

Therefore, one of the future research paths is the zero-energy startup of the switched resonant half-bridge. It is worth noting that although the ground switch MG is open, the parasitic capacitance C_{PAR} from v_{SW} to GND still closes the loop. Yet the loop L_R–C_R–C_{PAR} oscillates at a much higher frequency, as C_{PAR} is normally orders of magnitude smaller than the resonant capacitor C_R. So one option to start up the system is to upshift the transmitter frequency to L_R–C_R–C_{PAR}'s resonate frequency to excite the oscillation during startup. Once the parasitic LC tank accumulates enough energy and charges up v_B to the minimum required voltage, the transmitter can shift back to the normal operation frequency for optimal performance. However, this startup scheme has significant drawbacks. First, the start-up scheme requires the transmitter to be able to operate in two separate frequency bands, which significantly complicated the transmitter design. Also, the parasitic capacitance varies from chip to chip. So the start-up transmitting frequency needs to be calibrated individually for each receiver IC.

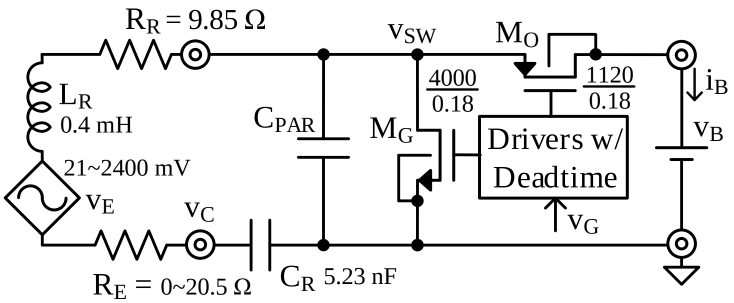

Figure 7-6. Startup the switched resonant half-bridge with the help of C_{PAR}.

An alternative way is to use auxiliary start-up circuits like in [142, 143]. However, as the circuit resumes normal operation, the start-up circuit sees the high oscillation voltage v_C. How to protect the start-up circuit from the high voltage becomes another challenge.

7.3.2 Maximum Power Point Tracking (MPPT)

The switched resonant half-bridge in CHAPTER 6 adjusts the energy transfer frequency f_X for MPP. However, the frequency adjustment is done in an open-loop fashion: in coupled voltage was calibrated once to set the optimal energy transfer frequency. For real applications, the distance between the transmitting and receiving coil often varies with time. So f_X needs to be updated from time to time for MPPT:

$$f_{X(MPP)} = \left(\frac{\pi}{4}\right)\left(\frac{v_{E(PK)}}{v_B}\right) \Big/ \sin\left[\left(\frac{t_{ON}}{t_O}\right)\pi\right]. \tag{7.4}$$

Most state-of-the-art MPPT or maximum power efficiency tracking (MPET) schemes [144-147] calibrate the output power or output current. However, the output current is low and intermittent in the switched resonant half-bridge, making the calibration difficult. One MPPT option is to break the power receiving operation and calibrate coupled v_E once in a while. Figure 7-7 shows the MPPT scheme. The ground switch S_G and output switch S_O turn on alternatively during the energy receiving and transferring operation. To calibrate the open-loop voltage v_E, both switches are turned off, so $v_{E(CL)} = v_E$. The open-loop voltage is then fed to an ADC and a look-up table (LUT) to determine the optimal f_X for MPP.

However, the MPPT suffers several drawbacks. First, depending on how frequent v_E needs to be calibrated, breaking the power receiver operation can cause a significant opportunity loss, as the receiver cannot draw power during calibration. Second, the circuit that senses $v_{E(CL)}$ needs to handle the high common-mode voltage, as the v_C can be high during the normal operation. Finally, the coupled voltage v_E varies orders of magnitude, making the low-power ADC design challenging.

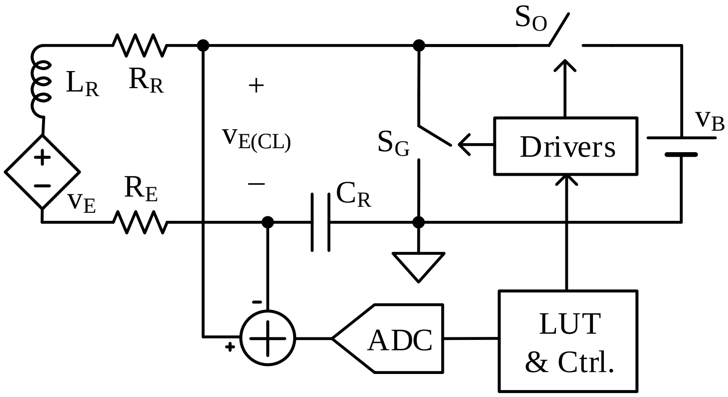

Figure 7-7. MPPT by calibrating coupled voltage and using a look-up table.

An alternative solution is to calibrate the saturated capacitor voltage v_C instead of v_E. This is possible because when loosely coupled, v_E is a $1/Q_R$ fraction of v_C. In other words,

$$v_{C(SAT)} = Q_R v_{E(PK)} . \tag{7.5}$$

Q_R stays constant in the low-coupling region, as the coupled resistance R_E is negligible. However, when the coupling is high, the high R_E lowers Q_R, the saturated $v_{C(PK)}$ is no longer proportional to $v_{E(PK)}$. So the MPPT scheme only works for the low-coupling region.

Finally, the MPPT can be achieved by monitoring the averaged $v_{C(PK)}$ of each cycle. According to the MPP theory developed in CHAPTER 5, the switched resonant half-bridge outputs the highest power when the averaged $v_{C(PK)}$ of each cycle is about $v_{C(OPT)}$, where

$$v_{C(OPT)} = 0.5 Q_R v_{E(PK)} = 0.5 v_{C(SAT)} . \tag{7.6}$$

Therefore, the MPPT can monitor and regulate the averaged $v_{C(PK)}$ of each cycle to half of the $v_{C(SAT)}$. To calibrate $v_{C(SAT)}$, the MPPT needs to halt the power transfer till the oscillation in the LC tank saturates. However, the energy accumulated in the LC tank can be transferred to the battery once the calibration finishes. So the MPPT induces less loss than the v_E- or v_C- calibration scheme.

7.4 Summary

Embedded microsensors collect, process, and transmit information that saves costs and lives. Inductively coupled power transfer can extend their lifetime by recharging their batteries wirelessly. To expand the functionality of the embedded microsensors, the transferred wireless power needs to be maximized. Plus, for real applications, the power receiver needs to tolerate wide coupling variations. Therefore, the objective of this research is to investigate and design a power receiver that outputs the highest power out of what's available for the widest coupling range possible. For this, a switched resonant half-bridge power receiver is proposed. The power stage can adjust both energy transfer duration and frequency for MPP without the help of an extra buffer stage. Plus, the operation is not breakdown-limited, so MPP can be achieved for a wide coupling range. An MPP theory is also developed to predict the optimal settings of the proposed power stage. At the theory's predicted settings, the power stage can output more than 98.6% of the MPP power. Finally, the research addresses the practical challenges in system integration, including over-voltage protection and synchronization. The fabricated self-synchronized power receiver prototype power and coupling range are 1.3× and 13× better than the SoA power receivers. The improvements potentially expand the functionality of embedded microsensors.

REFERENCES

[1] K. Stangel, S. Kolnsberg, D. Hammerschmidt, B. J. Hosticka, H. K. Trieu, and W. Mokwa, "A programmable intraocular CMOS pressure sensor system implant," *IEEE Journal of Solid-State Circuits,* vol. 36, no. 7, pp. 1094-1100, 2001.

[2] O. Paul and H. Baltes, "Novel fully CMOS-compatible vacuum sensor," *Sensors and Actuators A: Physical,* vol. 46, no. 1, pp. 143-146, 1995.

[3] L.-y. Sheng, Z. Tang, J. Wu, P. C. H. Chan, and J. K. O. Sin, "A low-power CMOS compatible integrated gas sensor using maskless tin oxide sputtering," *Sensors and Actuators B: Chemical,* vol. 49, no. 1, pp. 81-87, 1998.

[4] S. Gopi Nambiar and P. Ranjan, "Energy harvesting system for deployment of wireless sensor networks in nuclear fusion reactor," *IEEE International Conference on Green Technologies*, pp. 288-92, December, 2012.

[5] D. Mascarenas, E. Flynn, C. Farrar, G. Park, and M. Todd, "A mobile host approach for wireless powering and interrogation of structural health monitoring sensor networks," *IEEE Sensors Journal,* vol. 9, no. 12, pp. 1719-1726, 2009.

[6] D. Puccinelli and M. Haenggi, "Wireless sensor networks: applications and challenges of ubiquitous sensing," *IEEE Circuits and Systems Magazine,* vol. 5, no. 3, pp. 19-31, 2005.

[7] R.-F. Xue, H.-K. Cha, J. H. Cheong, K. P. Basappa, M. Je, and Y. Zheng, "Wireless powering and bidirectional telemetry front-end for implantable biomedical devices," *IEEE International Symposium on Integrated Circuits*, pp. 144-147, Dec. 2011.

[8] J. S. Ho, A. J. Yeh, E. Neofytou, K. Sanghoek, Y. Tanabe, B. Patlolla, R. E. Beygui, and A. S. Y. Poon, "Wireless power transfer to deep-tissue microimplants," *Proceedings of the National Academy of Sciences of the United States of America,* vol. 111, no. 22, pp. 7974-9, 2014.

[9] P. Cong, W. H. Ko, and D. J. Young, "Wireless batteryless implantable blood pressure monitoring microsystem for small laboratory animals," *IEEE Sensors Journal,* vol. 10, no. 2, pp. 243-254, 2010.

[10] M. M. Ahmadi and G. A. Jullien, "A wireless-implantable microsystem for continuous blood glucose monitoring," *IEEE Transactions on Biomedical Circuits and Systems,* vol. 3, no. 3, pp. 169-180, 2009.

[11] H. Kassiri, A. Bagheri, N. Soltani, K. Abdelhalim, H. M. Jafari, M. T. Salam, J. L. Perez Velazquez, and R. Genov, "Battery-less tri-band-radio neuro-monitor and responsive neurostimulator for diagnostics and treatment of neurological disorders," *IEEE Journal of Solid-State Circuits,* vol. 51, no. 5, pp. 1274-89, 2016.

[12] S. B. Lee, H.-M. Lee, M. Kiani, U.-M. Jow, and M. Ghovanloo, "An inductively powered scalable 32-channel wireless neural recording system-on-a-chip for neuroscience applications," pp. 360-371, 2010.

[13] J. Minkyu, C. Jia Hao, H. Chee Keong, *et al.*, "Wireless sensor microsystems for emerging biomedical applications (Invited)," *IEEE International Symposium on Radio-Frequency Integration Technology*, pp. 139-41, Aug. 2015.

[14] C. T. Wentz, J. G. Bernstein, P. Monahan, A. Guerra, A. Rodriguez, and E. S. Boyden, "A wirelessly powered and controlled device for optical neural control of freely-behaving animals," *Journal of Neural Engineering*, 2011.

[15] R. R. Harrison, P. T. Watkins, R. J. Kier, R. O. Lovejoy, D. J. Black, B. Greger, and F. Solzbacher, "A low-power integrated circuit for a wireless 100-electrode neural recording system," *IEEE Journal of Solid-State Circuits,* vol. 42, no. 1, pp. 123-33, 2007.

[16] D. Peng, J. Zhang, and L. Wang, "Experimental result on wireless power management microsystem for endoscopic capsule robot," *IEEE-EMBS International Conference on Biomedical and Health Informatics*, pp. 810-813, January 2012.

[17] B. Lenaerts and R. Puers, "An inductive power link for a wireless endoscope," *Biosensors and Bioelectronics,* vol. 22, no. 7, pp. 1390-1395, 2007.

[18] T. Sun, X. Xie, G. Li, Y. Gu, Y. Deng, and Z. Wang, "A two-hop wireless power transfer system with an efficiency-enhanced power receiver for motion-free capsule endoscopy inspection," *IEEE Transactions on Biomedical Engineering,* vol. 59, no. 12 PART2, pp. 3247-3254, 2012.

[19] J.-C. Chiou, S.-H. Hsu, Y.-T. Liao, Y.-C. Huang, G.-T. Yeh, C.-K. Kuei, and K.-S. Dai, "Toward a wirelessly powered on-lens intraocular pressure monitoring system," *IEEE Journal of Biomedical and Health Informatics,* vol. 20, no. 5, pp. 1216-1224, 2016.

[20] D. Laqua, T. Just, S. Hampl, V. Cimalla, O. Bludau, P. Husar, and M. Hoffmann, "Conception of an implantable RF-transmitter with self-sufficient power supply for intraocular pressure monitoring," *Biomedizinische Technik,* vol. 55, no. suppl1, pp. 137-40, 2010.

[21] C. Po-Jui, S. Saati, R. Varma, M. S. Humayun, and T. Yu-Chong, "Wireless intraocular pressure sensing using microfabricated minimally invasive flexible-coiled LC sensor implant," *Journal of Microelectromechanical Systems,* vol. 19, no. 4, pp. 721-34, 2010.

[22] H. Li, J. Tan, and M. Zhang, "Dynamics modeling and analysis of a swimming microrobot for controlled drug delivery," *IEEE Transactions on Automation Science and Engineering,* vol. 6, no. 2, pp. 220-227, 2009.

[23] Y. Yao-Joe, H. Yu-Jie, L. Hsin-Hung, W. Tao, H. Pen-Li, L. Chii-Wan, W. Yao-Hong, and L. Shey-shi, "A release-on-demand wireless CMOS drug delivery SoC based on electrothermal activation technique," *IEEE International Solid-State Circuits Conference*, pp. 288-289,289a, Feb. 2009.

[24] Y. Zhang, F. Zhang, Y. Shakhsheer, *et al.*, "A batteryless 19 w MICS/ISM-band energy harvesting body sensor node SoC for ExG applications," *IEEE Journal of Solid-State Circuits,* vol. 48, no. 1, pp. 199-213, 2013.

[25] S. Gambini, K. Skucha, P. P. Liu, J. Kim, and R. Krigel, "A 10 kPixel CMOS hall sensor array with baseline suppression and parallel readout for immunoassays," *IEEE Journal of Solid-State Circuits,* vol. 48, no. 1, pp. 302-317, 2013.

[26] R. F. Yazicioglu, P. Merken, R. Puers, and C. V. Hoof, "A 60 µW 60 nV/Hz readout front-end for portable biopotential acquisition systems," *IEEE Journal of Solid-State Circuits,* vol. 42, no. 5, pp. 1100-1110, 2007.

[27] M. J. Nothnagel, G. Park, and C. R. Farrar, "Wireless energy transmission for structural health monitoring embedded sensor nodes," *SPIE Health Monitoring of Structural and Biological Systems*, p. 653216, 2007.

[28] Y. Peng, L. Gang, and L. Yan, "Low-power design and critical event-triggered transmission scheme for wireless strain gauge sensor node in aircraft structural health monitoring," *Sensors and Transducers,* vol. 155, no. 8, pp. 10-20, 2013.

[29] C. Escriba, J. Fourniols, M. Lastapis, J. Boizard, G. Auriol, and S. Andrieu, "New real-time structural health monitoring microsystem for aircraft propeller blades," *IEEE Aerospace and Electronic Systems Magazine,* vol. 27, no. 2, pp. 29-41, 2012.

[30] G. vom Boegel, F. Meyer, and M. Kemmerling, "Batteryless sensors in building automation by use of wireless Energy Harvesting," *IEEE International Symposium on Wireless Systems*, pp. 72-7, Sept. 2012.

[31] M. Salas, O. Focke, A. S. Herrmann, and W. Lang, "Wireless power transmission for structural health monitoring of fiber-reinforced-composite materials," *IEEE Sensors Journal*, vol. 14, no. 7, pp. 2171-2176, 2014.

[32] S. Jiang and S. V. Georgakopoulos, "Optimum wireless power transmission through reinforced concrete structure," *IEEE International Conference on RFID*, pp. 50-56, April 2011.

[33] S. Jiang, S. V. Georgakopoulos, and O. Jonah, "Power transmission for sensors embedded in reinforced concrete structures," *Joint IEEE International Symposium on Antennas and Propagation and USNC-URSI National Radio Science Meeting*, pp. 1-2, July 2012.

[34] H. Marques, B. Borges, P. Ramos, and A. Martins, "Contactless battery charger for composite humidity and temperature wireless sensors," *IEEE International Conference on Computer as a Tool*, p. 4, April 2011.

[35] A. D. DeHennis and K. D. Wise, "A wireless microsystem for the remote sensing of pressure, temperature, and relative humidity," *Journal of Microelectromechanical Systems*, vol. 14, no. 1, pp. 12-22, 2005.

[36] D. Cirmirakis, A. Demosthenous, N. Saeidi, and N. Donaldson, "Humidity-to-Frequency Sensor in CMOS Technology With Wireless Readout," *IEEE Sensors Journal*, vol. 13, no. 3, pp. 900-8, 2013.

[37] E. G. Kilinc, F. Maloberti, and C. Dehollain, "Short-range remote powering for long-term implanted sensor systems in freely moving small animals," *IEEE Sensors Conference*, pp. 1-4, Nov. 2013.

[38] M. Flatscher, M. Dielacher, T. Herndl, T. Lentsch, R. Matischek, J. Prainsack, W. Pribyl, H. Theuss, and W. Weber, "A bulk acoustic wave (BAW) based transceiver for an in-tire-pressure monitoring sensor node," *IEEE Journal of Solid-State Circuits*, vol. 45, no. 1, pp. 167-177, 2010.

[39] M. Flatscher, M. Dielacher, T. Herndl, T. Lentsch, R. Matischek, J. Prainsack, W. Pribyl, H. Theuss, and W. Weber, "A robust wireless sensor node for in-tire-pressure monitoring," *IEEE International Solid-State Circuits Conference*, pp. 286-287,287a, Feb. 2009.

[40] R. R. Singh, L. Leng, A. Guenther, and R. Genov, "A CMOS-microfluidic chemiluminescence contact imaging microsystem," *IEEE Journal of Solid-State Circuits,* vol. 47, no. 11, pp. 2822-2833, 2012.

[41] N. Cottini, M. Gottardi, N. Massari, R. Passerone, and Z. Smilansky, "A 33 μW 64×64 pixel vision sensor embedding robust dynamic background subtraction for event detection and scene interpretation," *IEEE Journal of Solid-State Circuits,* vol. 48, no. 3, pp. 850-863, 2013.

[42] J. H. Cheong, C. K. Ho, S. S. Y. Ng, *et al.*, "A wirelessly powered and interrogated blood flow monitoring microsystem fully integrated with a prosthetic vascular graft for early failure detection," *IEEE Asian Solid-State Circuits Conference,* pp. 177-180, 2012.

[43] D. Cirmirakis, A. Demosthenous, N. Saeidi, and N. Donaldson, "Humidity-to-frequency sensor in CMOS technology with wireless readout," *IEEE Sensors Journal,* vol. 13, no. 3, pp. 900-908, 2013.

[44] M. Armand and J. M. Tarascon, "Building better batteries," *Nature,* vol. 451, no. 7179, pp. 652-657, 2008.

[45] S. Anuphappharadorn, S. Sukchai, C. Sirisamphanwong, and N. Ketjoy, "Comparison the Economic Analysis of the Battery between Lithium-ion and Lead-acid in PV Stand-alone Application," *Energy Procedia,* vol. 56, no. pp. 352-358, 2014.

[46] D. Aurbach, Y. Gofer, Z. Lu, *et al.*, "A short review on the comparison between Li battery systems and rechargeable magnesium battery technology," *Journal of Power Sources,* vol. 97-98, no. pp. 28-32, 2001.

[47] A. Alvarez-Carulla, J. Colomer-Farrarons, J. Lopez-Sanchez, and P. Miribel-Catala, "Piezoelectric harvester-based self-powered adaptive circuit with wireless data transmission capability for structural health monitoring," *IEEE Conference on Design of Circuits and Integrated Systems,* pp. 1-6, November 2015.

[48] H. J. Park, H. Sohn, C. B. Yun, J. Chung, and I. B. Kwon, "Development of a wireless power and data transmission system using laser and optoelectronic devices for guided wave-based structural health monitoring," *International Conference on Bridge Maintenance, Safety and Management,* pp. 269-276, July 2010.

[49] M. Ecker, N. Nieto, S. Käbitz, J. Schmalstieg, H. Blanke, A. Warnecke, and D. U. Sauer, "Calendar and cycle life study of Li(NiMnCo)O2-based 18650 lithium-ion batteries," *Journal of Power Sources,* vol. 248, no. pp. 839-851, 2014.

[50] J. Li, E. Murphy, J. Winnick, and P. A. Kohl, "Studies on the cycle life of commercial lithium ion batteries during rapid charge–discharge cycling," *Journal of Power Sources,* vol. 102, no. 1, pp. 294-301, 2001.

[51] U. Köhler, C. Antonius, and P. Bäuerlein, "Advances in alkaline batteries," *Journal of Power Sources,* vol. 127, no. 1, pp. 45-52, 2004.

[52] G. G. Yadav, X. Wei, J. Huang, J. W. Gallaway, D. E. Turney, M. Nyce, J. Secor, and S. Banerjee, "A conversion-based highly energy dense Cu2+ intercalated Bi-birnessite/Zn alkaline battery," *Journal of Materials Chemistry A,* vol. 5, no. 30, pp. 15845-15854, 2017.

[53] G. G. Yadav, J. W. Gallaway, D. E. Turney, M. Nyce, J. Huang, X. Wei, and S. Banerjee, "Regenerable Cu-intercalated MnO(2) layered cathode for highly cyclable energy dense batteries," *Nature communications,* vol. 8, no. pp. 14424-14424, 2017.

[54] R. A. Powers, "Batteries for low power electronics," *Proceedings of the IEEE,* vol. 83, no. 4, pp. 687-693, 1995.

[55] M. Uno and K. Tanaka, "Accelerated Charge–Discharge Cycling Test and Cycle Life Prediction Model for Supercapacitors in Alternative Battery Applications," *IEEE Transactions on Industrial Electronics,* vol. 59, no. 12, pp. 4704-4712, 2012.

[56] Z. S. Wu, K. Parvez, X. Feng, and K. Müllen, "Graphene-based in-plane micro-supercapacitors with high power and energy densities," *Nature Communications,* vol. 4, no. 1, p. 2487, 2013.

[57] G. V. Merrett and A. S. Weddell, "Supercapacitor leakage in energy-harvesting sensor nodes: Fact or fiction?," *2012 Ninth International Conference on Networked Sensing (INSS),* pp. 1-5, 11-14 June 2012 2012.

[58] J. G. Pepin, W. Borland, P. O'Callaghan, and R. J. S. Young, "Electrode-Based Causes of Delaminations in Multilayer Ceramic Capacitors," *Journal of the American Ceramic Society,* vol. 72, no. 12, pp. 2287-2291, 1989.

[59] E. O. Torres and G. A. Rincon-Mora, "An electrostatic CMOS/BiCMOS Li-ion vibration-based harvester-charger IC," *Ph.D. dissertation, School of Electrical and Computer Engineering, Georgia Institute of Technology, Atlanta, GA,* no. 2010.

[60] M. Zenker, A. Heinzel, G. Stollwerck, J. Ferber, and J. Luther, "Efficiency and power density potential of combustion-driven thermophotovoltaic systems using GaSb photovoltaic cells," *IEEE Transactions on Electron Devices,* vol. 48, no. 2, pp. 367-376, 2001.

[61] A. Nasiri, S. A. Zabalawi, and G. Mandic, "Indoor power harvesting using photovoltaic cells for low-power applications," *IEEE Transactions on Industrial Electronics,* vol. 56, no. 11, pp. 4502-4509, 2009.

[62] G.-T. Hwang, H. Park, J.-H. Lee, *et al.*, "Self-powered cardiac pacemaker enabled by flexible single crystalline PMN-PT piezoelectric energy harvester," *Advanced Materials,* vol. 26, no. 28, pp. 4880-4887, 2014.

[63] J. Briscoe and S. Dunn, "Piezoelectric nanogenerators – a review of nanostructured piezoelectric energy harvesters," *Nano Energy,* vol. 14, no. pp. 15-29, 2015.

[64] J. Sirohi and R. Mahadik, "Piezoelectric wind energy harvester for low-power sensors," *Journal of Intelligent Material Systems and Structures,* vol. 22, no. 18, pp. 2215-2228, 2011.

[65] C. L. Zhang, J. S. Yang, and W. Q. Chen, "Harvesting magnetic energy using extensional vibration of laminated magnetoelectric plates," *Applied Physics Letters,* vol. 95, no. 1, p. 013511, 2009.

[66] M. Jinyeong and S. B. Leeb, "Power electronic circuits for magnetic energy harvesters," *IEEE Transactions on Power Electronics,* vol. 31, no. 1, pp. 270-9, 2016.

[67] S. Yuan, Y. Huang, J. Zhou, Q. Xu, C. Song, and P. Thompson, "Magnetic field energy harvesting under overhead power lines," *IEEE Transactions on Power Electronics,* vol. 30, no. 11, pp. 6191-6202, 2015.

[68] E. O. Torres and G. A. Rincon-Mora, "Electrostatic energy-harvesting and battery-charging CMOS system prototype," *IEEE Transactions on Circuits and Systems I: Regular Papers,* vol. 56, no. 9, pp. 1938-1948, 2009.

[69] E. O. Torres and G. A. Rincon-Mora, "Energy-harvesting system-in-package microsystem," *Journal of Energy Engineering,* vol. 134, no. 4, pp. 121-9, 2008.

[70] M. Strasser, R. Aigner, C. Lauterbach, T. F. Sturm, M. Franosch, and G. Wachutka, "Micromachined CMOS thermoelectric generators as on-chip power supply," *Sensors and Actuators A: Physical,* vol. 114, no. 2, pp. 362-370, 2004.

[71] D. T. Crane and L. E. Bell, "Design to maximize performance of a thermoelectric power generator with a dynamic thermal power source," *Journal of Energy Resources Technology,* vol. 131, no. 1, 2009.

[72] V. Valente, C. Eder, N. Donaldson, and A. Demosthenous, "A high-power CMOS class-D amplifier for inductive-link medical transmitters," *IEEE Transactions on Power Electronics,* vol. 30, no. 8, pp. 4477-88, 2015.

[73] L. Xing, L. Yin-Ping, T. Chi-Ying, and K. Wing-Hung, "Wireless power transfer system with -modulated transmission power and fast load response for implantable medical devices," *IEEE Transactions on Circuits and Systems II: Express Briefs*, vol. 64, no. 3, pp. 279-83, 2017.

[74] S. Aldhaher, P. C. K. Luk, and J. F. Whidborne, "Electronic tuning of misaligned coils in wireless power transfer systems," *IEEE Transactions on Power Electronics,* vol. 29, no. 11, pp. 5975-82, 2014.

[75] S. Y. R. Hui, W. Zhong, and C. K. Lee, "A Critical Review of Recent Progress in Mid-Range Wireless Power Transfer," *IEEE Transactions on Power Electronics,* vol. 29, no. 9, pp. 4500-4511, 2014.

[76] T. Umeda, H. Yoshida, S. Sekine, Y. Fujita, T. Suzuki, and S. Otaka, "A 950-MHz rectifier circuit for sensor network tags with 10-m distance," *IEEE Journal of Solid-State Circuits,* vol. 41, no. 1, pp. 35-41, 2006.

[77] N. Xing and G. A. Rincon-Mora, "Generating the highest power with a tiny and distant inductively coupled coil," *2016 IEEE 25th International Symposium on Industrial Electronics,* pp. 477-80, June 2016.

[78] J. Dai and D. C. Ludois, "A survey of wireless power transfer and a critical comparison of inductive and capacitive coupling for small gap applications," *IEEE Transactions on Power Electronics,* vol. 30, no. 11, pp. 6017-6029, 2015.

[79] L. Chong-Yi, K. Chi-Jung, and M. Shau-Gang, "Wireless-power-transfer system using near-field capacitively coupled resonators," *IEEE Transactions on Circuits and Systems II: Express Briefs,* vol. 63, no. 9, pp. 898-902, 2016.

[80] N. Xing and G. A. Rincón-Mora, "180-nm 85%-efficient inductively coupled switched resonant half-bridge power receiver," *IEEE Transactions on Circuits and Systems II: Express Briefs,* vol. 66, no. 6, pp. 983-987, 2019.

[81] Q. W. Low and L. Siek, "A single-stage dual-output tri-mode AC-DC regulator for inductively powered application," *IEEE Transactions on Circuits and Systems I: Regular Papers,* vol. 66, no. 9, pp. 3620-3630, 2019.

[82] C. Lin, K. Wing-Hung, and T. Chi-Ying, "A 6.78-MHz single-stage wireless power receiver using a 3-mode reconfigurable resonant regulating rectifier," *IEEE Journal of Solid-State Circuits,* vol. 52, no. 5, pp. 1412-23, 2017.

[83] C. Lin, K. Wing-Hung, W. Tat-To, Y. Tak-Sang, and T. Chi-Ying, "21.7 A 6.78MHz 6W wireless power receiver with a 3-level 1 / / 0 reconfigurable resonant regulating rectifier," *2016 IEEE International Solid-State Circuits Conference (ISSCC), 31 Jan.-4 Feb. 2016*, pp. 376-7, 2016.

[84] L. Xing, T. Chi-Ying, and K. Wing-Hung, "A 13.56 MHz wireless power transfer system with reconfigurable resonant regulating rectifier and wireless power control for implantable medical devices," *IEEE Journal of Solid-State Circuits,* vol. 50, no. 4, pp. 978-89, 2015.

[85] "IEEE approved draft standard for safety levels with respect to human exposure to electric, magnetic and electromagnetic fields, 0 Hz to 300 GHz," *IEEE PC95.1/D3.5, October 2018,* no. pp. 1-312, 2019.

[86] A. K. Moghaddam, C. Joon Huang, H. Ramiah, J. Ahmadian, M. Pui-In, and R. P. Martins, "A 73.9%-efficiency CMOS rectifier using a lower DC Feeding (LDCF) self-body-biasing technique for far-field rf energy-harvesting systems," *IEEE Transactions on Circuits and Systems I: Regular Papers,* vol. 64, no. 4, pp. 992-1002, 2017.

[87] D. Mishra, S. De, and K. R. Chowdhury, "Charging time characterization for wireless RF energy transfer," *IEEE Transactions on Circuits and Systems II: Express Briefs,* vol. 62, no. 4, pp. 362-366, 2015.

[88] Z. Hameed and K. Moez, "A 3.2 V -15 dBm adaptive threshold-voltage compensated RF energy harvester in 130 nm CMOS," *IEEE Transactions on Circuits and Systems I: Regular Papers,* vol. 62, no. 4, pp. 948-56, 2015.

[89] J. Masuch, M. Delgado-Restituto, D. Milosevic, and P. Baltus, "Co-integration of an RF energy harvester into a 2.4 GHz transceiver," *IEEE Journal of Solid-State Circuits,* vol. 48, no. 7, pp. 1565-74, 2013.

[90] S. Keyrouz, H. J. Visser, and A. G. Tijhuis, "Ambient RF energy harvesting from DTV stations," *2012 Loughborough Antennas & Propagation Conference,* pp. 1-4, 2012.

[91] K. Jian, P. Y. Chiang, and A. Natarajan, "A 1.2cm2 2.4GHz self-oscillating rectifier-antenna achieving -34.5dBm sensitivity for wirelessly powered sensors," *2016 IEEE International Solid-State Circuits Conference (ISSCC), 31 Jan.-4 Feb. 2016*, pp. 374-5, 2016.

[92] L. Yan, D. Haojuan, H. Mo, L. Man-Kay, S. Sai-Weng, U. Seng-Pan, and R. P. Martins, "A wide input range dual-path CMOS rectifier for RF energy harvesting," *IEEE Transactions on Circuits and Systems II: Express Briefs,* vol. 64, no. 2, pp. 166-70, 2017.

[93] A. Mansano, S. Bagga, and W. Serdijn, "A high efficiency orthogonally switching passive charge pump rectifier for energy harvesters," *IEEE Transactions on Circuits and Systems I: Regular Papers,* vol. 60, no. 7, pp. 1959-66, 2013.

[94] L. G. de Carli, Y. Juppa, A. J. Cardoso, C. Galup-Montoro, and M. C. Schneider, "Maximizing the power conversion efficiency of ultra-low-voltage CMOS multi-stage rectifiers," *IEEE Transactions on Circuits and Systems I: Regular Papers,* vol. 62, no. 4, pp. 967-75, 2015.

[95] X. Nan and G. A. Rincon-Mora, "Highest wireless power: inductively coupled or RF," *Accepted for 2020 IEEE International Symposium on Quality Electronic Design*, 2017.

[96] Y. Lee, "RFID coil design," *Microchip Design Note,* no. AN678, 1998.

[97] J. D. Jackson, "Classical electrodynamics," ed: AAPT, 1999.

[98] C. S. Kong, "A general maximum power transfer theorem," *IEEE Transactions on Education,* vol. 38, no. 3, pp. 296-298, 1995.

[99] N. Xing and G. Rincon-Mora, "Highest maximum power point of radially distant inductively coupled power receivers with deep submicron CMOS," *IEEE Transactions on Industrial Informatics,* no. DOI: 10.1109/TII.2019.2910092.

[100] K. G. Moh, F. Neri, M. Sungwoo, Y. Pyeongwoo, Y. Jinhyuck, C. Youso, R. Yong-seong, K. Myeonglyong, and P. Byeong-Ha, "A fully integrated 6W wireless power receiver operating at 6.78MHz with magnetic resonance coupling," *2015 IEEE International Solid-State Circuits Conference (ISSCC), 22-26 Feb. 2015*, pp. 230-2, 2015.

[101] L. Qifan and Y. C. Liang, "An Inductive Power Transfer System With a High-Q Resonant Tank for Mobile Device Charging," *IEEE Transactions on Power Electronics,* vol. 30, no. 11, pp. 6203-12, 2015.

[102] J. T. Hwang, D. S. Lee, J. H. Lee, *et al.*, "An all-in-one (Qi, PMA and A4WP) 2.5W fully integrated wireless battery charger IC for wearable applications," *63rd IEEE International Solid-State Circuits Conference, ISSCC 2016, January 31, 2016 - February 4, 2016*, pp. 378-380, 2016.

[103] T. Jianlong and A. P. Hu, "A DC-voltage-controlled variable capacitor for stabilizing the ZVS frequency of a resonant converter for wireless power transfer," *IEEE Transactions on Power Electronics*, vol. 32, no. 3, pp. 2312-18, 2017.

[104] L. Shuenn-Yuh, C. Chih-Jen, and L. Ming-Chun, "A Low-Power Bidirectional Telemetry Device With a Near-Field Charging Feature for a Cardiac Microstimulator," *IEEE Transactions on Biomedical Circuits and Systems*, vol. 5, no. 4, pp. 357-67, 2011.

[105] J. Charthad, M. J. Weber, C. Ting Chia, and A. Arbabian, "A mm-sized implantable medical device (IMD) with ultrasonic power transfer and a hybrid bi-directional data link," *IEEE Journal of Solid-State Circuits*, vol. 50, no. 8, pp. 1741-53, 2015.

[106] L. Xing, T. Chi-Ying, and K. Wing-Hung, "Wireless power transfer system using primary equalizer for coupling- and load-range extension in bio-implant applications," *2015 IEEE International Solid-State Circuits Conference (ISSCC), 22-26 Feb. 2015*, pp. 228-9, 2015.

[107] C. Peters, J. Handwerker, D. Maurath, and Y. Manoli, "A sub-500 mV highly efficient active rectifier for energy harvesting applications," *IEEE Transactions on Circuits and Systems I: Regular Papers*, vol. 58, no. 7, pp. 1542-1550, 2011.

[108] L. Yan, H. Mo, C. Lin, K. Wing-Hung, U. Seng-Pan, and R. P. Martins, "A dual-output wireless power transfer system with active rectifier and three-level operation," *IEEE Transactions on Power Electronics*, vol. 32, no. 2, pp. 927-30, 2017.

[109] H. Cheng, T. Kawajiri, and H. Ishikuro, "A near-optimum 13.56 MHz CMOS active rectifier with circuit-delay real-time calibrations for high-current biomedical implants," *IEEE Journal of Solid-State Circuits*, vol. 51, no. 8, pp. 1797-809, 2016.

[110] H. Yuh-Shyan, L. Chia-Cheng, Y. Yao-Wei, C. Jiann-Jong, and Y. Cheng-Chieh, "A 13.56-MHz low-voltage and low-control-loss RF-DC rectifier utilizing a reducing reverse loss technique," *IEEE Transactions on Power Electronics*, vol. 29, no. 12, pp. 6544-54, 2014.

[111] J. Yoo, Y. Long, L. Seulki, K. Yongsang, and Y. Hoi-Jun, "A 5.2 mW self-configured wearable body sensor network controller and a 12 W wirelessly powered sensor for a continuous health monitoring system," *IEEE Journal of Solid-State Circuits*, vol. 45, no. 1, pp. 178-88, 2010.

[112] T. Kaya and H. Koser, "A new batteryless active RFID system: Smart RFID," *2007 1st Annual RFID Eurasia, September 5, 2007 - September 6, 2007,* 2007.

[113] G. Chen, S. Hanson, D. Blaauw, and D. Sylvester, "Circuit design advances for wireless sensing applications," *Proceedings of the IEEE,* vol. 98, no. 11, pp. 1808-27, 2010.

[114] H. Xu and M. Ortmanns, "A Temperature and Process Compensated Ultralow-Voltage Rectifier in Standard Threshold CMOS for Energy-Harvesting Applications," *IEEE Transactions on Circuits and Systems II: Express Briefs,* vol. 58, no. 12, pp. 812-816, 2011.

[115] O. Lazaro and G. A. Rincon-Mora, "Inductively coupled 180-nm CMOS charger with adjustable energy-investment capability," *IEEE Transactions on Circuits and Systems II: Express Briefs,* vol. 60, no. 8, pp. 482-6, 2013.

[116] O. Lazaro and G. A. Rincon-Mora, "A nonresonant self-synchronizing inductively coupled 0.18-m CMOS power receiver and charger," *IEEE Journal of Emerging and Selected Topics in Power Electronics,* vol. 3, no. 1, pp. 261-271, 2015.

[117] A. Berger, M. Agostinelli, S. Vesti, J. A. Oliver, J. A. Cobos, and M. Huemer, "A wireless charging system applying phase-shift and amplitude control to maximize efficiency and extractable power," *IEEE Transactions on Power Electronics,* vol. 30, no. 11, pp. 6338-48, 2015.

[118] K. Colak, E. Asa, M. Bojarski, D. Czarkowski, and O. C. Onar, "A novel phase-shift control of semibridgeless active rectifier for wireless power transfer," *IEEE Transactions on Power Electronics,* vol. 30, no. 11, pp. 6288-97, 2015.

[119] L. Jun-Young and H. Byung-Moon, "A bidirectional wireless power transfer EV charger using self-resonant PWM," *IEEE Transactions on Power Electronics,* vol. 30, no. 4, pp. 1784-7, 2015.

[120] T. Diekhans and R. W. D. Doncker, "A dual-side controlled inductive power transfer system optimized for large coupling factor variations and partial load," *IEEE Transactions on Power Electronics,* vol. 30, no. 11, pp. 6320-6328, 2015.

[121] B. X. Nguyen, D. M. Vilathgamuwa, G. H. B. Foo, W. Peng, A. Ong, U. K. Madawala, and N. Trong Duy, "An efficiency optimization scheme for bidirectional inductive power transfer systems," *IEEE Transactions on Power Electronics,* vol. 30, no. 11, pp. 6310-19, 2015.

[122] M. Kiani, L. Byunghun, Y. Pyungwoo, and M. Ghovanloo, "A power-management ASIC with Q-modulation capability for efficient inductive power transmission," *2015 IEEE International Solid-State Circuits Conference (ISSCC), 22-26 Feb. 2015*, pp. 226-8, 2015.

[123] H. S. Gougheri and M. Kiani, "Current-Based Resonant Power Delivery With Multi-Cycle Switching for Extended-Range Inductive Power Transmission," *IEEE Transactions on Circuits and Systems I: Regular Papers,* vol. 63, no. 9, pp. 1543-52, 2016.

[124] M. Kiani, B. Lee, P. Yeon, and M. Ghovanloo, "A Q-Modulation technique for efficient inductive power transmission," *IEEE Journal of Solid-State Circuits,* vol. 50, no. 12, pp. 2839-2848, 2015.

[125] C. Myungjoon, J. Taekwang, J. Junwon, J. Seokhyeon, D. Blaauw, and D. Sylvester, "A current-mode wireless power receiver with optimal resonant cycle tracking for implantable systems," *2016 IEEE International Solid-State Circuits Conference (ISSCC), 31 Jan.-4 Feb. 2016*, pp. 372-3, 2016.

[126] G. Villar, E. Alarcon, J. Madrenas, F. Guinjoan, and A. Poveda, "Energy optimization of tapered buffers for CMOS on-chip switching power converters," *2005 IEEE International Symposium on Circuits and Systems,* pp. 4453-4456 Vol. 5, 23-26 May 2005 2005.

[127] M. C. Shults, R. K. Rhodes, S. J. Updike, B. J. Gilligan, and W. N. Reining, "A telemetry-instrumentation system for monitoring multiple subcutaneously implanted glucose sensors," *IEEE Transactions on Biomedical Engineering,* vol. 41, no. 10, pp. 937-42, 1994.

[128] O. Lazaro and G. A. Rincon-Mora, "180-nm CMOS wideband capacitor-free inductively coupled power receiver and charger," *IEEE Journal of Solid-State Circuits,* vol. 48, no. 11, pp. 2839-49, 2013.

[129] X. Wei, Z. Wang, and H. Dai, "A critical review of wireless power transfer via strongly coupled magnetic resonances," *Energies,* vol. 7, no. 7, 2014.

[130] N. Xing and G. A. Rincón-Mora, "180-nm 85%-efficient inductively coupled switched resonant half-bridge power receiver," *IEEE Transactions on Circuits and Systems II: Express Briefs,* no. 10.1109/TCSII.2018.2867795.

[131] X. Nan and G. A. Rincon-Mora, "Power analysis and maximum output-power scheme for inductively coupled resonant power receivers," *2017 IEEE 60th International Midwest Symposium on Circuits and Systems (MWSCAS), 6-9 Aug. 2017*, pp. 293-6, 2017.

[132] C. Peng, W. H. Ko, and D. J. Young, "Wireless batteryless implantable blood pressure monitoring microsystem for small laboratory animals," *IEEE Sensors Journal,* vol. 10, no. 2, pp. 243-54, 2010.

[133] W. Hayward, *Introduction to radio frequency design*: American Radio Relay League, 1994.

[134] M. H. Perrott, T. L. Tewksbury, and C. G. Sodini, "A 27 mW CMOS fractional-N synthesizer/modulator IC," *IEEE International Solids-State Circuits Conference*, pp. 366-367, Feb. 1997.

[135] T. Jang, N. Xing, F. Liu, J. Shin, H. Ryu, J. Kim, T. Kim, J. Park, and H. Park, "A 0.026mm^2 5.3mW 32-to-2000MHz digital fractional-N phase locked-loop using a phase-interpolating phase-to-digital converter," *IEEE International Solid-State Circuits Conference*, pp. 254-255, Feb. 2013.

[136] C. Myungjoon, J. Taekwang, J. Junwon, J. Seokhyeon, D. Blaauw, and D. Sylvester, "A resonant current-mode wireless power receiver and battery charger with -32 dBm sensitivity for implantable systems," *IEEE Journal of Solid-State Circuits,* vol. 51, no. 12, pp. 2880-92, 2016.

[137] U. K. Madawala, M. Neath, and D. J. Thrimawithana, "A power–frequency controller for bidirectional inductive power transfer systems," *IEEE Transactions on Industrial Electronics,* vol. 60, no. 1, pp. 310-317, 2013.

[138] K. Wei, Z. Zhang, W. Chen, Z. Feng, and M. F. Iskander, "A triband shunt-fed omnidirectional planar dipole array," *IEEE Antennas and Wireless Propagation Letters,* vol. 9, no. pp. 850-853, 2010.

[139] M. J. Wilson and S. R. Ford, *The ARRL Handbook for Radio Communications 2007*: American Radio Relay League, 2006.

[140] T. Yestrebsky, "MICRF001 Antenna Design Tutorial," *Application Note,* vol. 23, no. p. 8, 1999.

[141] A. Yaghjian, "An overview of near-field antenna measurements," *IEEE Transactions on Antennas and Propagation,* vol. 34, no. 1, pp. 30-45, 1986.

[142] A. A. Blanco and G. A. Rincón-Mora, "A 44–93-µs 250–400-mV 0.18-µm CMOS starter for DC-sourced switched-inductor energy harvesters," *IEEE Transactions on Circuits and Systems II: Express Briefs,* vol. 61, no. 12, pp. 1002-1006, 2014.

[143] A. A. Blanco and G. A. Rincón-Mora, "Bootstrapping and resetting CMOS starter for thermoelectric and photovoltaic chargers," *IEEE Transactions on Circuits and Systems II: Express Briefs*, vol. 65, no. 2, pp. 156-160, 2018.

[144] A. A. Abdelmoaty, M. Al-Shyoukh, H. Ying-Chih, and A. A. Fayed, "A MPPT circuit with 25 W power consumption and 99.7% tracking efficiency for PV systems," *IEEE Transactions on Circuits and Systems I: Regular Papers*, vol. 64, no. 2, pp. 272-82, 2017.

[145] L. Hongchang, L. Jie, W. Kangping, C. Wenjie, and Y. Xu, "A maximum efficiency point tracking control scheme for wireless power transfer systems using magnetic resonant coupling," *IEEE Transactions on Power Electronics*, vol. 30, no. 7, pp. 3998-4008, 2015.

[146] Y. Tae-Dong, K. DukSoo, K. Seung-Tae, and Y. Jong-Won, "Design of maximum efficiency tracking control scheme for closed-loop wireless power charging system employing series resonant tank," *IEEE Transactions on Power Electronics,* vol. 32, no. 1, pp. 471-8, 2017.

[147] W. X. Zhong and S. Y. R. Hui, "Maximum energy efficiency tracking for wireless power transfer systems," *IEEE Transactions on Power Electronics,* vol. 30, no. 7, pp. 4025-4034, 2015.